Electrochemical Sensing of Environmental and Biological Samples

by

Anna Nelson

A dissertation submitted in partial fulfillment
of the requirements for the degree of
Doctor of Philosophy
(Chemical Engineering)
in the University of Michigan
2023

Doctoral Committee:

Professor Mark A. Burns, Chair
Professor James A. Ashton Miller
Assistant Professor Jouha Min
Assistant Professor Nirala Singh

Anna M. Nelson

nelsonan@umich.edu

ORCID iD: 0000-0002-9301-6161

© Anna M. Nelson 2023

Dedication

To my mom, dad, Keegan, and Sawyer.

Acknowledgements

This dissertation would not have come to fruition without the network of people who supported me throughout. You all have a piece in this, thank you.

First and foremost, to Sanaz: I cannot put into words how grateful I am for your friendship and collaboration during our time at Michigan Tech and the University of Michigan. Before you came here, I was wandering aimlessly and your kindness, many zoom calls (with lovely Liam cameos), and research guidance helped me learn how to become a productive researcher.

To my parents: I would never have applied for a PhD without your direction, and I am certain I would never have completed this degree without you. You both have been my number one supporters, with constant encouragement, advice and love. I am so grateful for you.

To my partner in life and all things, Keegan: You were my rock through these tough years of graduate school. Thank you for your support, logical reasoning skills, love and for the many delicious meals you cooked (… or bought) for me.

To Katie and Chris: Thank you for being my home away from home.

To Chloe: Your friendship has been critical to maintaining my sanity, and I enjoyed experiencing all the stages of graduate school with you.

And other friends from all walks of life: I appreciated the much-needed break from graduate school and enjoyed spending time with you all.

To my labmates before me: It was hard watching you all leave, but I learned so much from each one of you. Alyse, you taught me how to be organized. Zach, you were the first person

to encourage me to join the Burns Lab. Martin, I admire your confidence and independence and appreciate all the advice you gave me to increase these qualities in my research. Brian, thank you for all your help through the years. Sarah, I appreciate your positive outlook that always brightened the lab. Jaesung, thank you for teaching me fabrication. And to my current labmate, Scott: Thanks for all the fabrication you did for me. I enjoyed our time GSIing fluids and discussing cool fabrication methods together.

To my committee: Prof. Ashton-Miller, thank you for your kind words of encouragement and freedom you gave me to explore with the chloride sensor project. Prof. Jouha Min, thank you for all your time training me on the electrochemical assay and your advice on crafting experiments with the goal being to learn. I really enjoyed working in your lab space during the final months of my degree. Prof. Nirala Singh, thank you for teaching me the fundamentals of electrochemistry! Your class was so beneficial to my understanding and fueled my passion.

And last, but not least, to my advisor, Mark: When I came to you and told you it was my dream to do electrochemistry, you said your passion was optical detection, but you would help me achieve my dream. Now, here I am. With your mentorship, I have grown so much as a scientist and person. Thank you, for pushing me to become more independent, teaching me how to think in a different way, and believing in me.

Table of Contents

Dedication ii

Acknowledgements iii

List of Tables viii

List of Figures ix

Abstract xvii

Chapter 1 Introduction 1

1.1 Motivation 1

1.2 Prevalent Detection Methods for Ion and Biomarker Monitoring 3

1.2.1 Optical Detection 4

1.2.2 Electrochemical Detection 5

1.3 Organization of this Dissertation 7

Chapter 2 Electrochemical Deposition of Lead for Water Quality Sensing 10

2.1 Introduction 10

2.2 Materials and Methods 12

2.2.1 Sensor Design and Fabrication 12

2.2.2 Chemicals and Test Solution Preparation 13

2.2.3 Experimental Setup 13

2.2.4 Scanning Electron Microscopy 14

2.2.5 Fractal Dimension 14

2.2.6 Lead Ion Transport Simulation 15

2.3 Results and Discussion 16

2.3.1 Lead Sensor Detection Mechanism 16
2.3.2 COMSOL Multiphysics® Simulation of Lead Ion Diffusion 21
2.3.3 Shortening and Improving the Stability of the Detection Signal 23
2.4 Conclusion 26
Chapter 3 Electrochemical Sensing of Urinary Chloride Ion Concentration for Near Real-Time Monitoring 28
3.1 Introduction 28
3.2 Theory 31
3.3 Materials and Methods 33
3.3.1 Chemicals and Test Solution Preparation 33
3.3.2 Sensors and Experimental Setup 34
3.3.3 Measurement and Data Analysis 35
3.3.4 Electrode Surface Characterization 36
3.4 Results and Discussion 36
3.4.1 Detection of Chloride Ion Concentration Using Chronopotentiometry 36
3.4.2 Current Density Optimization for Detection of Biologically Relevant Chloride Concentration 38
3.4.3 Detection of Chloride Ion Concentration Using Swept Current Densities 43
3.4.4 Sensor Reusability 47
3.4.5 Effect of Relevant Clinical Parameters on Transition Time 50
3.5 Conclusion 53
Chapter 4 Electrochemical Sensing of Traumatic Brain Injury Biomarkers 55
4.1 Introduction 55
4.2 Background 57
4.3 Materials and Methods 60
4.3.1 Antibody Conjugation to Magnetic Beads 60

4.3.2 Bicinchoninic acid Assay 61
4.3.3 GFAP and UCH-L1 Sandwich Immunoassay 61
4.3.4 Electrochemical Assay, Testing and Analysis 63
4.4 Results and Discussion 64
4.4.1 The Effect of Reagent Concentration on Assay Signal 64
4.4.2 The Effect of Time on Assay Performance 66
4.4.3 Electrochemical Detection of TBI Biomarkers 69
4.4.4 Device Design and Multiplexing 72
4.5 Conclusion 74
Chapter 5 Conclusion and Future Work 76
5.1 Summary 76
5.2 Future Work 77
5.2.1 Lead Sensor 77
5.2.2 Urinary Chloride Sensor 79
5.2.3 Traumatic Brain Injury Biomarker Sensor 81
5.3 Conclusion 82
Bibliography 86

List of Tables

Table 1.1:Guide to each electrochemical sensing strategy employed in this dissertation. 8

Table 2.1:Device geometries respective geometrical parameters and response time in lead measurement mode (ΔV_1). *Two of the devices did not respond after running the deposition for 233 hrs..... 24

Table 3.1:Comparison of the square root of transition time of tests conducted with an individual electrode versus tests completed with the sweep method in various NaCl concentrations (N=3) in 20 mM Na_2SO_4 at 25°C. 45

Table 3.2:Comparison of the average measured chloride concentration, through back calculation in Sand equation, of tests conducted with an individual electrode versus tests completed with the sweep method in various NaCl concentrations (N=3) in 20 mM Na_2SO_4 at 25°C..... 45

List of Figures

Figure 2.1:(a) The schematic diagram of the four-electrode system. (b) Sensor schematic with three different sensing configurations including: deposition mode (ΔV) between anode and cathode, lead measurement mode (ΔV_1) between anode and F2, and heavy metal measurement mode (ΔV_2) between F3 and cathode 13

Figure 2.2:(a) Potential (ΔV) signal versus time at three different operational mode: deposition mode, lead measurement mode, and heavy metal measurement mode. (b) The SEM images were taken and studied for six different sensors stopped after 6, 12, 18, 24, 48, and 72 hrs. SEM images show lead oxide growth over time at the tip side of the first anode digit. Sensors were rinsed with deionized water prior to imaging. (c) Deposited lead oxide length over time with a growth rate between 0.05 and 0.15 μm/hr. All devices had a 5 μm gap between anode and F2. Tests were conducted with lead solutions of 15 ppb $PbCl_2$, 0.01 M NaCl, and deionized water. 18

Figure 2.3:Potential (ΔV) signal versus time at three different operational mode: deposition mode, lead measurement mode, and heavy metal measurement mode in control solution of 0.01 M NaCl using the 5 μm device geometry. 19

Figure 2.4:(a) EDS Spectra composition of a broken lead fragment on Pt electrode. Large peak at ~ 2 keV is from Pt. (b) SEM Image of analyzed area in 5 μm gap distance device. 20

Figure 2.5:(a) EDS Spectra Composition of lead presence in 5 μm gap between anode and F2. The smooth particle covering the gap is believed to be NaCl. (b) SEM Image of analyzed area. 20

Figure 2.6:A plot of log N versus log ε using the box-counting method gives a fractal dimension f_D = - slope. The f_D of six different lead sensors were found to be 1.71, 1.74, 1.65, 1.71, 1.71, and 1.68 after 6, 12, 18, 24, 48, and 72 hrs, respectively. Devices had a gap distance of 5 µm. Lead sensors were tested in 15 ppb lead solutions 21

Figure 2.7:(a) Schematic of lead sensor geometry with deposition areas of interest. The ion concentration gradient is shown in the area closer to the anode tip generated with COMSOL®. (b) COMSOL® simulation of spatial dependence of Pb^{2+} ion flux versus location along the 1st anode digit was plotted at 0.2 µm above the surface in the z direction. The SEM images of (c) anode corner, (d) anode palm, and (e) anode tip after 12 hrs of lead deposition in 15 ppb lead solution. Sensor was gently washed with deionized water prior to imaging and had a 5 µm gap distance. 23

Figure 2.8:(a) A representative potential signal curve for each gap distance in lead measurement mode. All experiments were conducted with 15 ppb lead solution. (b) The average detection time versus gap distance ($n \geq 3$ sensors) between anode and F2 with a growth rate ranging between 0.05 and 0.15 µm/hr. 24

Figure 2.9:Potential signal during lead measurement mode (ΔV_1) for (a) stagnant solutions and (c) 360 rpm agitated solutions. Each curve represents a unique device in isolated experiment. SEM images of sensor in (b) stagnant and (d) 150 rpm agitated solutions. Each curve represents a unique device in isolated experiment. SEM images of sensor in (b) stagnant and (d) 150 rpm agitated solutions. Each SEM image was taken in different devices with 5 µm gap distance that both ran for ~27 hours in 15 ppb lead solution. 26

Figure 3.1:(a) Schematic of chronopotentiometric method. The local depletion creates a chloride ion con-centration gradient, shown by the blue curve, between the working and reference electrodes. (b) Schematic of DropSens C013 screen-printed electrodes and chip holder. The working electrode (W) and reference electrode (R) are silver, while the counter electrode (C) is made of carbon. 32

Figure 3.2:(a) Representative chronopotentiograms at 50 mM NaCl and 20 mM Na_2SO_4 at 25 °C in 240 A/m^2. (b) The effect of concentration on the potential response and transition time at 25 °C in 240 A/m^2. The dotted line represents the derivative of the chronopotentiogram. 37

Figure 3.3:Scanning electron microscopy images of 50 mM NaCl and 20 mM Na_2SO_4 at 25 °C at (a) 60 A/m^2 after running for 3 s and (b) after 15 s; at 240 A/m^2 for (d) 0.5 s prior to transition time and (e) 3 s after transition time; at 960 A/m^2 with a (g) voltage cutoff of 0.9 V and (h) without a voltage cutoff running for 3 s. Each experiment was used with a fresh screen-printed electrode. The corresponding chronopotentiogram for the 60 A/m^2, 240 A/m^2, and 960 A/m^2 experiments are found in (c), (f), and (i), respectively. The potential cutoff is represented by a horizontal red line. The transition time is represented by a vertical cyan line. All scale bars are 2.5 μm 39

Figure 3.4:SEM/EDS of (a) the working electrode (b) the blue barrier film located around the electrodes (c) the reference electrode and (d) the counter electrode of a bare Dropsens C013 electrode. All scale bars are 25 μm. 40

Figure 3.5:Corresponding EDS to SEM images shown in Figure 3.3 of 50 mM NaCl and 20 mM Na_2SO_4 at 25 °C at (a) 60 A/m^2 after running for 1s and (b) after 15s. At 240 A/m^2 for (c) 0.5s

and (d) 3s. At 960 A/m^2 with a (e) voltage cutoff of 0.9V and (f) without a voltage cutoff running for 3 s. All scale bars 2.5 μm. 41

Figure 3.6:SEM image of the reference electrode after a solution of 50 mM NaCl and 20 mM Na_2SO_4 was tested at 25 °C with 960 A/m^2. 42

Figure 3.7:The experimental and theoretical (black line) square root of transition time (N = 3) as a function of chloride concentration in 20 mM Na_2SO_4 at 25 °C. One current density does not resolve the entire relevant concentration range of 5–250 mM NaCl. 43

Figure 3.8:Chronopotentiogram of each mode of sweep test run in succession at 3 s for 960 A/m^2,480 A/m^2, and 60 A/m^2 in 20 mM Na_2SO_4 at 25 °C in NaCl concentrations of (a) 0 mM, (b) 5 mM, (c) 10 mM, (d) 25 mM, (e) 50 mM, (f) 75 mM, (g) 100 mM, (h) 150 mM, and (i) 200 mM. Vertical dotted lines in each plot indicate the transition time. Prior to each constant current density step, the system was run at OCP for 1 min. 44

Figure 3.9:Average time to potential cutoff when run for 3 s at 960 A/m^2 in 20 mM Na_2SO_4 at 25 °C. Note that 150 and 200 mM NaCl never reached the cutoff. The sweep methodology only required 1 step to resolve 25 to 200 mM NaCl. Note that the time to potential cutoff was used as the signal for 25–75 mM, and the transition time was used to resolve 75–200 mM. For 5 to 15 mM, only two sweep steps were needed. 46

Figure 3.10:The potential value at 0.2 s during the sweep experiments for each current density step. 47

Figure 3.11:The measured chloride concentration, from back calculation using transition time, versus cycle number, using fresh 5 mL solutions with a reused sensor with 5 mM NaCl at 60

A/m^2, 50 mM NaCl at 240 A/m^2, and 100 mM at 960 A/m^2, in solutions of 20 mM Na_2SO_4 at room temperature, run for 3 s, or until the 0.9 V cutoff was reached. 48

Figure 3.12:SEM images of sensors after running for (a) and (d) 1 cycle; (b) and (e) 2 cycles; and (c) and (f) 3 cycles, with experimental conditions of 50 mM NaCl, 240 A/m^2 and 100 mM NaCl, 960 A/m^2, respectively. Each cycle used 5 mL of fresh 20 mM Na_2SO_4 simple solution at 25 °C. A new electrode was used for each test, and was stopped after different cycle numbers. All scale bars are 2.5 µm. 49

Figure 3.13:EDS corresponding to Figure 3.12 of sensors in 50 mM NaCl and 240 A/m^2 after running for (a) and (d) 1 cycle, (b) and (e) 2 cycles and (c) and (f) 3 cycles in 50 mM NaCl, 240 A/m^2 and 100 mM NaCl, 960 A/m^2 respectively. Each cycle used 5 mL of fresh 20 mM Na_2SO_4 simple solution at 25°C. A new electrode was used for each test and was stopped after different cycle numbers. All scale bars are 2.5 µm. 50

Figure 3.14:The effect of (a) pH at 20 mM Na_2SO_4 and 100 mM NaCl at 25°C; (b) temperature in 20 mM Na_2SO_4 and 100 mM NaCl; and (c) conductivity with varying Na_2SO_4 concentrations and 100 mM NaCl at 25 °C with respect to average squared root of transition time (N=3) in 480 A/m^2. The effect of other ions was investigated with (d) NaCl-spiked artificial urine as a function of the average square root of transition time (N=3) at 480 A/m^2 and 25 °C. Each curve was fit with a regression line (blue dotted line). 52

Figure 3.15:Chronopotentiogram of 100 mM NaCl, 20 mM Na_2SO_4 was tested at 25 °C with 480 A/m^2 with and without 150 µg/L NaI. The sodium iodide did not affect the signal. The dashed line represents the transition time for each curve. 53

Figure 4.1:Schematic of an enzyme linked sandwich immunoassay. The enzyme immunoassay is capable of being both an optical and electrochemical detection method. Note, the depicted immunoassay is not to scale..... 58

Figure 4.2:Schematic of the TMB reaction in the presence of HRP enzyme and hydrogen peroxide..... 60

Figure 4.3:Schematic of the assay steps necessary to detect the biomarker of interest (GFAP depicted) with optical and electrochemical detection. Each step was completed in a microcentrifuge tube with 2.8 μm diameter beads. Note, a single bead is depicted as a representative for millions of beads that were present during the assay..... 63

Figure 4.4:Absorbance measurements (λ = 450 nm) for varying capture antibody concentrations (N=3) with Incubation I – IV times of 2 hour, 2 hour, 20 minute and 6 minutes, respectively. .. 65

Figure 4.5:Absorbance measurements (λ = 450 nm) for varying GFAP detection antibody concentrations with fixed GFAP protein concentration and control (N=4) after (a) 3 minute and (b) 20 minute Incubation IV times with (c) the corresponding signal to noise ratio. Incubation I – III times were 2 hour, 2 hour, and 20 minute, respectively. 66

Figure 4.6:Standard calibration curve of GFAP (N=3) with absorbance measurements (λ = 450 nm) with varying Incubation I-IV times. 67

Figure 4.7:Standard calibration curve with absorbance measurements (λ = 450 nm) for varying Incubation IV times (3 minute; N=1; 6 and 20 minute N=2). Incubations I, II and III were 30 minutes, 20 minutes and 15 minutes, respectively. 68

Figure 4.8:Standard calibration curve with absorbance measurements (λ = 450 nm) for varying Incubation I times (N=3; N=6 for 0). Incubations II, III and IV were 2 hours, 20 minutes and 6 minutes, respectively..... 69

Figure 4.9:(a) The electrodes consist of gold working (WE), counter (CE), and silver reference (RE) used to electrochemically detect biomarker concentration. The HRP enzyme in the presence of H_2O_2 converts the TMB substrate into TMB^+ which is reduced back into TMB with the electrodes. (b) The generated representative reductive current between the working and counter electrodes serves as an indicator of amount of TMB^+ converted and corresponds to the GFAP concentration. The amperometry measurement was conducted with 5 µm beads reacted with 20 µL TMB for 6 minutes at varying GFAP concentrations. 70

Figure 4.10:(a) Representative amperometry measurement of 5000 pg/mL GFAP concentration. (b) The reductive current was averaged at different time intervals along the amperometry curves for different GFAP concentrations (N=3; N=5 for 0 pg/mL). Incubation times (I-IV) were 2 hours, 2 hours, 20 minutes, and 6 minutes, respectively. 71

Figure 4.11:Comparison of optical and electrochemical detection methods standard curves with (a) GFAP optical absorbance (N=4; N=8 for 0 pg/mL) (b) GFAP amperometry measurement (N=3; N=5 for 0 pg/mL) (c) UCH-L1 optical absorbance (N=2; N=4 for 0 pg/mL) (d) UCH-L1 amperometry measurement (N=2; N=4 for 0 pg/mL). Incubation times (I-IV) were 2 hours, 2 hours, 20 minutes, and 6 minutes, respectively. For optical measurements, 2.5 µm beads were reacted with 100 µL of TMB and 50 µL of acid stop solution. The beads were removed from solution and measured in a plate reader at λ=450 nm. For electrochemical measurements, 5 µm

beads reacted with 20 µL TMB and the first 15s of measurement was averaged. Each curve was fit with a linear regression trendline (blue dotted line). 72

Figure 4.12:(a) The proposed multiplexed device design with three sets of electrodes placed at different heights along the channel. (b) One dimensional diffusion calculation to determine the ratio of final and initial TMB^+ concentration as a function of the distance from a TMB^+ source (e.g., working electrode). The TMB^+ diffusion coefficient was $3x10^{-10}$ m^2/s [37]. If electrode sets are placed 3 mm apart, TMB^+ should not diffuse between different electrode sets after 60 minutes. 74

Abstract

Recent advancements in the sensor manufacturing industry have facilitated the development of rapid, inexpensive, and user-friendly sensors for end-point monitoring of different environmental (e.g., water) and biological (e.g., urine, blood) samples. However, developing portable, simple and long-term sensors with minimal maintenance still remains a challenge as sensors are often reliant on the user with bulky instrumentation and thus, quantification of analytes of interest are primarily conducted by sending samples to a local or central laboratory. Recently, electrochemical sensors have shown promise to develop end-point monitoring systems as they are rapid, easily miniaturized, and inexpensive. In this doctoral research, we focus on development of electrochemical sensors for near real-time monitoring of lead ions in water, quantification of chloride ions in urine samples, and assessment of traumatic brain injury (TBI) biomarkers in blood samples. Lead contamination of drinking water from lead infrastructure used in buildings prior to 1986 is difficult to predict and hazardous to human health. Changes in water chemistry and aging infrastructure can result in large scale public health crisis, as evidenced by the 2014 Flint Water Crisis. Presently, heavy metal water testing is reliant on the user to send water samples into a lab with multi-week wait times. We have developed an end-point sensor capable of monitoring drinking water for 15 ppb lead. The sensor captures electrodeposited lead oxide and triggers when the electrodeposit bridges two electrodes in the four-electrode sensor through a diffusion limited process. We were able to re-design the sensor to reduce the detection time by 40%. Ion monitoring in urine also relies on laboratory testing with long turnaround times. Urinary chloride, one of the most prevalent electrolytes in the body,

has been an underutilized indicator of hydration, kidney and heart health. By providing near real-time quantification of urinary chloride concentration, laborious 24-hour fluid collection can be mitigated. To this end, we developed a chronopotentiometry sensor capable of rapid chloride quantification in 3 seconds. With a swept current density algorithm, we demonstrate improved sensor range by quantifying 5-200 mM chloride with a single sensor. We also investigate sensor reusability and effect of pH, temperature, conductivity, and additional ions relevant to the urinary parameter space. Finally, we investigate sensing systems for conditions where present diagnostic tools are lacking, such as traumatic brain injury. Mild TBI is notoriously difficult to identify, and often relies on invasive computerized tomography scans. In 2018, the Food and Drug Administration approved glial fibrillary acidic protein (GFAP) and ubiquitin c-terminal hydrolase L1 (UCH-L1) biomarkers that elevate after a TBI. However, quantification of these biomarkers is primarily dominated by optical detection systems that are high throughput but are limited by bulky detection systems. To improve portability, we develop an enzymatic sandwich immunoassay for electrochemical identification of TBI biomarkers. We use high throughput optical methods to develop a working assay and translate this protocol to achieve electrochemical detection. We then demonstrate rapid amperometric sensing can be achieved in under 5 s for both GFAP and UCH-L1 biomarkers. Lastly, we propose a design and fabrication process for developing a credit card sized variable height microfluidic platform that can be used to multiplex TBI biomarkers of interest. Overall, this work presents sensing systems that can be employed at the end-point for rapid, portable monitoring to provide actionable data to identify harmful substances, disease, and injury progression.

Chapter 1 Introduction

1.1 Motivation

The desire to monitor environmental and biological samples dates back to the pre-1800s with inventions of pH sensing litmus paper and thermometers[1]. In the following centuries, complex sensing systems have been applied towards environmental[2-5], food[1], and health[6-9] monitoring. As a result, everyday interaction with a multitude of sensors (e.g., temperature, smoke-alarms, COVID tests) has become commonplace. Particularly important is the development of diagnostic sensors to obtain chemical and biological health information (e.g., heavy metal, ion, biomarker concentration) and inform decision making. These devices can be used to identify harmful substances, indicate acute or chronic injury, or monitor response to treatment. Recently, a push towards end-point and near-patient devices has been driving a need for near real-time sensing systems with improved portability, low-cost and simple operation in the fields of water contamination, urinalysis, and medical diagnosis.

Since at least the fourth millennium BCE, humans have been struggling with hazardous lead contaminated drinking water[10]. Lead piping, banned in 1986, was commonly used in water infrastructure and a naturally occurring passivation layer prevented pipe corrosion[11]. When the passivation layer fails from changes in water chemistry or aging infrastructure, large quantities of lead leaches into the drinking water as demonstrated by the Flint Water Crisis in 2014. An estimated 140,000 people were exposed to lead, which can damage the brain and nervous system, and has lasting effects in children[12]. An unknown amount of lead pipes still exist today and are often difficult to access. Lead sensors capable of monitoring drinking water within the

home infrastructure are needed to identify harmful water contamination and prevent future health crises. Ideally, these sensors would be miniature and able to monitor lead presence for long times, with minimal maintenance. By deploying end-point sensors, users can obtain water quality information faster than existing lab testing.

In addition to external monitoring, present quantification of internal body fluids, such as urine and blood, are dominated by time-consuming laboratory testing and could benefit from portable sensing. Urinary chloride monitoring can aid in early detection of serious conditions (e.g. acid base disorder[13, 14], acute heart failure[15, 16]) and determine patient wellbeing (e.g. dietary salt intake[14, 17-20]). However, urinary ion monitoring is limited as ion concentration frequently changes, requiring 24-hour urine collection with long wait times to obtain results[21]. By developing portable, cost-effective and near real-time sensors, a patient or physician could quickly obtain information about one of the most common electrolytes in the body. Sensors could capture frequent ion change, and be coupled with other electrolyte sensors (e.g., Na^+, K^+) to inform diagnostic and treatment decisions in a wide variety of settings (point-of-care, hospital, intensive care unit).

Portable and noninvasive sensors are also needed for conditions that are particularly difficult to identify and monitor, such as mild traumatic brain injury (TBI). TBIs occur after a blunt blow or jolt to the head and the majority of the 69 million annual cases are mild[22] Presently, TBI diagnostics are reliant on qualitative testing, such as the Glasgow Coma Scale and computerized tomography scans. However, the brain scans often reveal no brain injury and expose the patient to harmful radiation[23]. Alternative diagnostic biosensors that identify biomarkers that elevate in blood and serum post-TBI have been emerging as a noninvasive solution. Continual improvements of sensor form factor, cost and portability are needed to

expand the use of these systems toward point-of-care monitoring (e.g., ambulances, battlefields, sporting complexes).

1.2 Prevalent Detection Methods for Ion and Biomarker Monitoring

Traditionally, analytical methods have been utilized for highly accurate quantification of complex samples. For ion detection in water and biological fluids, inductively coupled plasma mass spectroscopy[24] has become favored in the last decade over older methods such as inductively coupled plasma atomic emission spectroscopy[25] and atomic absorption spectroscopy[4, 26]. Typically, these methods require bulky instruments that are housed in a conventional analytical chemistry central laboratory. They tend to have low detection limits, large quantification range, and high sample throughput with multi-element detection[26]. However, they are often expensive, require special training to operate, and have large form factors.

In the twentieth century, small scale chemical and biological sensors were developed to address limitations of traditional analytical techniques, such as cost, portability, and ease of use. These sensors measure chemical or biological reactions that are proportional to the concentration of a particular analyte[27]. With the advent of improved microfabrication processes, sensors were able to be mass manufactured and easily miniaturized. Additionally, the emergence of novel recognition molecules (e.g., antibodies, enzymes, cells, aptamers, and nanoparticles[7, 28]) that influence the selectivity and capture of an analyte of interest furthered sensor development. Today, ions and biomarkers are quantified with a variety of different sensing techniques[2, 29]. The most common examples of successful sensing systems include lateral flow pregnancy tests and electrochemical glucose biosensors. These sensors employ optical and electrochemical detection methods, respectively.

1.2.1 Optical Detection

Optical detection methods quantify species based on their interaction with light intensity or color generation. Specifically, molecules undergo a change in electronic structure that affects how they interact with photons[5]. Common light phenomena include absorption, scattering, fluorescence, chemiluminescence and colorimetry[5, 29]. The simplest form of optical devices are disposable devices often made of low-cost indicator paper (e.g., dipsticks, testing strips). They are easily deployed in the field, but often only provide YES/NO results and are not autonomous. More complex devices with improved quantification range have been developed for multiuse. These devices, such as a plate reader, are high throughput, and easy to use in a laboratory setting. However, they are often large and can be affected by turbidity, humidity, deposits, or debris that interfere with the optical signal.

Colorimetry is one of the most common optical detection methods deployed in the field or in remote settings[20, 30, 31]. Colorimetric methods generate a color change when in the presence of a chemical or physical stimuli[32]. Often, the user will have to add reagents to their sample or use a test strip with immobilized reagents, making these sensors heavily dependent on the user. However, a primary benefit of this method is the ability to see the color change with the naked eye or phone camera which reduces the need for inexpensive and bulky detectors. Disposable devices are often limited in the range and resolution of measurement, and semi-automatic detectors, such as colorimeters and spectrophotometers, have been developed for improved quantification, reusability, and high throughput measurement.

Fluorescent methods have been used to achieve greater accuracy, lower detection limits and improved analyte selectivity[5]. These methods rely on fluorophores (e.g., quantum dots, dyes) that re-emit light after being excited with light. By introducing fluorophores that tag a particular

analyte, complex instrumentation is needed to excite and detect fluorescent behavior. Often, this instrumentation is bulky and requires image analysis software to interpret signal. However, recently portable fluorescent sensors (e.g., handheld, smartphone based) have been developed for low power, inexpensive and rapid sensing[33].

1.2.2 Electrochemical Detection

Electrochemical detection uses the relationship between chemical and electrical energy to produce a quantifiable electrical signal proportional to analyte concentration. Typically, electrochemical sensors contain an electrolytic cell, where electrical energy is added to a system to drive a non-thermodynamically favorable chemical process. The electrochemical cell contains at least two connected electrodes that are submerged in a fluid (or solid), called the electrolyte. Ions in the fluid move and transfer charge at the electrode surface. In an electrolytic cell, charge will travel from the more positive electrode (anode) to the more negative electrode (cathode). Three electrode systems are also common with a working, counter, and reference electrode. The working electrode (WE) is defined as the electrode where the reaction of interest occurs. The counter electrode (CE) balances charge on the working electrode and completes the circuit and the reference electrode (RE) serves as a stable reference point when measuring cell potential. Common electrochemical methods include conductimetry[34], electrochemical impedance spectroscopy[9, 35] potentiometry[36], amperometry[37], voltammetry[38-40], and chronopotentiometry[41, 42]. Electrochemical sensors are often cost-effective, rapid, selective, sensitive, and easily miniaturized which make them advantageous when developing near real-time diagnostic and monitoring devices. Yet, electrochemical sensors can have poor sensitivity, reproducibility, and stability[4]. The reference electrode often has an internal standard solution leading to increased maintenance and shorter lifetime.

Conductimetry and electrochemical impedance spectroscopy are valuable techniques that determine bulk properties. Conductimetric sensors, such as a conductivity sensor, measure a bulk solution resistance and are not species selective[3]. With these sensors, no chemical reaction occurs. They are useful in determining the total ion concentration or conductivity of a solution but are limited in ability to identify a specific ion or biomarker. Electrochemical impedance spectroscopy (EIS) is an emerging technique that applies an AC signal to a electrochemical cell over a wide range of frequencies and measures the resulting current or voltage response[35]. EIS is particularly valuable in that it can fit collected data to an equivalent electrical circuit to predict bulk properties, such as capacitance and solution resistance associated with an electrochemical cell. However, care must be taken with choosing a particular circuit that represents the electrochemical cell being studied. EIS is often used to interpret the quality of sensors that achieve selectivity through surface modification[6, 43-45].

Potentiometric sensors measure a chemical reaction at equilibrium. Equilibrium potential is measured between two electrodes (i.e., working and reference) with a high impedance voltmeter that has near zero current[3]. These sensors often have a membrane (e.g. porous, glass, crystalline, polymer) containing ionophores, which carry specific ions through the membrane. The potential difference is a function of ion concentration from the ion exchange or transport through a membrane and sample interface[46]. ISEs are commonly used in pH meters and hospital electrolyte analyzers to accurately detect a variety of ions (e.g., Na^+, K^+, Ca^{2+}, and Cl^-) present in blood, serum, and urine. However, it is critical in measuring potential to prevent drift or instability of the reference electrode and thus, frequent electrode maintenance is needed. Much like traditional analytical methods, ISEs are expensive, have a large footprint, and require trained personal to operate and maintain.

Amperometry and voltammetry methods manipulate an applied potential and measure the resulting current response in three electrode cells. Amperometry uses a constant applied potential and voltammetry uses a swept potential or ramping methods. Common voltammetric techniques include differential pulse voltammetry[46], cyclic voltammetry[47], and anodic stripping voltammetry[5]. Amperometric and voltammetric sensors are advantageous as they use careful potential control to selectively react a particular species and often have very low detection limits (e.g., picomolar)[3]. However, chemical modification of electrode surface or addition of control species, and reference electrode maintenance are often needed.

Chronopotentiometry is the opposite of amperometric and voltammetric methods. In chronopotentiometry, current is applied to the cell with simultaneous potential measurement. The selected applied current directly influences the rate at which a reaction can occur and can cause measurable local ion depletion of the analyte of interest. Additional information on the theory of chronopotentiometry can be found in Chapter 3.2. This method is advantageous as it does not rely on a reliable reference electrode and thus, has been shown to be better for developing long-term sensors with unmodified pseudo-reference electrodes[42, 48]. Additionally, by using a pseudo-reference with no internal standard, sensors can also be easily miniaturized. However, they can be susceptible to surface fouling which could impact their reusability and lifetime.

1.3 Organization of this Dissertation

The work presented in this dissertation is motivated by the need to monitor the presence of ions and biomarkers at the point of application to inform health decisions. We have chosen to focus on utilizing electrochemical sensing strategies as they are rapid, cost-effective and are easily miniaturized with portable measuring instrumentation. A summary of each chapter of this dissertation with each electrochemical sensing method presented can be found in Table 1.1.

Table 1.1:Guide to each electrochemical sensing strategy employed in this dissertation.

	SENSOR DEVELOPED	DRIVING SYSTEM	REACTION EVENT	SIGNAL	SENSING TYPE(S)
CHAPTER 1	Introduction to many sensing techniques	-	-	-	Optical, Electrochemical Methods
CHAPTER 2	Lead Ion	Constant potential applied between anode/cathode	Lead ions oxidized onto sensor	Potential across load resistor	Conductometry
CHAPTER 3	Chloride Ion	Current applied between WE/CE	Chloride ions oxidize onto sensor	Potential between WE/RE	Chronopotentiometry
CHAPTER 4	TBI Biomarkers	Potential applied between WE/RE	TMB^{+} ions reduce in solution	Current between WE/CE	Amperometry
CHAPTER 5	Conclusion and Future Work	-	-	-	-

In Chapter II, we present a four-electrode sensor that reliably responds to electrodeposited lead oxide to provide a near real-time indication of lead ion presence. To better understand the detection mechanism, we investigate the temporal and spatial electrochemical deposition of lead using potential response data, scanning electron microscopy, fractal dimension, and COMSOL Multiphysics® finite element analysis. Our results suggest that the deposition of lead oxide on the sensor is diffusion limited. By applying the learnings from this study, we improve the detection time and reliability of the sensor signal through changes in sensor design and operation.

In Chapter III, we demonstrate the applicability of chronopotentiometry for urinary chloride detection with readily available screen-printed electrodes. The sensor signal is based on a time at which all chloride ions locally deplete at the surface of a silver electrode, also known as the transition time. Initially, the sensor performance was optimized through proper selection of current density at a specific chloride concentration using electrical response data in conjunction with scanning electron microscopy. We then developed a unique swept current density algorithm to resolve the entire clinically relevant chloride concentration range, and the chloride sensors can

be reliably reused at chloride concentrations less than 50 mM. Lastly, we explored the impact of pH, temperature, conductivity, and additional ions (i.e., artificial urine) on the sensor signal to determine sensor feasibility in complex biological samples. This study provides a path for further development of a portable, near real-time sensor for quantification of urinary chloride.

In Chapter IV, we develop an enzyme sandwich immunoassay for quantifying traumatic brain injury biomarkers. We use optical absorbance methods to develop a working assay protocol capable of detection of relevant traumatic brain injury biomarkers. We investigate reagent concentration and incubation time on assay signal and limit of detection. We then provide calibration curves for both optical and electrochemical detection of two relevant biomarkers. We conclude by providing an electrochemical device design based on calculations that account for diffusion to develop a device capable of multiplexing biomarkers. This work provides preliminary research into developing an electrochemical sensing system capable of quantifying multiple TBI biomarkers.

In Chapter V, we finish the dissertation with a summary of each electrochemical sensor developed, our ideas for future follow-up research, and concluding remarks on the future of this field.

Chapter 2 Electrochemical Deposition of Lead for Water Quality Sensing

This work was done in collaboration with Dr. Sanaz Habibi and Dr. Jaesung Lee. My contributions include the design of the original study, discussions with Dr. Sanaz Habibi, sensor fabrication, and lead sensor testing. Dr. Jaesung Lee's contributions include the electrode geometry design, collection of SEM images for the time and spatial study, and creation of the MATLAB code.

2.1 Introduction

Water infrastructure containing lead has the potential to cause great harm to humans. Lead is a neurotoxin that, when consumed, can slow growth and development of children and cause damage to the nervous system[49, 50]. Prior to 1986, lead was widely used in residential plumbing including service lines, solder, and brass fittings. Changes to water chemistry can cause corrosion of a pipe's passivation layer, allowing lead and other heavy metals to leach into the drinking water source[51, 52]. Corrosion events often occur within individual homes and contaminate clean water from the water utility source. Although no level of lead is safe to consume, the Environmental Protection Agency (EPA) and European Union (EU) have set a maximum action lead level of 15 part per billion (ppb) and 10 ppb, respectively[39]. In the United States, the EPA estimates that there are 6 – 10 million lead service lines still used to deliver water in homes[53]. Thus, a sensor capable of alerting the homeowner that lead is present within their home could accelerate the detection of a corrosion event, monitor the water quality, and determine the need for plumbing replacement.

Currently, traditional analytical methods are the gold standard for accurate and sensitive lead detection but are resource intensive and do not provide continuous monitoring. Analytical methods include inductively coupled plasma atomic emission spectroscopy (ICP-AES)[25], inductively coupled plasma mass spectroscopy (ICP-MS)[24], and atomic absorption spectroscopy (AAS)[4]. Despite traditional analytical methods' accuracy and sensitivity, these methods are expensive, require highly trained operators, involve complicated and laborious pre-treatment processes, and take days or weeks to provide test results. Furthermore, water samples need to be collected by a homeowner and transported to a certified laboratory, requiring the diligence of homeowners to regularly test their water for lead contamination. Thus, a simple and inexpensive method is desirable for near real-time monitoring of a water sample.

Colorimetric and electrochemical sensors are being explored to address the need for lead detection and monitoring in the individual home[4, 5, 54-58]. As these sensors are miniature, portable, have fast detection times, and do not require trained operators, they are ideal for home use where contaminated lead infrastructure is often located[5]. Among these various detection technologies, colorimetric sensors are the most convenient methods due to their simplicity, but they are single use and often require the homeowner to add testing reagents to their water sample. Electrochemical sensors are accurate and detect dilute concentrations of 1-150 ppb lead[4], but contain reference electrodes that can become unstable over time, making unsuitable for long-term monitoring of lead contamination.

To create sensors that continuously operate at long time scales, Lin *et. al* developed a four-electrode system (positive anode, negative cathode, and two floating electrodes) to detect 15 ppb lead ions with no false responses in 3 days without the need for reference electrodes[56]. The anode and its neutral floating electrode create a locally acidic environment, while the cathode

and its neutral floating electrode generate a locally basic environment. Lead detection takes place when the gap between the anode and the adjacent floating electrode is bridged by a lead oxide deposition. However, lead detection in that system could take several days to trigger a response.

In this study, we aim to understand and achieve more effective sensor detection strategies for identifying electrodeposited lead oxide on a microelectrode sensor based on the four-electrode system[56]. Initially, we designed a new four-electrode system and demonstrated successful lead oxide deposition. In order to shorten the lead sensor detection time and improve the stability of the detection signal, we investigated temporal and spatial behavior of lead oxide deposition and its underlying mechanism. Lead deposition was examined with respect to time, the gap between the anode/cathode and the adjacent electrodes (3-12 μm), and the absence or presence of agitation. Potential response data and scanning electron microscopy (SEM) images were obtained to further understand lead oxide deposition.

2.2 Materials and Methods

2.2.1 Sensor Design and Fabrication

To detect lead presence in drinking water, a 300/1000 Å Ti/Pt four-electrode sensor was designed and fabricated as shown in Figure 2.1a. The four-electrode system consists of an anode (+), anode's adjacent floating electrode (F2), cathode's adjacent floating electrode (F3), and a cathode (-). Here, F2 and F3 serve as a reference point to determine if conductive materials are present. The gap between the two adjacent electrodes (e.g., anode and F2) was designed to be 3, 5, 8, 10 and 12 μm. Photolithography, electron beam evaporation, and lift-off were employed to fabricate the electrodes on borofloat wafers (Precision Glass & Optics) following published procedures.[56] The borofloat wafers were diced into 2.0 mm × 3.6 mm pieces. Each wafer

produced approximately 500 sensors. Fabricated sensors were epoxied (Loctite) to custom printed circuit boards (PCBs) and were electrically connected by Gold ball wirebonding (Model 4124, Kulicke & Soffa) and protected by epoxy encapsulation (Loctite). Wires connecting the sensors to the LabVIEW test setup were soldered to the other end of the PCBs.

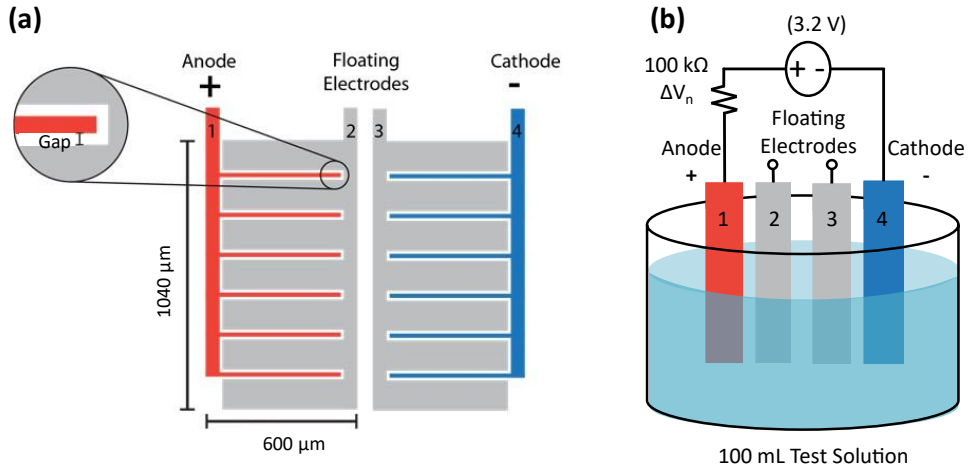


Figure 2.1:(a) The schematic diagram of the four-electrode system. (b) Sensor schematic with three different sensing configurations including: deposition mode (ΔV) between anode and cathode, lead measurement mode (ΔV_1) between anode and F2, and heavy metal measurement mode (ΔV_2) between F3 and cathode

2.2.2 Chemicals and Test Solution Preparation

Lead (II) chloride ($PbCl_2$) and sodium chloride (NaCl, >98%) were purchased from Sigma-Aldrich (St. Louis, MO, USA). All experiments were conducted in 0.01 M NaCl with a conductivity of 1000 µS/cm, the upper limit in drinking water[59]. The lead test solutions were adjusted to 15 ppb $PbCl_2$ using deionized water. Control solutions consisted of 0.01 M NaCl and deionized water.

2.2.3 Experimental Setup

The experimental setup uses LabVIEW Data Acquisition software to operate at three different modes: deposition mode (anode-cathode), lead measurement mode (anode-F2), and heavy metal measurement mode (F3-cathode). The sensor was connected in series with a 100 kΩ

load resistor and a 3.2 V DC power supply (Figure 2.1b). The sensor was submerged in 100 mL of test solution and ran in deposition mode for one hour. Next, the LabVIEW Data Acquisition software recorded potential measurements across the load resistor every hour for 3 minutes in deposition mode (ΔV), lead measurement (ΔV_1) mode and heavy metal measurement mode (ΔV_2). A MATLAB program determined the average potential for each operating configuration by averaging five data points across the span of the 3-minute recording. The sensor triggered after the load resistor in lead measurement mode (ΔV_1) reached a 1 V threshold potential. Tests have been conducted in stagnant and agitated solution. Agitated solutions were mixed by placing a 15.9 mm × 8.0 mm stir bar in solution on a stir plate.

2.2.4 Scanning Electron Microscopy

All SEM images were taken with a Field Emission SEM (Hitachi SU8000 In-Line) in the secondary electron detection mode. Samples were mounted on a 4" wafer mount and loaded into the machine. A 2 KV acceleration voltage and a 7 μA emission current were used. It should be noted that the SEM images were taken following the electrical measurements, rinsing the sensor with deionized water, and preparing the sensor for SEM imaging. The presence of lead on the sensor was confirmed by Energy Dispersive X-ray Spectroscopy (EDS, Bruker Quantax 200) with a 5 KV acceleration voltage and a 7 μA emission current.

2.2.5 Fractal Dimension

Fractal box-counting method was employed to calculate fractal dimension (f_D) of the electrodeposited structure between the anode and F2. The f_D analysis was performed on the SEM images of six different lead sensors after applying potential for 6, 12, 18, 24, 48, and 72 hrs. Individual SEM images were analyzed with ImageJ® software and ImageJ® plugin FracLac V

2.5 software developed by Karperien[60]. Briefly, using ImageJ® software, a threshold was applied to the SEM images to distinctly separate pixels of the electrodeposited structures from those in the background. Next, the area of interest was selected by manually removing the anode and F2 from the SEM images. Using plugin FracLac V 2.5, the box-counting method was executed. SEM images were automatically converted into binary images and covered with grids of boxes. The software counts the number of boxes (N) that covers the structures and contains the pixels of interest. The pixels of interest are considered to contain meaningful information while other pixels are background or noise. Finally, the f_D is calculated as follows:

$$f_D = \lim_{\varepsilon \to 0} \frac{\log N}{\log \varepsilon} \tag{2.1}$$

where ε is the length scale and is equal to the box size divided by the image size. f_D is a unit-less measure and can be calculated by measuring the negative slope of $\log N$ versus $\log \varepsilon$. When the f_D value nears 2, the growth is more of a compact cluster, while an f_D value of 1 indicates the growth is closer to a one-dimensional structure[61].

2.2.6 Lead Ion Transport Simulation

Lead ion concentration gradient and flux were numerically modeled with COMSOL Multiphysics® 5.5. The lead ion transportation was adapted from Lupo *et. al*[62, 63]. Due to the symmetry of the four-electrode system, the geometry was modeled and contained the electrolyte, anode, and F2. "Transport of Diluted Species" and "Level Set" were used to simulate the concentration gradient and ion flux. The transport module solved the diffusive term of the Nernst-Planck Equation[64]. The initial concentration of the lead ion was defined as 0 mol/m^3 at the anode, and 15 ppb (7.24×10^{-5} mol/m^3) a distance of 15 µm away from the sensor in the z direction. The F2 and electrolyte regions between electrodes were assumed to have a no flux

boundary condition. To save computation time, the mesh was defined to be coarser at a distance of 5 to 15 µm away from the electrode interface with a maximum element size and growth rate of 1.34 µm and 1.25, respectively. At the anode boundary, the mesh contained a maximum element size and growth rate of 0.43 µm and 1.1, respectively.

2.3 Results and Discussion

2.3.1 Lead Sensor Detection Mechanism

We designed and fabricated an interdigitated four-electrode sensor capable of detecting lead in drinking water with no false positive results (Figure 2.1). As previously described[56], the four-electrode lead sensor operates by depositing lead oxide onto the anode. The sensor returns a positive signal for lead when the lead oxide bridges the gap between the anode and the adjacent floating electrode, F2. The presence of lead oxide in this gap lowers the resistance between the anode and F2 thus increasing the potential across the load resistor. Lin *et. al* demonstrated the four-electrode sensor can also detect other heavy metals (i.e., Zn^{2+}, Cu^{2+}, and Fe^{2+}) between the cathode and F3 and found that other heavy metals had minimal effect on the lead detection capability[56]. Figure 2.2a shows the electrical potential signal at three different operational modes: deposition mode, heavy metal measurement mode, and lead measurement mode. Lead solutions did not trigger a response during the deposition and heavy metal measurement modes. In the lead measurement mode, the initial potential (ΔV_1) was below the 1 V threshold potential before 18 hrs, oscillating below and above 1V between 18 and 32 hrs, and above 1V after 32 hours. The rise in potential served as the detection signal for the presence of lead oxide on the sensor and, therefore, lead in the contacting solution.

The detection signal is based on depositing conductive lead oxide and bridging between the anode and F2 to trigger the sensor. To visually capture this bridging event, SEM images were studied over time as illustrated in Figure 2.2b. Prior to 18 hrs, SEM images show fast linear growth of lead oxide deposition and correspond to the observed constant ΔV_1 in Figure 2.2b. Following 18 hrs of lead oxide deposition, the deposited material starts to bridge the gap between the electrodes which coincides with the oscillating potential response. At this stage, lead oxide structures are similar to very thin wires and can easily break with the passage of current during the lead measurement mode. The interplay between connection and breakage appears to slow down the overall rate of lead oxide growth as observed in Figure 2.2c. By 72 hrs, the electrical potential signal stabilizes as a thick layer of deposited lead oxide fills the electrode gap. The presence of sufficient material between the electrodes to carry the current can eliminate the stress caused by the measurement process. Note that the lead oxide deposition has a growth rate between 0.05 and 0.15 μm/hr as indicated in Figure 2.2c. Additionally, control lead-free test solutions did not trigger a detection signal in the lead or heavy metal measurement modes as shown Figure 2.3.

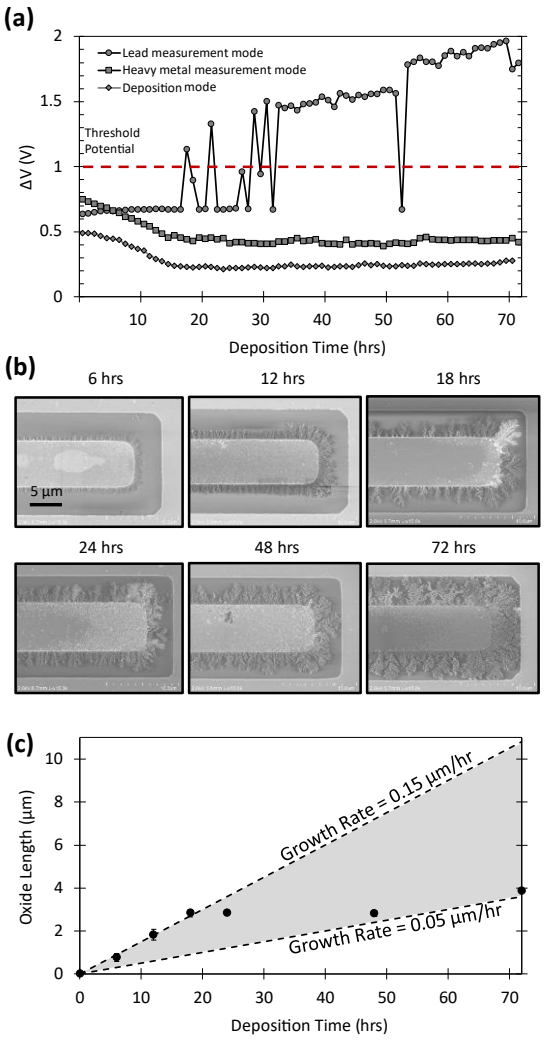


Figure 2.2:(a) Potential (ΔV) signal versus time at three different operational mode: deposition mode, lead measurement mode, and heavy metal measurement mode. (b) The SEM images were taken and studied for six different sensors stopped after 6, 12, 18, 24, 48, and 72 hrs. SEM images show lead oxide growth over time at the tip side of the first anode digit. Sensors were rinsed with deionized water prior to imaging. (c) Deposited lead oxide length over time with a growth rate between 0.05 and 0.15 µm/hr. All devices had a 5 µm gap between anode and F2. Tests were conducted with lead solutions of 15 ppb $PbCl_2$, 0.01 M NaCl, and deionized water.

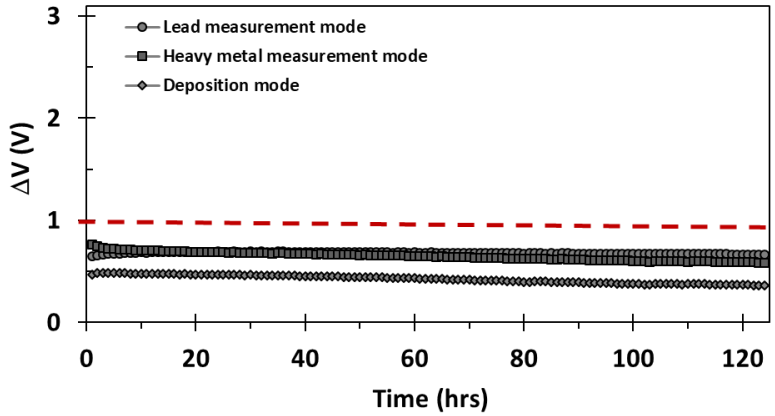


Figure 2.3:Potential (ΔV) signal versus time at three different operational mode: deposition mode, lead measurement mode, and heavy metal measurement mode in control solution of 0.01 M NaCl using the 5 µm device geometry.

As further support, lead and oxygen composition in the EDS spectra of the electrodeposits suggests the formation of lead oxide. An EDS Spectra of a broken fragment consistent with the observed electrodeposit morphology was analyzed on the Pt anode. In Figure 2.4, the spectra clearly demonstrate a lead and oxygen peak being present in addition to a large Pt peak around 2 keV. Thus, the elemental analysis indicates lead is most likely present in the form of an oxide. Auger spectroscopy has also pointed to the electrodeposits being most likely lead oxide in development of past sensor geometries[65]. The EDS Spectra demonstrated in Figure 2.5, shows a smooth formation that contains sodium and chloride ions, which is consistent with the added supporting electrolyte of NaCl.

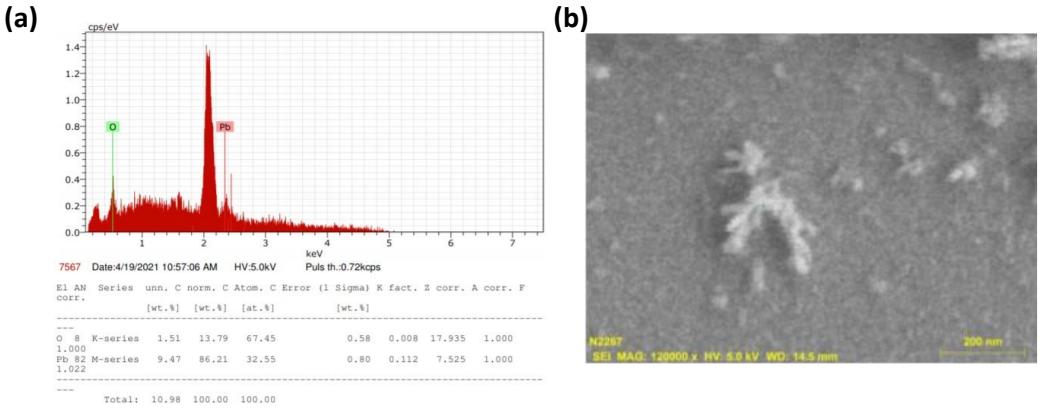


Figure 2.4:(a) EDS Spectra composition of a broken lead fragment on Pt electrode. Large peak at ~ 2 keV is from Pt. (b) SEM Image of analyzed area in 5 µm gap distance device.

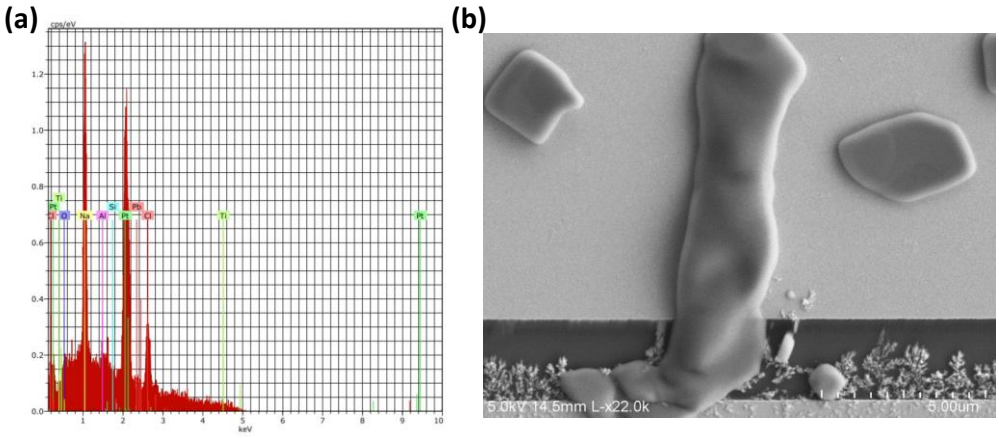


Figure 2.5:(a) EDS Spectra Composition of lead presence in 5 µm gap between anode and F2. The smooth particle covering the gap is believed to be NaCl. (b) SEM Image of analyzed area.

The relatively slow process of oxide growth to bridge the electrodes is due to the limitation caused by ion diffusion and is supported by the observed morphology. As shown in Figure 2.2b, the morphology agrees well with an open fractal pattern suggesting the ions are performing a random walk and aggregating one-by-one (i.e., a diffusion mechanism)[66, 67]. The open fractal patterns of lead oxide deposits are self-similar with a non-uniform growing front with respect to electric field lines and continuous tip splitting facilitating growth into a tree-like structure. The open fractal structures that emerge from this process can be described by the fractal dimension,

f_D, which is an index for quantifying open fractal pattern complexity as a ratio of the change in detail ($\log N$) with respect to the change in scale ($\log \varepsilon$). As shown in Figure 2.6, the f_D of the lead oxide formation varied between 1.65 to 1.74, which is approximately consistent with the diffusion limited value of 1.71 reported in the literature[61, 68].

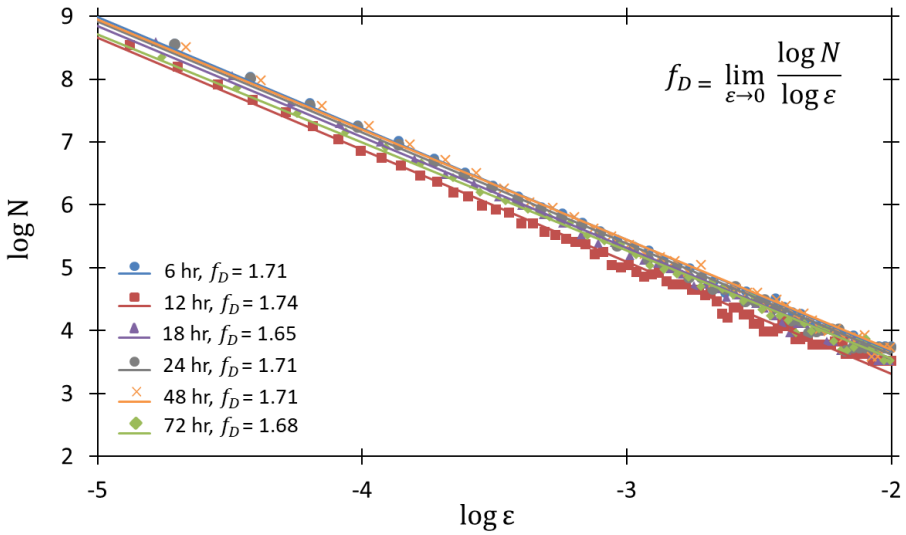


Figure 2.6:A plot of log N versus log ε using the box-counting method gives a fractal dimension f_D = - slope. The f_D of six different lead sensors were found to be 1.71, 1.74, 1.65, 1.71, 1.71, and 1.68 after 6, 12, 18, 24, 48, and 72 hrs, respectively. Devices had a gap distance of 5 µm. Lead sensors were tested in 15 ppb lead solutions

2.3.2 COMSOL Multiphysics® Simulation of Lead Ion Diffusion

The diffusion-limited growth was modeled with COMSOL Multiphysics® simulations and agreed with the spatial observation of lead oxide deposition across the anode. Generally, in dilute systems, the ion flux, $\boldsymbol{N}_i$, is governed by diffusion, migration, and convection:

$$\boldsymbol{N}_i = \underbrace{-D_i \nabla C_i}_{\text{flux}} \underbrace{-F z_i C_i u_i \nabla \Phi}_{\text{diffusion}} \underbrace{+ \mathbf{v} C_i}_{\text{migration}} \underbrace{}_{\text{convection}} \tag{2.2}$$

where D_i is ion diffusivity, C_i is the bulk ion concentration, F is Faraday's constant, z_i is the ion charge, u_i is the ion mobility, Φ is the electric potential, and **v** is the bulk velocity. In stagnant solutions that contain highly conductive supporting electrolytes, convection and migration can be assumed to be negligible[69]. Thus, Eq. (2.2) simplifies to:

$$\boldsymbol{N}_i = \quad -D_i \nabla C_i \tag{2.3}$$

For a diffusion limited mechanism, the ion flux is primarily driven by the concentration gradient. Figure 2.7a shows the 2D cross-sectional plot of the concentration gradient in the x-z plane at y=0. The anode tip (E_1) and near-anode tip (E_2) are identified as the area of interest across the 1st anode digit. After 12 hrs, a drastic drop in concentration occurs at the anode tip (E_1) because this area receives a greater supply of ions giving rise to a larger concentration gradient. The large gradient at the anode tip is beneficial as the detection mechanism of the sensor relies on lead bridging across the anode and F2.

To correlate ion flux with the spatial observation of lead oxide deposition across the 1st anode digit, two additional area of interest were identified at the anode corner (C) and anode palm (D). Figure 2.7b shows the ion flux across the x direction at z= 0.2 μm. The ion flux is largest at the anode tip (E_1) and corner (C), resulting in a greater possibility of forming electrodeposits at these locations. The simulated results agree with the increased deposition experimentally observed in SEM images, as shown in Figure 2.7c and Figure 2.7e. At the center of the anode (between D and E_1), the ion flux decreases significantly resulting in less deposition displayed in Figure 2.7d and Figure 2.7e.

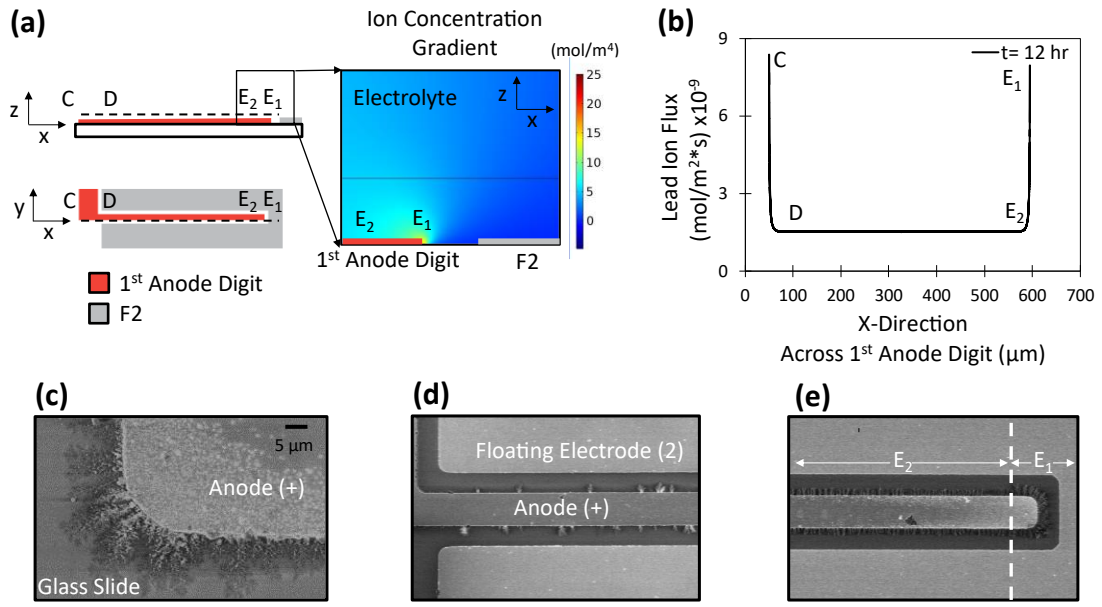


Figure 2.7:(a) Schematic of lead sensor geometry with deposition areas of interest. The ion concentration gradient is shown in the area closer to the anode tip generated with COMSOL®. (b) COMSOL® simulation of spatial dependence of Pb^{2+} ion flux versus location along the 1st anode digit was plotted at 0.2 µm above the surface in the z direction. The SEM images of (c) anode corner, (d) anode palm, and (e) anode tip after 12 hrs of lead deposition in 15 ppb lead solution. Sensor was gently washed with deionized water prior to imaging and had a 5 µm gap distance.

2.3.3 Shortening and Improving the Stability of the Detection Signal

The simplest way to decrease the detection time of the sensor is to reduce the gap distance between the anode and F2. As previously shown in Figure 2.2, lead detection in the sensor geometry is a function of the time it takes for the lead oxide to form and bridge the gap between electrodes. To study the effect of gap distance on sensor detection time, sensors with different gap (3, 5, 8, 10, and 12 µm) were fabricated. Table 2.1 summarizes the average actual gap distance, electrode width, and detection time of each studied device geometry. Figure 2.8a shows a representative curve for each gap distance. The oscillation period and detection time are significantly shorter with smaller gap distances of 3 and 5 µm, as smaller amounts of lead oxide deposits are needed to bridge the gap between electrodes. Figure 2.8b illustrates the average detection time versus gap distance. The dispersion of average detection time for 3 and 5 µm gap sensors is relatively low with the values of 19.8 ± 3.04 and 33.2 ± 5.44 hours, respectively. The

rate of lead oxide growth was found to be between 0.05 and 0.15 µm/hr, and agrees with the growth rate range calculated in Figure 2.2c. Note that, for short distances in Figure 2.2c and Figure 2.8b, the growth rate appears to be linear and a constant value of 0.15 µm/hr. While this phenomenon is associated with the morphology of the growing lead oxide, further investigation is needed to determine the exact mechanism and to validate that the region truly involves linear growth. The growth rate, as determined by the relationship between gap distance and detection time, can also be used to envision an improved detection time with a smaller gap sensor (e.g., sub-micron made via nanopatterning) below what was possible in this work (i.e., 3 µm gap).

*Table 2.1:Device geometries respective geometrical parameters and response time in lead measurement mode (ΔV_1). *Two of the devices did not respond after running the deposition for 233 hrs.*

Average Actual Gap distance (µm)	Average Actual Electrode Width (µm)	ΔV_1 Response Time (hrs)	Number of tested sensors
2.94 ± 0.29	5.13 ± 0.23	19.7 ± 6.0	4
5.13 ± 0.39	5.00 ± 0.24	33.1 ± 13.6	6
8.04 ± 0.29	4.56 ± 0.17	96.8 ± 29.1	5
10.18 ± 0.20	4.54 ± 0.13	173.6 ± 117.1	3
12.38 ± 0.25	4.59 ± 0.20	146 ± 36.3	5*

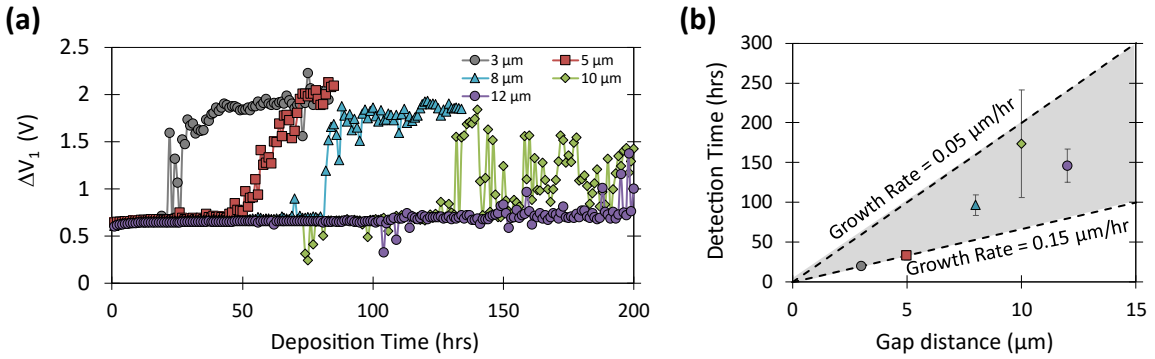


Figure 2.8:(a) A representative potential signal curve for each gap distance in lead measurement mode. All experiments were conducted with 15 ppb lead solution. (b) The average detection time versus gap distance ($n \geq 3$ sensors) between anode and F2 with a growth rate ranging between 0.05 and 0.15 µm/hr.

Electrolyte agitation was employed to facilitate transport of lead ions to the electrode surface and resulted in more stable electrical potential signals. The electrical response of three lead sensors are plotted for stagnant and 360 rpm agitated lead solutions in Figure 2.9a and Figure 2.9c, respectively. The electrical response of a stagnant lead solution exhibits noisy signals oscillating around the threshold potential, while electrical response of the agitated lead solution produces a smooth curve that reaches a steady potential. Additionally, two sensors (i.e., lead sensor 1 and 2 in Figure 2.9c) show stronger signal response during agitation with a ΔV_1 larger than 2 V when triggered. Note that the agitated solution created a laminar flow regime, which demonstrates that the sensor can perform well in conditions consistent with the real world (e.g., laminar faucet flow). Further studies are needed to understand the effect of water flow in a turbulent regime on sensor performance.

The improvement of signal stability could be due to the morphology of the electrodeposited material, which has been shown to be influenced by agitation[70-72]. Compared to the stagnant solutions (Figure 2.9b), the SEM images of agitated solutions (Figure 2.9d) were more densely packed, had a growing front that varied in direction, and were more uniformly distributed across the anode. In agitated solutions, the dense nature of the lead oxide structures could contribute to the stable signal observed during experiments. When agitating a solution, the diffusion layer thickness decreases[73] causing the rate of ion diffusion to increase. As more ions are closer to the surface of the electrode in agitated solutions, denser structures are more likely to form.

To study the lead oxide growth mechanism during agitation, the SEM images were horizontally divided at the center of the image into the top and the bottom regions, and the resulting segmented images were used to calculate f_D. Despite increasing the ion transport to the

surface of the electrode, f_D of the top region is similar to that of stagnant solutions. However, the f_D of the bottom region was found to be 1.82 ± 0.04 displaying deviation from the fractal patterns by forming denser structures. As stated previously, the formation of these dense structures greatly improves the sensor's potential signal stability.

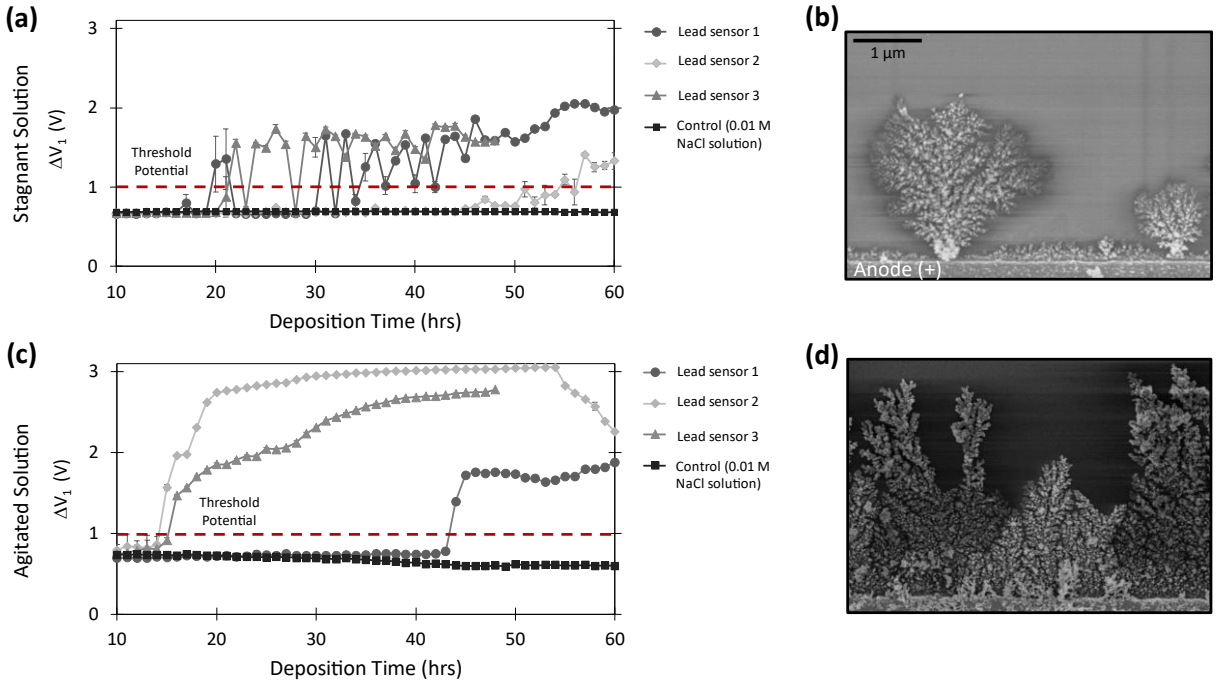


Figure 2.9:Potential signal during lead measurement mode (ΔV_1) for (a) stagnant solutions and (c) 360 rpm agitated solutions. Each curve represents a unique device in isolated experiment. SEM images of sensor in (b) stagnant and (d) 150 rpm agitated solutions. Each curve represents a unique device in isolated experiment. SEM images of sensor in (b) stagnant and (d) 150 rpm agitated solutions. Each SEM image was taken in different devices with 5 µm gap distance that both ran for ~27 hours in 15 ppb lead solution.

2.4 Conclusion

The lead sensor described in this work uses electrodeposition of lead oxide to reproducibly and reliably detect the presence of lead in aqueous solutions. The deposited oxide forms structures that bridge the gap between the anode and the adjacent floating electrode. The deposition is diffusion limited, and faster sensor response can be obtained by reducing the gap between the bridged electrodes, shortening detection times in our experiments by 40%. In

agitated flow conditions, the sensor has been shown to have more stable electrical potential signals, and the laminar flow regimes at the end point of water service lines or in individual faucets would be similar to those conditions. Lead sensor performance can be further improved by masking the areas of the electrode (e.g., connecting wires, anode corner) that are not near a floating electrode to prevent deposition of lead in undetectable regions. With minor changes, the resulting miniature, sensitive, and user-friendly sensors can easily be deployed in a variety of water infrastructure and can generate actionable data to prevent consumption of lead during a corrosion event.

Chapter 3 Electrochemical Sensing of Urinary Chloride Ion Concentration for Near Real-Time Monitoring

This work was conducted with close collaboration with Dr. Sanaz Habibi. My contributions to the project include design of the original study, experimental data collection and analysis.

3.1 Introduction

Urinary chloride is a versatile, readily available biomarker for diagnosing and monitoring a wide variety of diseases involving kidney and circulatory health. As the most abundant extracellular anion[74], chloride accounts for 70% of the total anion concentration in the body[75, 76], and is responsible for regulating the extra/intracellular volume[74], maintaining acid/base equilibrium[15, 74, 75, 77], and upholding muscular activity[75, 77]. As a mobile ion that is primarily regulated through kidney excretion[78, 79], urinary chloride is physiologically dynamic. Timed spot and 24-hour sample collection are often needed to account for intra- and interday variations and to capture ion changes[21], which can aid in early disease detection and monitor organ health. Specifically, chloride concentration has been shown to be an indicator for prerenal acute kidney disease[74], acid-base disorders[13, 14], dietary salt intake[14, 17-20], and acute heart failure[15, 16]. Recently, lower chloride concentrations (<53 mM) have been linked to higher mortality in critically ill patients in the intensive care unit (ICU)[77]. To quantify and monitor chloride ion concentration, a chloride sensor is needed to quickly detect ion change. Thus, a near real-time sensor could accelerate detection of disease, monitor organ health, and inform treatment decisions.

Traditional analytical techniques have been employed as the gold standard to accurately quantify chloride concentration. Analytical techniques include ion chromatography[30, 80], colorimetry[19, 20, 79], fluorescence[30], and potentiometric ion selective electrodes (ISE)[36, 46, 81]. Potentiometric ISEs are most commonly employed in electrolyte analyzers used in hospital settings[17], as they are accurate and reliable; however, they rely on a consistent reference electrode, which is difficult to miniaturize, requires an internal solution, and requires constant recalibration to remain stable[46]. Electrolyte analyzers are capable of accurately quantifying multiple ions, but tend to be expensive, have a large footprint, and require time-consuming calibration. Furthermore, analyzers require processing samples in a certified lab, which can be a time-consuming process. Thus, simple and cost-effective sensors are needed to achieve near real-time chloride monitoring. For example, such sensors could be integrated into a wearable uroflowmeter[82].

Optical chemosensors[19, 79, 83, 84] and electrochemical sensors[9, 38, 42, 43, 48, 85, 86] have been investigated for cost effective, near real-time chloride detection. Optical chemosensors are typically paper-based sensors[20, 30, 31] (e.g., dipsticks); due to their portability, they have been widely used in qualitative field studies[46]. However, optical chemosensors are typically single use, and often require adding reagents (such as fluorescent probes, quenching agents) to obtain results. Thus, they are not suitable for long-term near real-time monitoring of urinary chloride.

Electrochemical sensors are often reusable, and can be used for long term measurement[46]. Aside from potentiometric ISEs, common electrochemical techniques include electrochemical impedance spectroscopy (EIS)[9, 87, 88], voltammetry[38, 40, 85, 89], and chronopotentiometry[42, 48, 86]. EIS is an emerging technique used in development of sweat chloride sensors[6, 43-45] where complex modification of the electrode surface (e.g., ionophores) is required to achieve chloride

selectivity. Voltammetric sensors also may need complex chemical surface modification, and often detect a smaller resolvable range; however, they can detect low concentrations of chloride (10^{-6} M)[46]. Chronopotentiometric sensors are advantageous, as they rely on measuring a potential shift and not an absolute potential; thus, a pseudo-reference electrode can be used. The pseudo-reference electrode only needs to maintain stability during short measurement times, which makes the sensor ideal for miniaturization and long-term measurement[86]. To the authors' knowledge, chronopotentiometric sensors have never been optimized for detecting urinary chloride, but the technique shows promise for developing a portable and near real-time urinary chloride sensor, with no required sample preparation.

In this study, we developed a chronopotentiometric sensor capable of measuring a physiologically relevant range[21, 77] of chloride ion concentrations (5–250 mM), using simple silver electrodes with no surface modification or added reagents. We studied the influence of the chloride ion concentrations effect on the sensor signal and identified current densities that can resolve different concentration ranges. To determine the optimal current density for a particular chloride concentration, we electrically and optically characterized the surface of the working electrode by interpreting chronopotentiograms, scanning electron microscopy (SEM) images, and energy dispersive spectroscopy (EDS) spectra. We developed a novel current density sweeping algorithm that allows resolution of the relevant chloride concentration range with a single sensor in 3 s (25–200 mM). Furthermore, we demonstrated reusable sensors that could be suitable for long-term measurement. Lastly, we investigated the effect of pH (4.4–7.7), temperature (25–37 °C), conductivity (1.1–7 S/m), and additional ions (i.e., artificial urine) on the chronopotentiometric signal of our sensor.

3.2 Theory

As shown in Figure 3.1a, a constant current is applied between the working and counter electrode of the sensor, and the applied current induces a faradaic reaction on the surface of the working electrode. The silver working electrode will react with chloride ions in the electrolyte to form a solid silver chloride deposit, as shown in Equation (3.1):

$$\mathrm{Ag(s)} + \mathrm{Cl-(aq)} \rightarrow \mathrm{AgCl(s)} + \mathrm{e^-} \quad (3.1)$$

When the mass transport of the chloride ions from the bulk solution to the working electrode surface is slower than the faradaic reaction, the chloride ions will start to locally deplete[41]. The local depletion creates a chloride ion concentration gradient between the working and reference electrodes, represented by the blue curve in Figure 3.1a. The concentration gradient is derived from the migrative and diffusive terms of the Nernst–Planck equation[41, 42]. The derivation of the concentration gradient assumes the convective terms are negligible, as the system is in stagnant operating conditions. When the local chloride concentration is completely depleted at the surface of the working electrode, the ion flux to the surface will no longer be upheld, and the potential will rapidly increase to find a new faradaic process to fulfill the current[48, 90]. In chronopotentiometry, the potential response versus time (chronopotentiogram) is recorded while the current is applied, and the complete local chloride depletion at the surface is indicated as an inflection point in the chronopotentiogram[48]. The inflection point can be quickly identified by finding the maximum of the derivative of the chronopotentiogram. The corresponding time at the inflection point is known as the transition time (τ), and is defined by the Sand equation (Equation (3.2))[48, 90]:

$$\tau = \mathrm{D}\pi \left[\frac{\mathrm{FC^*}}{2j(1-\mathrm{t_{Cl^-}})}\right]^2, \quad (3.2)$$

$$t_{Cl^-} = \frac{|z_{Cl^-}|\lambda_{Cl^-}C^*_{Cl^-}}{\sum_k |z_k|\lambda_k C^*_k} \tag{3.3}$$

where F is Faraday's constant, D is the mean chloride ion diffusion coefficient, j is the current density, $C^*$is the bulk chloride concentration, and $t_{Cl^-}$is the transference number of chloride, or the fraction of chloride ions per total ions in solution. The chloride ion transference number can be calculated (Equation (3.3)) for chloride (Cl^-) and other ion species (k) present in the electrolyte, where z is the charge of the ion, λ is the limiting molar conductivity, and $C^*$is the bulk ion concentration. To calculate the transference number and diffusion coefficient, values for limited ion conductivities[91] at 25 °C and diffusion coefficients[64] at infinite dilution in water at 25 °C were used. In the presence of many ions that are not chloride (e.g., high conductivity of supporting electrolyte), t_{Cl^-} is negligible. The bulk chloride ion concentration directly relates to the transition time, and can be used as the chloride sensor signal[48].

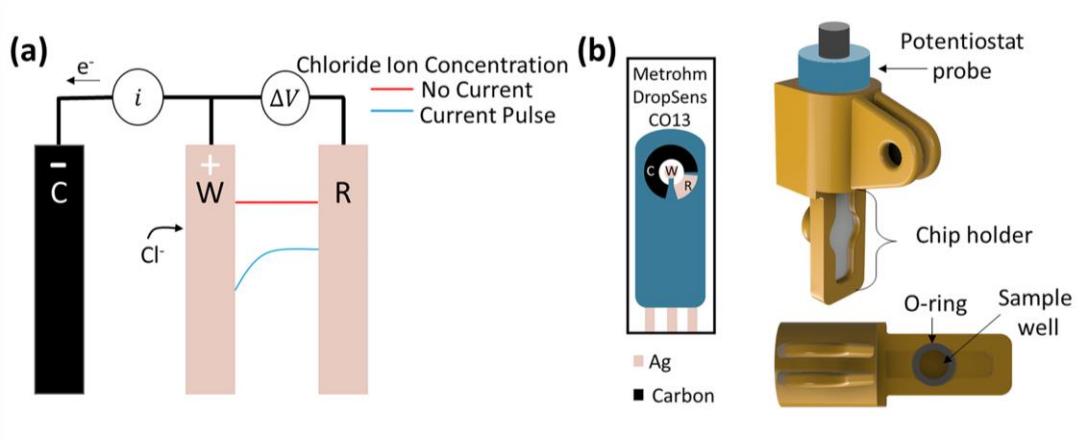


Figure 3.1:(a) Schematic of chronopotentiometric method. The local depletion creates a chloride ion con-centration gradient, shown by the blue curve, between the working and reference electrodes. (b) Schematic of DropSens C013 screen-printed electrodes and chip holder. The working electrode (W) and reference electrode (R) are silver, while the counter electrode (C) is made of carbon.

Resolution of the transition time at different chloride concentrations can be difficult to obtain at improper current densities. The current density directly relates to the rate of the reaction, and can influence how fast the silver chloride reaction is occurring. If a chloride

concentration is too large for a particular current density, the system cannot fully deplete the local chloride ions because the reaction rate is too slow. Alternatively, if a chloride concentration is too small for a particular current density, the reaction and transition time will occur too quickly. When the transition time occurs at time scales that are too short (τ <10 ms), a significant portion of the applied current goes towards charging the double layer, and thus inaccurately captures chloride depletion[48, 90]. At longer time scales (τ > 6 s), convective effects from ambient vibrations, or natural convection resulting from density gradients at the electrode surface, can no longer be ignored, and can influence the chloride ion concentration gradient[48, 90]. Thus, a chosen current density needs to resolve a variety of chloride concentrations within approximately 0.1 to 6 s, in order to accurately reflect the Sand equation (Equation (3.2)).

3.3 Materials and Methods

3.3.1 Chemicals and Test Solution Preparation

Sodium sulfate (Na_2SO_4, >99%), sodium chloride (NaCl, >98%), and citric acid ($C_6H_8O_7$, >99.5%) were purchased from Sigma-Aldrich (St. Louis, MO, USA). Sodium hydroxide (5 N NaOH) was purchased from EMD Millipore (Burlington, MA, USA). Customized artificial urine without chloride was purchased from Biochemazone (BZ104, Edmonton, AB, CA) at a pH of 6.3. The purchased artificial urine contained sodium citrate, sodium phosphate dibasic, magnesium sulphate hepta hydrate, sodium sulfate, potassium phosphate, uric acid, urea, acetic acid, and creatinine.

The simple solutions were made by creating a stock solution of 20 mM Na_2SO_4 with deionized water, and adding NaCl to adjust the chloride to a range of 5 to 250 mM, the relevant range present in urine. The simple solutions had a pH of 5.9, and conductivity varied with the

NaCl concentration in a relevant range of 0.4 to 3.5 S/m[92]. For pH experiments, the pH of simple solutions was adjusted with a 5% citric acid solution and 5 N sodium hydroxide solution, and sat overnight until the solutions were 4.7 and 7.7. The pH was measured with a pH meter (Thermofisher, Waltham, MA, USA). For conductivity experiments, the conductivity was adjusted by changing the Na_2SO_4 concentration (5–500 mM). The conductivity of the solutions was measured with a conductivity meter (Thermofisher, Waltham, MA, USA). For artificial urine samples, artificial urine was spiked with NaCl to simulate relevant chloride concentrations (50–150 mM).

3.3.2 Sensors and Experimental Setup

Chronopotentiometry was used to detect the chloride concentration in simple and artificial urine samples. To this end, screen printed electrodes, shown in Figure 3.1b, (DS-C013, Metrohm Dropsens, Oviedo, Spain) containing a silver working electrode, a carbon counter electrode, and a silver pseudo-reference electrode were used to perform all experiments. The working electrode had a 1.6 mm diameter, with an area of 2 mm^2.

The sensors were inserted into a custom 3D-printed chip holder with a 300 µL fluid well. The chip holder, shown in Figure 3.1a, was fabricated from biocompatiable dental SG resin (Formlabs, Sommerville, MA, USA) and treated with a ceramic hydrophobic chemical (NS 605, Nanoslic, Cincinnati, OH, USA) for better sealing. Solutions were pipetted into the fluid well, and an O-ring was placed in the holder to prevent solution leakage. The screen-printed electrodes were inserted into the chip holder and contacted the solution. The solutions were not stirred, and were preheated in the water bath prior to testing. The chip holder was submerged in a water bath to control temperature of the solutions during chronopotentiometry experiments. The electrodes were connected to a SP- 200 potentiostat (Biologic Science Instruments, Seyssinet-Pariset,

France). The working, counter, and reference electrodes were connected to the corresponding potentiostat terminals. The circuitry was manipulated using Biologic's EC-Lab software.

3.3.3 Measurement and Data Analysis

For single tests, one sensor was used per test at a single current density. The open circuit potential (OCP), where no current passes in the system, was recorded for 30 s. The OCP ensures that the solution reaches an equilibrium state prior to introducing a constant current. After OCP, the potentiostat applies a constant current between the working and counter electrodes for 15 s through a chronopotentiometry step. A large range of current densities (60–960 A/m^2) were tested. The current density was based on the area of the working electrode. For reusability tests, fresh 5 mL chloride solutions were tested with a reused sensor at room temperature. The reusability tests were run for 3 s, or until the 0.9 V cutoff was reached after a 30 s OCP.

For sweep tests, one sensor was used per test at multiple current densities. After an initial OCP step recorded for 60 s, a constant current density of 960 A/m^2 was applied between the working and counter electrodes, followed by 240 A/m^2, and lastly, 60 A/m^2. Each chronopotentiometry step was run for 3 s, with a 60 s OCP step run between to let the system relax back to equilibrium. A potential cutoff was imposed on the system, such that if a potential greater than 0.9 V was reached, the system would move to the next step. For both single and sweep tests, EC Lab recorded the potential of the working electrode relative to the reference electrode (E_W) as a function of time. A Python program determined the derivative of the potential with respect to time. To determine the transition time, the program found the maximum value of the potential derivative after an initial potential spike of 0.1 s. The corresponding time at this maximum was the transition time.

3.3.4 Electrode Surface Characterization

Sensors were submerged in 5 mL of chloride solutions to prevent the surface from being damaged from chip holder removal. The sensors were not washed prior to imaging, and may have had residual NaCl and Na_2SO_4 located on the surface. SEM images were captured with a Field Emission SEM (Hitachi SU8000 In-Line, Tokyo, Japan) in secondary electron detection mode. In addition to SEM, EDS (Bruker Quantax 200, Billerica, MA, USA) was used to elementally identify the surface of the working electrode. For both SEM and EDS, a 10 μA emission current and 10 kV acceleration voltage were used.

3.4 Results and Discussion

3.4.1 Detection of Chloride Ion Concentration Using Chronopotentiometry

We investigated chronopotentiometry to accurately detect chloride ion concentrations in aqueous solutions in near real-time. Figure 3.2a shows a representative chronopotentiogram of a 50 mM NaCl solution at a current density of 240 A/m^2. Initially, the potential difference (E_W) between the working and reference electrodes was close to zero. Upon applying a current density of 240 A/m^2, the potential rose rapidly, which corresponded to the ohmic drop across the electrolyte [48]. Next, the chloride ions began to deplete near the surface of the working electrode, and this process slowed the voltage rise. At 1.14 s, the local chloride became completely depleted, and the potential rapidly rose, creating an inflection point in the chronopotentiogram as the system switched to another faradaic reaction. By taking the derivative of the chronopotentiogram, the time to reach the inflection point could easily be identified as the transition time, indicated by the dotted blue line in Figure 3.2a. The transition time provides a

clear indication of chloride depletion, independent from an absolute potential value, and thus simple electrodes with a pseudo-reference can be employed.

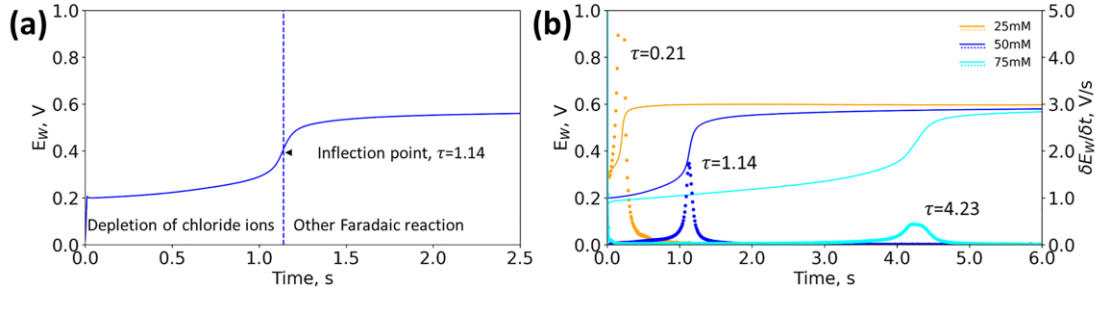


Figure 3.2:(a) Representative chronopotentiograms at 50 mM NaCl and 20 mM Na_2SO_4 at 25 °C in 240 A/m^2. (b) The effect of concentration on the potential response and transition time at 25 °C in 240 A/m^2. The dotted line represents the derivative of the chronopotentiogram.

The transition time is concentration dependent, and can be exploited as a sensor signal for quantifying urinary chloride. Figure 3.2b shows the relationship between chloride concentration and transition time at 240 A/m^2. As the concentration of sodium chloride increased from 25 to 75 mM, the transition time increased from 0.21 to 4.23 s, and the derivative peak decreased in signal intensity. The increase in transition time was a result of the presence of more chloride ions at the working electrode surface, requiring a longer time to deplete. If the transition time exceeded 15 s, the signal was unable to be resolved. When the chloride concentration became too high (>125 mM) or low (<25 mM) at 240 A/m^2, no inflection point was present in the chronopotentiogram, and the sensor could not detect the chloride concentration. The transition time does not occur because the slow rate of reaction was unable to fully deplete the chloride ions in samples of high chloride concentrations. Alternatively, at low chloride concentrations, the transition time occurred so quickly (e.g., <10ms) that it was unresolvable by our instrumentation.

3.4.2 Current Density Optimization for Detection of Biologically Relevant Chloride Concentration

The proper selection of current density is critical to optimize sensor performance at a specific chloride concentration across the biologically relevant range of urinary chloride concentrations. Here, we optically and electrically characterized the working electrode surface at 60, 240, and 960 A/m^2 across different time points in simple solutions of 50 mM NaCl, as shown in Figure 3.3. The EDS spectral data confirm the materials of a bare electrode and the presence of silver chloride in each SEM image shown in Figure 3.3, and are demonstrated in Figures 3.4 and Figure 3.5, respectively. It should be noted that the reference electrode was unaffected by the reactions occurring on the working electrode as shown in Figure 3.6. When the chloride ion depletion occurred at the slow rate of 60 A/m^2, as shown in Figure 3.3a–c, the faradaic reaction never fully depleted the local chloride ions, and no transition time at this chloride concentration was observed. The silver working electrode, shown in grey, continually had white silver chloride particles deposit on the surface as the reaction continued. At 240 A/m^2, as shown in Figure 3.3d–f, the current density was optimal for this chloride concentration, and the chronopotentiogram resolved the transition time at 1.1 s. Prior to the transition time, the working electrode surface looked similar to Figure 3.3a. After the transition time, larger silver chloride particles were visible, and likely formed between 0.5–1.1 s. As the current density further increased to 960 A/m^2, as shown in Figure 3.3g–i, local chloride ions quickly depleted, resulting in a rising potential, and the working electrode became damaged with cracks around the silver grain boundaries (Figure 3.3h). A potential cutoff that stopped the experiment when 0.9 V was reached prevented sensor damage, as shown in Figure 3.3g. By imposing the potential cutoff, unwanted reactions that affected the sensor's working electrode surface were eliminated.

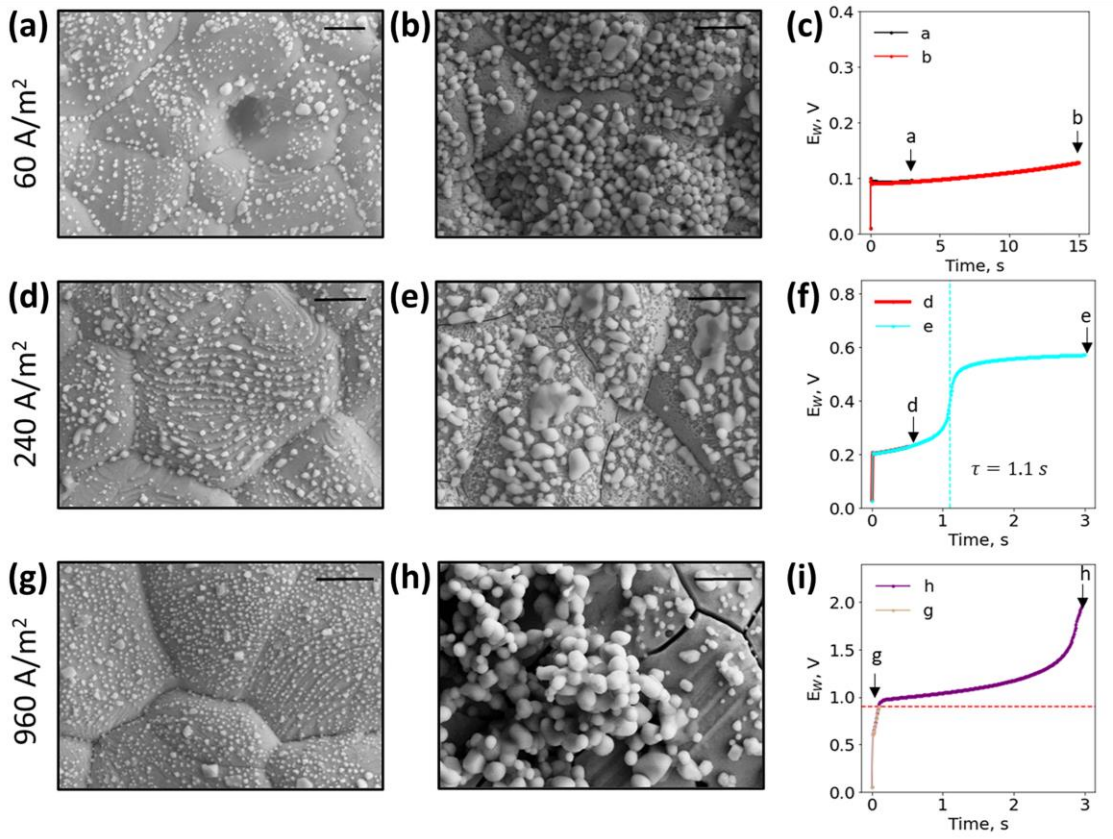


Figure 3.3:Scanning electron microscopy images of 50 mM NaCl and 20 mM Na_2SO_4 at 25 °C at (a) 60 A/m^2 after running for 3 s and (b) after 15 s; at 240 A/m^2 for (d) 0.5 s prior to transition time and (e) 3 s after transition time; at 960 A/m^2 with a (g) voltage cutoff of 0.9 V and (h) without a voltage cutoff running for 3 s. Each experiment was used with a fresh screen-printed electrode. The corresponding chronopotentiogram for the 60 A/m^2, 240 A/m^2, and 960 A/m^2 experiments are found in (c), (f), and (i), respectively. The potential cutoff is represented by a horizontal red line. The transition time is represented by a vertical cyan line. All scale bars are 2.5 µm

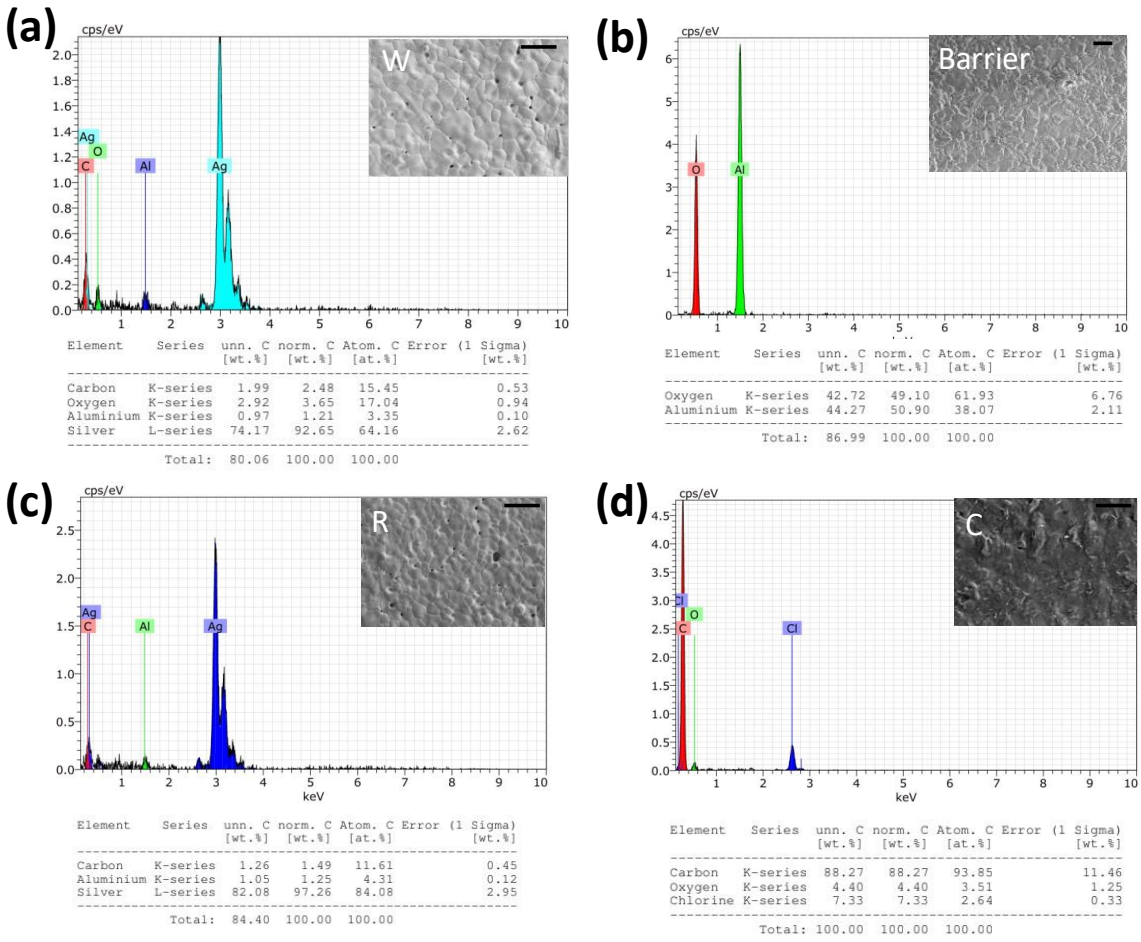


Figure 3.4:SEM/EDS of (a) the working electrode (b) the blue barrier film located around the electrodes (c) the reference electrode and (d) the counter electrode of a bare Dropsens C013 electrode. All scale bars are 25 µm.

By varying current density, we can resolve two orders of magnitude of chloride concentrations. If a particular chloride concentration could be resolved by a specific current density (60, 120, 240, 480, 960 A/m^2), the resulting average square root of transition time $\tau^{1/2}$ was plotted as a function of NaCl concentration (5–250 mM), and is shown in Figure 3.7. Specific chloride concentrations were able to be resolved with different current densities. For example, 50 mM NaCl could be resolved at 120, 240, and 480 A/m^2 at 2.03, 1.06, and 0.53 s$^{1/2}$, respectively. By increasing the current density, the transition time could be decreased by increasing the chloride depletion reaction. Although a single current density was unable to

resolve the entire range of biologically relevant chloride concentrations, we demonstrated optimal current densities for specific concentration ranges in near real-time (<15 s).

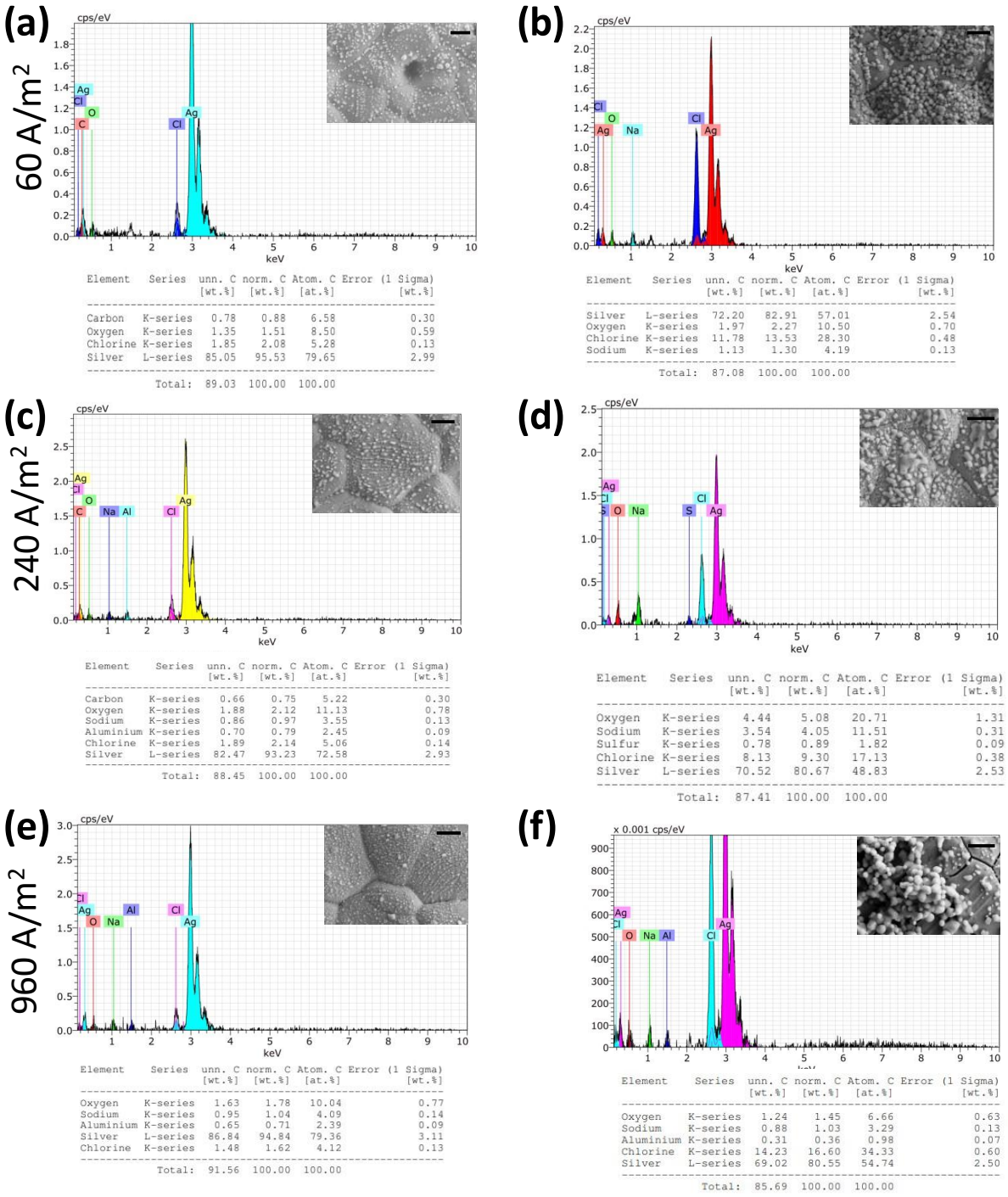


Figure 3.5:Corresponding EDS to SEM images shown in Figure 3.3 of 50 mM NaCl and 20 mM Na_2SO_4 at 25 °C at (a) 60 A/m² after running for 1s and (b) after 15s. At 240 A/m² for (c) 0.5s and (d) 3s. At 960 A/m² with a (e) voltage cutoff of 0.9V and (f) without a voltage cutoff running for 3 s. All scale bars 2.5 µm.

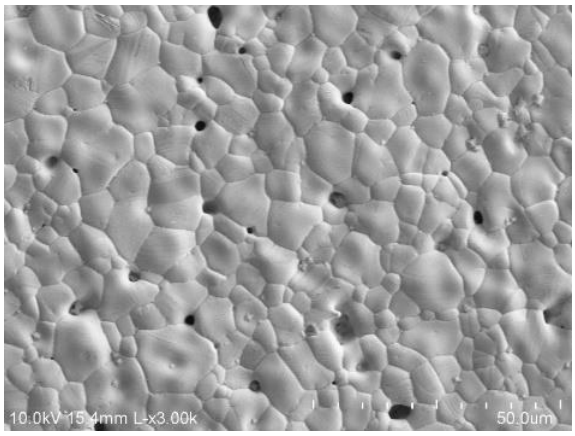


Figure 3.6:SEM image of the reference electrode after a solution of 50 mM NaCl and 20 mM Na_2SO_4 was tested at 25 °C with 960 A/m^2.

Furthermore, the Sand equation (Equation (3.2)) was able to accurately predict the sensor's response. The theoretical transition time was based on a chloride ion diffusion coefficient of 1.6×10^{-9} m^2/s, and the transference numbers were calculated using Equation (3.3) for each chloride ion concentration (5–250 mM NaCl) in the presence of 20 mM Na_2SO_4. The ion mobility (λ) used for Na^+, Cl^-, and SO_4^{2-}, were 5.01, 7.63, and 15.96 mS·m^2/mol, respectively[91] (refer to Theory section 3.2). Based on the mobility and chloride ion concentration, the transference number was calculated to be between 0.05 and 0.49. The theoretical square root of transition time, calculated from Equation (3.2), predicted the experimental values, and is shown for each current density curve as a black line in Figure 3.7. For short transitions ($\tau^{1/2} < 2$ s$^{1/2}$), the agreement between theory and experiments was quite good. At longer transition times ($\tau^{1/2} > 3$ s$^{1/2}$), there was a greater deviation from the predicted values, resulting from the influence of convection. Additionally, slight deviations could be attributed to an incorrect assumption of the area of the working electrode (e.g., surface roughness), deviation in chloride ion concentration due to measurement error, or inaccuracies in calculated mass transport parameters, as they reflected an ideal case. With promising theoretical

agreement, the entire range of biologically relevant chloride concentration can be resolved through the selection of optimal current densities.

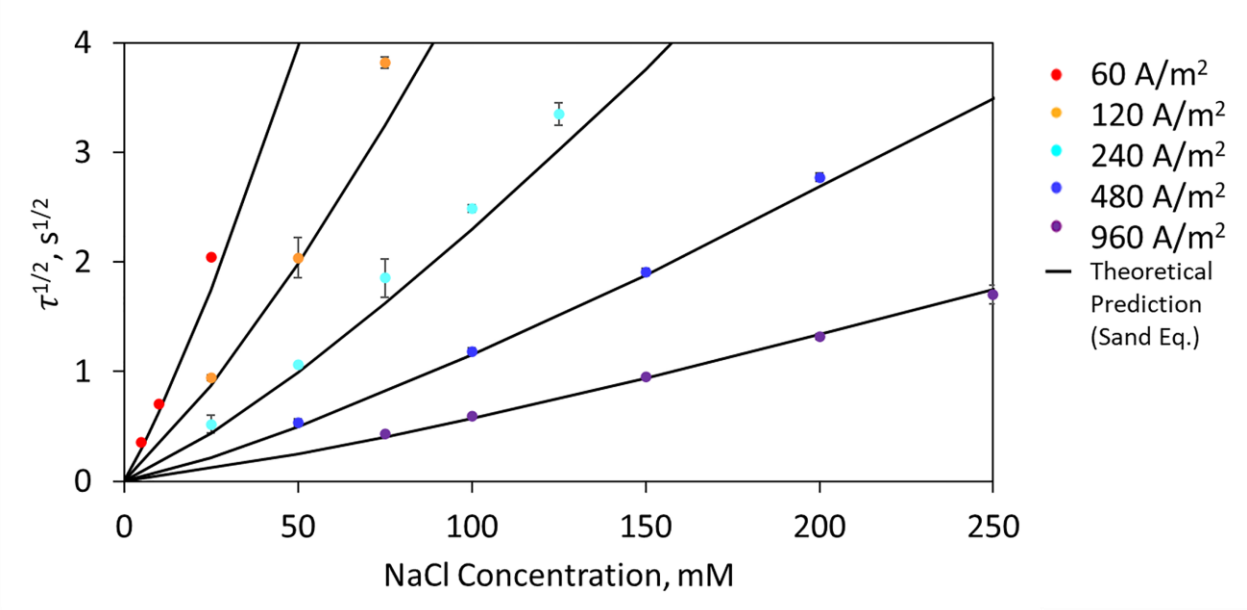


Figure 3.7:The experimental and theoretical (black line) square root of transition time (N = 3) as a function of chloride concentration in 20 mM Na_2SO_4 at 25 °C. One current density does not resolve the entire relevant concentration range of 5–250 mM NaCl.

3.4.3 Detection of Chloride Ion Concentration Using Swept Current Densities

To improve the detection range of a single sensor, a sweep algorithm was developed using multiple current densities on a single sensor, but limiting the potential to a predetermined potential cutoff value. The resulting chronopotentiograms of different chloride concentrations sensed with the sweep method are plotted in Figure 3.8. Each sweep cycle corresponds to a different resolvable chloride concentration range; the high (75–200 mM), mid (15–75 mM) and low ranges (5–15 mM) were resolved with 960, 240, and 60 A/m^2, respectively (note that the 250 mM NaCl concentration could be resolved if the experiment time was increased). To sweep current density while still maintaining the integrity of the sensor, the sensor had to be swept from high to low current densities. In this configuration, a high chloride concentration (<75 mM) either resolved immediately, or a low concentration quickly hit the potential cutoff, as seen in the

purple curve of Figure 3.8a–e. If swept from low to high current density, the sensor quickly became covered with silver chloride in the presence of a high chloride concentration, and the measurement became unreliable (as demonstrated from Figure 3.8 a–c). Ideally, the sensor would stop sweeping as soon as the transition time was detected, in order to prevent further change to the surface of the working electrode. The swept $\tau^{1/2}$ were in good agreement (2.6–7.3% difference) with the experimental $\tau^{1/2}$ found by the single current density method, and comparison tables can be found in Table 3.1 and Table 3.2. The proposed sweep method resolved the large range of relevant urinary chloride concentrations with a single sensor.

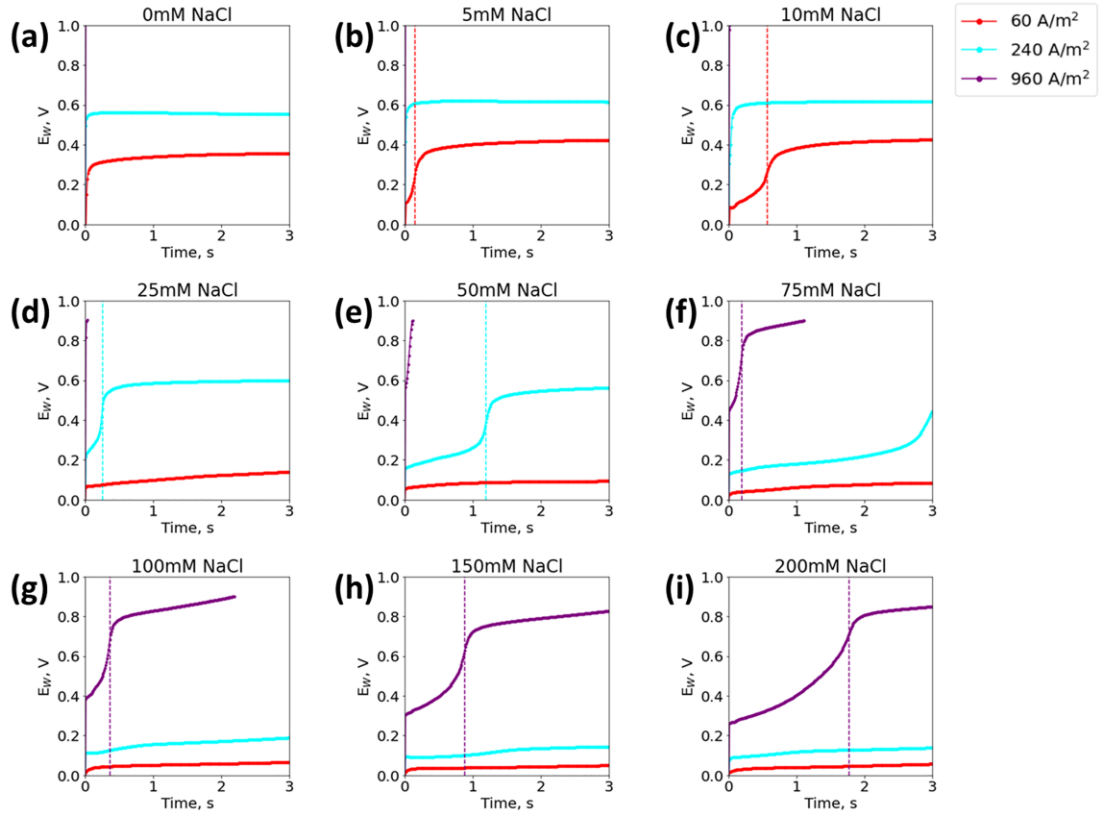


Figure 3.8:Chronopotentiogram of each mode of sweep test run in succession at 3 s for 960 A/m^2,480 A/m^2, and 60 A/m^2 in 20 mM Na_2SO_4 at 25 °C in NaCl concentrations of (a) 0 mM, (b) 5 mM, (c) 10 mM, (d) 25 mM, (e) 50 mM, (f) 75 mM, (g) 100 mM, (h) 150 mM, and (i) 200 mM. Vertical dotted lines in each plot indicate the transition time. Prior to each constant current density step, the system was run at OCP for 1 min.

Table 3.1:Comparison of the square root of transition time of tests conducted with an individual electrode versus tests completed with the sweep method in various NaCl concentrations (N=3) in 20 mM Na_2SO_4 at 25°C.

		Individual Electrode , $\tau^{\frac{1}{2}}$, $s^{\frac{1}{2}}$			Sweeped Electrode, $\tau^{\frac{1}{2}}$, $s^{\frac{1}{2}}$			
NaCl Concentration, mM	Conductivity S/m	960 A/m²	240 A/m²	60 A/m²	960 A/m²	240 A/m²	60 A/m²	% Difference
5	0.4	-	-	0.36	-	-	0.38	-7.3
10	0.5	-	-	0.70	-	-	0.73	-4.5
25	0.6	-	0.52	2.04	-	0.50	-	4.9
50	0.92	-	1.06	-	-	1.09	-	-2.6
75	1.1	0.44	1.85	-	0.44	-	-	0
100	1.4	0.60	2.49	-	0.60	-	-	0
150	2.0	0.95	-	-	0.95	-	-	0
200	2.5	1.32	-	-	1.32	-	-	0

Table 3.2:Comparison of the average measured chloride concentration, through back calculation in Sand equation, of tests conducted with an individual electrode versus tests completed with the sweep method in various NaCl concentrations (N=3) in 20 mM Na_2SO_4 at 25°C.

		Individual Electrode , $mM\ NaCl$			Sweeped Electrode, $mM\ NaCl$			
NaCl Concentration, mM	Conductivity S/m	960 A/m²	240 A/m²	60 A/m²	960 A/m²	240 A/m²	60 A/m²	% Difference
5	0.4	-	-	5.93	-	-	6.38	-7.3
10	0.5	-	-	11.21	-	-	11.73	-4.5
25	0.6	-	30.01	29.35	-	28.58	-	4.9
50	0.92	-	53.63	-	-	55.04	-	-2.6
75	1.1	80.74	85.80	-	80.74	-	-	0
100	1.4	103.68	2.49	-	103.68	-	-	0
150	2.0	152.33	-	-	152.33	-	-	0
200	2.5	195.86	-	-	195.86	-	-	0

Additional sensor response information can be used to improve the sweep algorithm for faster chloride quantification. As shown in Figure 3.9, the time to reach the potential cutoff is an important metric that can help determine how to enact the sweep algorithm. By incorporating the time to potential cutoff metric, 25 mM to 250 mM was identified using a single sweep step of 960 A/m^2. The signal was either determined with the time to potential cutoff (25–75 mM) or the transition time (75–250 mM). In cases where there were low chloride concentrations (<15 mM), the time to reach the potential cutoff was approximately 0.02 s to 0.03 s, and the sensor was

unable to distinguish between these different concentrations. In this case, the sensor would have two sweep steps (960 A/m^2, 60 A/m^2), thus resolving the low concentrations and reducing the total experimental sensing time from the present three-sweep configuration. Additionally, the potential of the sensor at early times within the experiment (e.g., 0.2 s) could be used as an indicator of chloride concentration, as the potential is a function of chloride concentration as demonstrated in Figure 3.10. However, absolute potential as an indicator should be treated with caution, as many parameters (e.g., conductivity) affect the potential of the sensor and could lead to inaccurate and unstable readings, as the sensor contains a pseudo-reference electrode. Using additional metrics, the sweep algorithm can be shortened to resolve the large range of relevant chloride concentrations in near real-time (3–66 s).

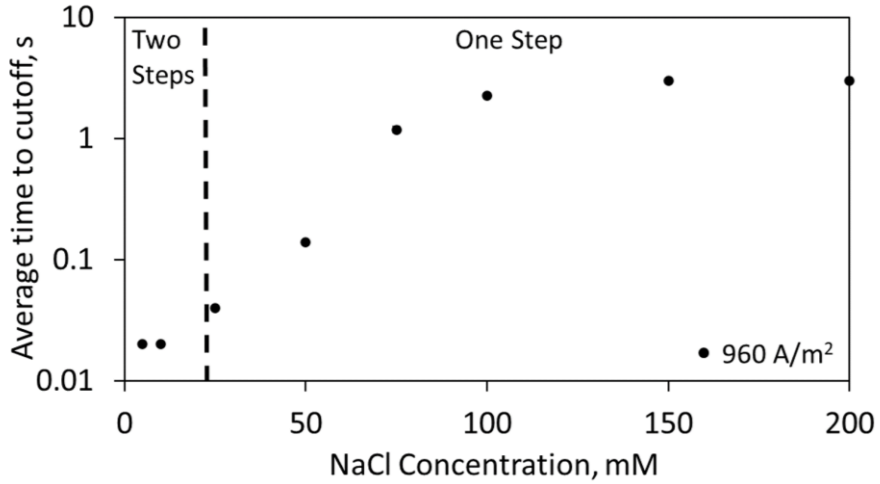


Figure 3.9:Average time to potential cutoff when run for 3 s at 960 A/m^2 in 20 mM Na_2SO_4 at 25 °C. Note that 150 and 200 mM NaCl never reached the cutoff. The sweep methodology only required 1 step to resolve 25 to 200 mM NaCl. Note that the time to potential cutoff was used as the signal for 25–75 mM, and the transition time was used to resolve 75–200 mM. For 5 to 15 mM, only two sweep steps were needed.

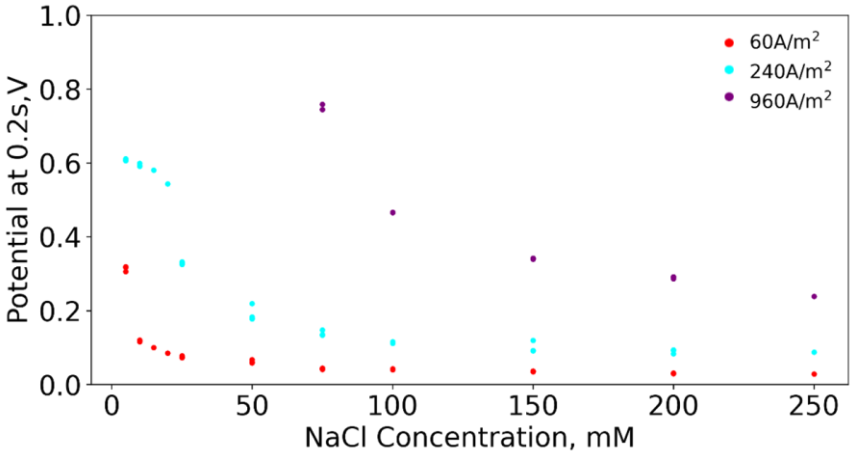


Figure 3.10:The potential value at 0.2 s during the sweep experiments for each current density step.

3.4.4 Sensor Reusability

To extend the lifetime of a single sensor, reusability was explored for cases where multiple measurements are needed. The same electrode in fresh sodium chloride solutions was tested for five experimental cycles. The experiments were conducted at different chloride concentrations at the optimal current density for each concentration (5 mM at 60 A/m^2, 50 mM at 240 A/m^2, and 100 mM at 960 A/m^2), and with the potential cutoff. Based on the resulting experimental transition times, the measured chloride concentrations were back calculated using Equations (2) and (3) and compared to the actual chloride concentrations (i.e., horizontal dashed line). The measured chloride concentration was plotted as a function of experimental cycles, as shown in Figure 3.11. For both 5 and 50 mM NaCl, the sensor was able to be reused across the five experimental cycles, with minimal deviation from the actual chloride concentrations. However, at the higher concentration of 100 mM NaCl, the sensor was only able to be used twice before significantly drifting from the actual chloride concentration values. Specifically, the measured chloride values at the first and third cycles were 99.9 mM and 87 mM, respectively. Thus, the chloride concentration at optimal current density affected the reusability of the sensor.

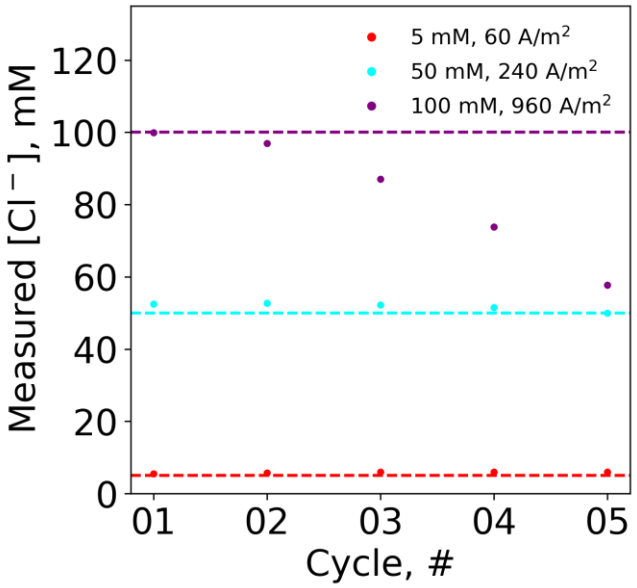


Figure 3.11:The measured chloride concentration, from back calculation using transition time, versus cycle number, using fresh 5 mL solutions with a reused sensor with 5 mM NaCl at 60 A/m^2, 50 mM NaCl at 240 A/m^2, and 100 mM at 960 A/m^2, in solutions of 20 mM Na_2SO_4 at room temperature, run for 3 s, or until the 0.9 V cutoff was reached.

The surface of the working electrode was further characterized using SEM and EDS to explore the impact of both chloride concentration and the current density on the reusability of the sensor. As shown in Figure 3.12, the SEM images depict the surface of the working electrode in both 50 mM and 100 mM NaCl solutions at the end of three consecutive chronopotentiometry cycles. The EDS results support the hypothesized formation of silver chloride, which can be found for each SEM image in Figure 3.13. In both cases, more silver chloride was formed on the working electrode surface after each cycle. At 50 mM, the surface of the working electrode was still exposed to the fresh sodium chloride solution after three cycles. In contrast, the 100 mM NaCl solutions had a working electrode surface that was covered with silver chloride after two cycles. The 100 mM NaCl solution at 960 A/m^2 had a different silver chloride morphology, with particles of larger surface area than the solution with 50 mM NaCl at 240 A/m^2. The silver chloride was likely blocking the active silver, or changing the surface properties of the electrode such that the transition time deviated from the predictions of the Sand equation (Equation (3.2)).

Thus, the sensor was reusable in cases of low chloride concentration (≤50 mM), where the silver chloride particle morphology had a smaller surface area. For future miniaturization of the sensor, many chloride sensors could be used in series to monitor a patient's inter/intraday urinary chloride concentration.

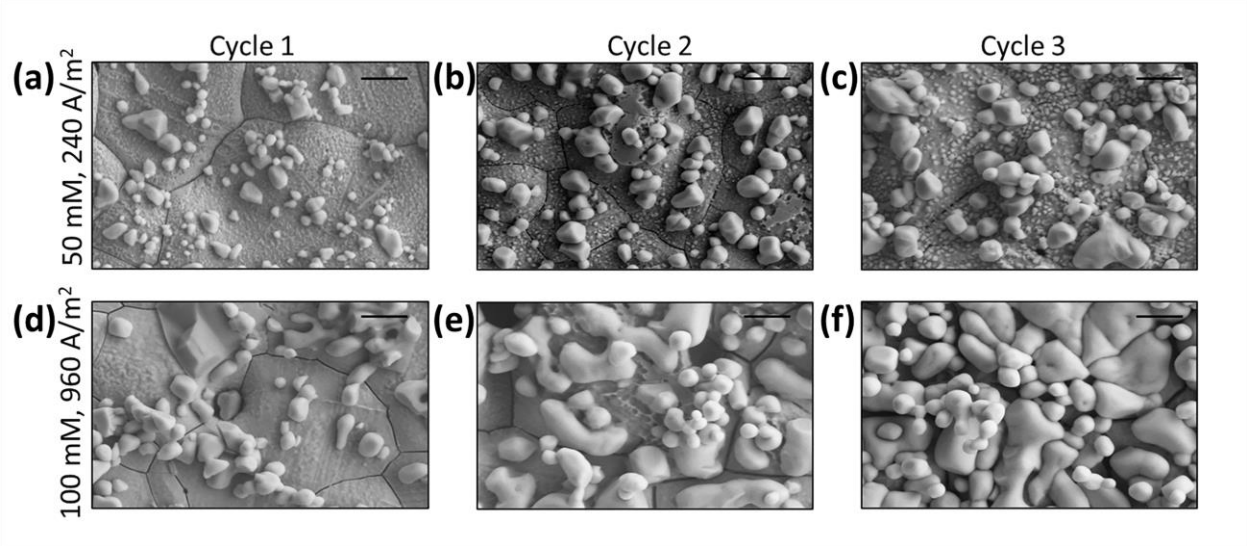


Figure 3.12:SEM images of sensors after running for (a) and (d) 1 cycle; (b) and (e) 2 cycles; and (c) and (f) 3 cycles, with experimental conditions of 50 mM NaCl, 240 A/m^2 and 100 mM NaCl, 960 A/m^2, respectively. Each cycle used 5 mL of fresh 20 mM Na_2SO_4 simple solution at 25 °C. A new electrode was used for each test, and was stopped after different cycle numbers. All scale bars are 2.5 µm.

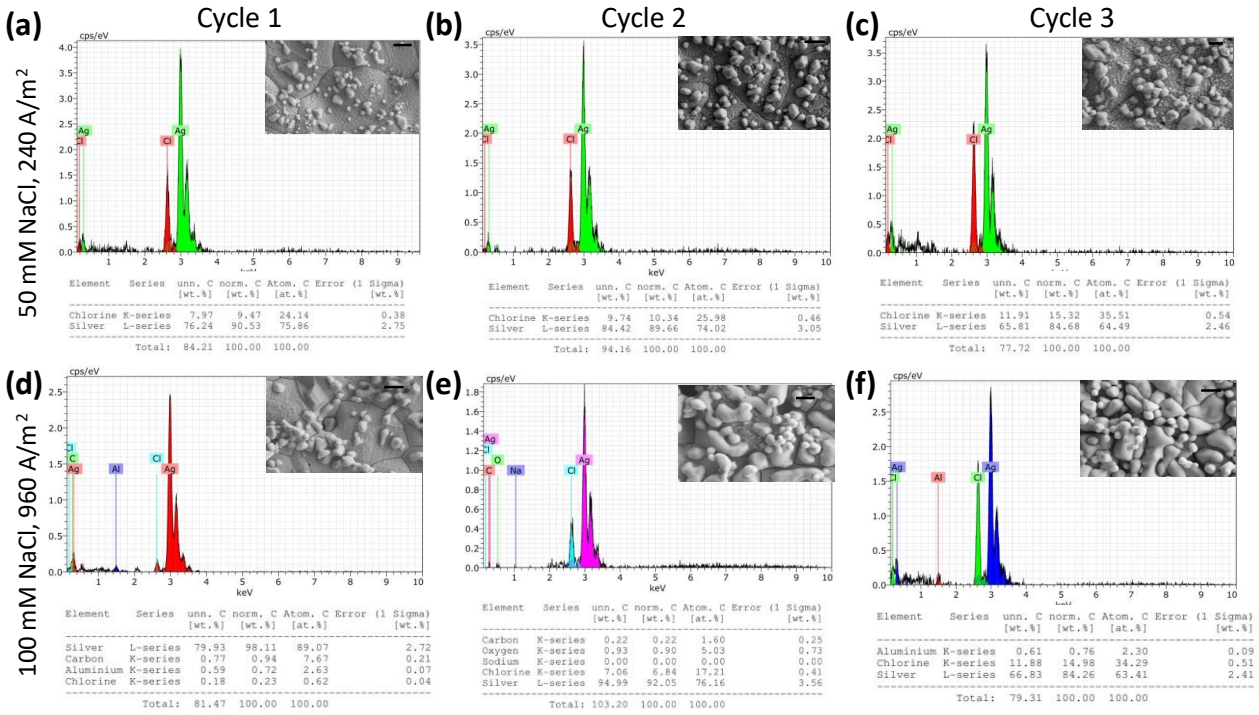


Figure 3.13:EDS corresponding to Figure 3.12 of sensors in 50 mM NaCl and 240 A/m^2 after running for (a) and (d) 1 cycle, (b) and (e) 2 cycles and (c) and (f) 3 cycles in 50 mM NaCl, 240 A/m^2 and 100 mM NaCl, 960 A/m^2 respectively. Each cycle used 5 mL of fresh 20 mM Na_2SO_4 simple solution at 25℃. A new electrode was used for each test and was stopped after different cycle numbers. All scale bars are 2.5 µm.

3.4.5 Effect of Relevant Clinical Parameters on Transition Time

The chloride sensor was evaluated in more complex solutions and was found to be relatively independent of pH and temperature. These solution parameters were evaluated in simple solutions of 100 mM NaCl at 480 A/m^2, and the results can be found in Figure 3.14a-b. To illustrate the impact of pH and temperature, the plot was fitted with a linear regression trendline, as shown in Figure 3.14a-b. It should be noted that 100 mM NaCl was chosen as a representative of normal urinary chloride and could be quickly resolved with the current density of 480 A/m^2. The relevant pH range of urine is 4 to 8, and the experimental $\tau^{1/2}$ did not significantly change as a function of pH, as hydrogen concentration does not influence the depletion of chloride ions near the working electrode. The solution temperature was considered for different temperatures (25, 31, 37 °C), and had minimal effect on $\tau^{1/2}$. Temperature affected

the diffusion coefficient, D, which increased 2–3% per degree[48]. The theoretical and average experimental $\tau^{1/2}$ had a 1.9–3.1% difference when the diffusion coefficient was adjusted by 3% per degree, which was a significant improvement over the 3.1–17.2% difference with no adjustment. To adjust for the changing diffusion coefficient, readily available temperature sensors[93] could be incorporated into the future design of the urinary chloride sensor.

Conductivity and transference number had a greater impact on the sensor transition time and should be considered in future chloride sensor design. In Figure 3.14c, the conductivity was adjusted by varying the Na_2SO_4 concentration (5–500 mM), and ranged from 1.1 –7 S/m. In these experiments, conductivity was indirectly proportional to the transference number (0.52–0.04), and the data were fitted with a second-order polynomial regression trendline. Higher conductivities increased the fraction of total ions in solution that were not chloride, thus decreasing the chloride ion transference number. At 500 mM Na_2SO_4 and 7 S/m, the transference number was negligible, and the percent difference between the experimental and theoretical $\tau^{1/2}$ was 0.2%. When the conductivity was decreased (1.1–3.4 S/m), there was a slightly higher percent difference (3–8%). To account for the effect of varying the transference number, conductivity sensors [94] could be incorporated into the design to enable calculation of transference number variations. Additionally, more non-chloride-containing salt solutions (e.g., Na_2SO_4) could be added to the urine sample prior to testing. Adding additional ions will increase the solution conductivity and decrease the fraction of chloride present in the total solution, making the transference number negligible. The elimination of the uncontrollable transference number in the Sand equation (Equation (3.2)) would simplify the sensor algorithm in complex solutions where the ions change over time (e.g., urine).

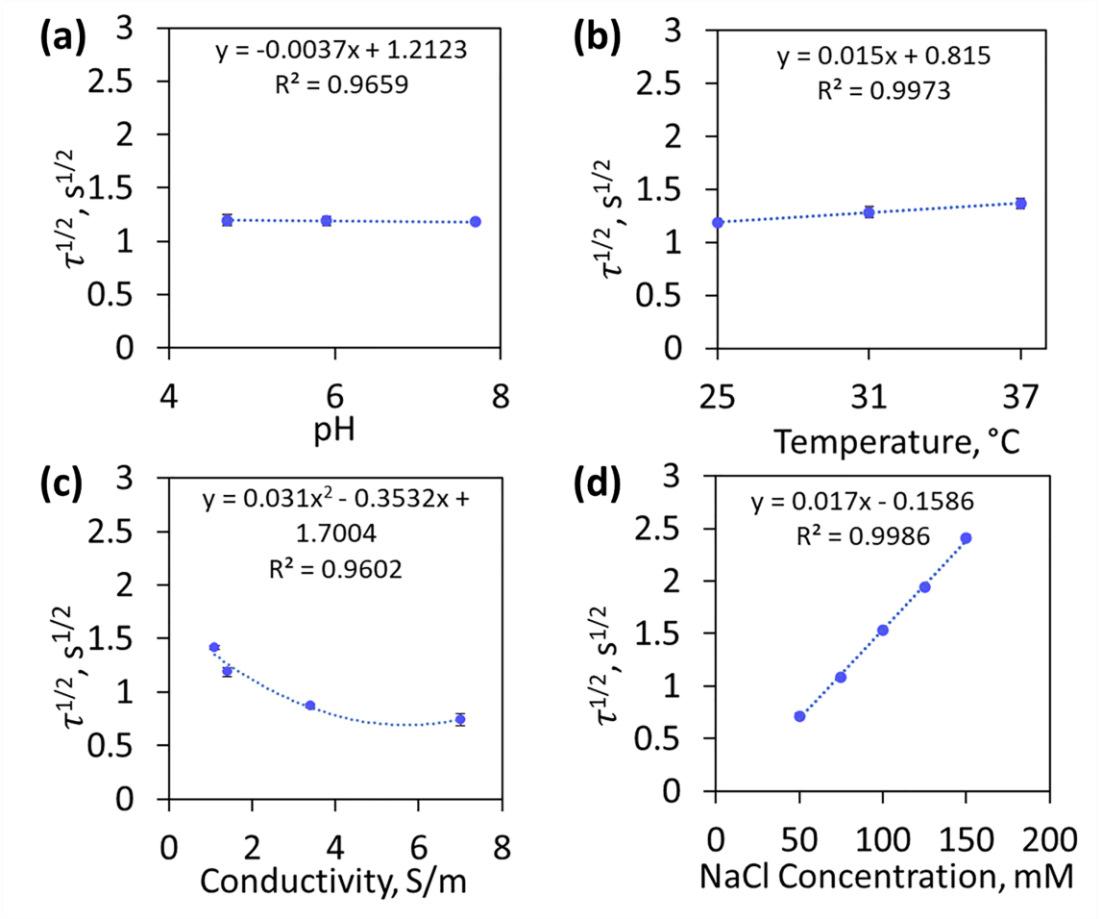


Figure 3.14:The effect of (a) pH at 20 mM Na_2SO_4 and 100 mM NaCl at 25°C; (b) temperature in 20 mM Na_2SO_4 and 100 mM NaCl; and (c) conductivity with varying Na_2SO_4 concentrations and 100 mM NaCl at 25 °C with respect to average squared root of transition time (N=3) in 480 A/m^2. The effect of other ions was investigated with (d) NaCl-spiked artificial urine as a function of the average square root of transition time (N=3) at 480 A/m^2 and 25 °C. Each curve was fit with a regression line (blue dotted line).

The chloride sensor was operated in the presence of other ions relevant to applications in urinary chloride. To investigate halide interference, we tested solutions that contained the clinically relevant concentration of sodium iodide[95]. As shown in Figure 3.15, sodium iodide had no effect on the sensor signal. The effect of other ions was evaluated by varying chloride concentrations (50–200 mM) in purchased artificial urine solutions, as shown in Figure 3.14d. The sensor was able to resolve 50 to 150 mM NaCl, but could not resolve 200 mM after 15 s of applied current. This deficiency was attributed to the conductivity difference of the simple and artificial solutions with 1.4 S/m and 1.2 S/m, respectively, in 100 mM NaCl. The lower

conductivity of the artificial urine sample increased the transition time, and agrees with the trend described in Figure 3.14c. The presence of other ions in the artificial urine did not affect the sensor's ability to resolve the transition time.

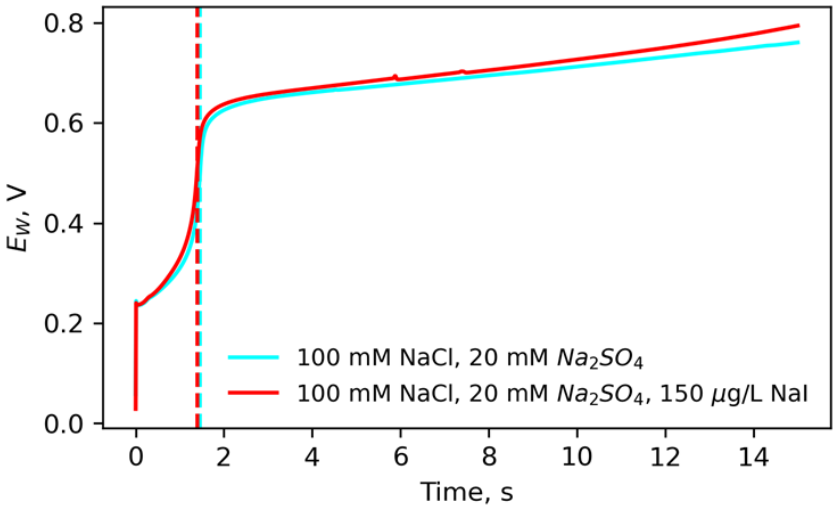


Figure 3.15:Chronopotentiogram of 100 mM NaCl, 20 mM Na_2SO_4 was tested at 25 °C with 480 A/m^2 with and without 150 µg/L NaI. The sodium iodide did not affect the signal. The dashed line represents the transition time for each curve.

3.5 Conclusion

The chloride sensor described in this research uses chronopotentiometry, combined with simple commercially available screen-printed electrodes, to resolve the entire range of relevant urinary chloride concentrations in near real-time, with no chemical modification or added reagents. The transition time serves as a reliable and clear indicator of bulk chloride concentration, and can be easily tuned by changing the applied current density. By optimizing the applied current density, the relevant chloride concentration range was resolved using a single sensor with a current density sweep algorithm, and the sensor lifetime was extended through reuse in cases of low chloride concentration (≤50 mM). The pH and temperature were shown to have a minimal impact on the sensor's response, with the conductivity and transference number having a greater influence. Chloride-spiked artificial urine was successfully quantified, and

demonstrates the sensor's feasibility for clinical applications. We believe this research can trigger additional research to further develop the sensor by investigating the effects of interfering species (e.g., halides, organics), and evaluating the feasibility in real urine samples. Sensor performance can be further improved by optimizing the sweep algorithm to further reduce detection time and account for sensor lifetime; furthermore, by incorporating additional sensors (i.e., conductivity, temperature) shifts in the transition time can be corrected. The sensor also has the capability of being integrated easily into an existing uroflowmeter to provide actionable data for critically ill patients in the ICU. The resulting simple, portable, user-friendly sensor provides a feasible path for achieving near real-time urinary chloride quantification in a variety of clinical settings.

Chapter 4 Electrochemical Sensing of Traumatic Brain Injury Biomarkers

This work was done in collaboration with Dr. Jouha Min. My contributions to this work include data collection, discussions with Dr. Jouha Min, and experimental data analysis.

4.1 Introduction

Traumatic brain injury (TBI) from a variety of accidents (e.g., vehicle collisions, falls) is prevalent and can become harmful if undiagnosed. Approximately 69 million people worldwide suffer from a TBI annually[22] with the majority being mild[96-98]. Repeated TBIs can lead to life altering physical and mental symptoms (e.g., headaches, memory loss, and physical imbalance)[99]. Currently, the primary diagnostic tools to indicate a TBI are qualitative tests and computerized tomography (CT) scans. To avoid not detecting a TBI, the majority of emergency patients (82% of 4.8 million patients annually) get a brain CT scan and 91% of scans reveal no brain injury[23]. Thus, most CT brain scans (>3.5 million) result in unnecessary exposure to ionizing medical radiation and financial harm[100-102]. An inexpensive diagnostic device capable of quickly identifying a TBI could generate actionable data without the use of harmful CT scans.

Protein biomarkers that release into the body following a TBI are a promising indicator and can be quantified in a rapid, noninvasive diagnostic system. Over the last decade, several biomarkers have been studied in blood and serum to identify a brain trauma, including glial fibrillary acidic protein (GFAP)[103], ubiquitin c-terminal hydrolase L1 (UCH-L1)[104], interleukin 6 (IL-6), interleukin 8 (IL-8), and neurofilament light chain (NF-L)[98]. Recently, the Food and Drug Administration (FDA) approved two of these biomarkers – GFAP and UCH-L1 for the

evaluation of traumatic brain injury[105]. After one hour of injury, GFAP and UCH-L1 levels elevate and can both be consistently detected in serum[106]. Thus, quantification of TBI biomarkers serves as a non-invasive, rapid method for identifying and monitoring the progression of a TBI.

Optical sensors[98, 107] are commonly used to accurately quantify TBI biomarkers. These sensors often employ sandwich immunoassays with fluorescent or colorimetric indicators (e.g., quantum dots, fluorophores) to label a particular biomarker. High throughput devices with low detection limits make optical detection a useful method of quantification. However, these sensors can become complex as they often require testing within a housing that shields any ambient light. Optical sensor performance also relies on a minimum path length and changes with sample volume[108]. Thus, optical sensors need expensive, and bulky optical systems (e.g, light sources, detectors, monochromators) which limit the portability of these sensors.

Electrochemical[8, 109, 110] sensors are a promising alternative method as they tend to have simpler analysis systems and are easily miniaturized. With the advent of microfabrication processes, developing micro-scale sensors is easily achieved. Many common electrochemical techniques include electrochemical impedance spectroscopy (EIS)[109, 111], amperometry[112], and field effect transistors (FET)[110]. Additionally, electrochemical methods have been shown to not be affected by sample volume and can be used with very low quantities (e.g, microliters to nanoliters)[108]. Thus, electrochemical methods are best employed in settings where portability is critical (e.g., military backpack, emergency vehicle).

Developing a miniaturized technology capable of sensitive, simple, and rapid detection of multiple biomarkers remains a challenge. To multiplex, electrochemical sensors often capture the biomarker of interest directly at the electrode or graphene surface. Microbead technology

coupled with electrochemiluminescence[8], and sensor arrays have been commonly employed[113]. Recently, an optical variable height microfluidic device has been developed for multiplexing TBI biomarkers[107, 114]. The optical device utilizes a variable height microfluidic channel to capture and separate beads of different sizes (e.g., 2.8 μm, 4.5 μm) along the length of the channel. Each bead size is capable of chemically capturing a different TBI biomarker. The development of this technology has created the opportunity to easily quantify multiple biomarkers but is limited by the large equipment needed for optical detection. By shifting to an electrochemical sensing platform with more portable instrumentation, the sensor can be further miniaturized and utilized in additional applications where smaller size is important.

Here, we report the development of an electrochemical enzymatic sandwich immunoassay for quantifying GFAP and UCH-L1 biomarkers. To begin, we utilize high throughput optical absorbance measurements to develop a robust assay protocol. Using optical detection, we investigate the effect of reagent concentration and incubation time on the assay signal and limit of detection. We then develop the assay protocols for electrochemical detection of GFAP and UCH-L1 and compare with the optical method. We identify the optimal average time interval in the amperometry curve to serve as a representative metric for standard calibration curves. Lastly, we propose an electrochemical device design and fabrication process capable of multiplexing TBI biomarkers.

4.2 Background

Enzyme-linked immunosorbent assays (ELISAs) facilitate capture and quantification of a particular biomarker through immobilization on a surface with antigen/antibody chemistry. Commonly employed ELISAs include direct[115], competitive[116, 117] and sandwich[8, 107]. In a direct ELISA, antigen proteins passively adsorb onto a plastic surface and enzyme conjugated detection

antibodies link to the antigen. Direct methods have the simplest chemistry with limited steps but are less specific and can have low signal. For improved signal, competitive assays have an inversely proportional signal to antigen concentration and are beneficial to use with small proteins. Sandwich assays demonstrate high sensitivity and specificity, but sourcing matched antibody pairs can be difficult[115]. As shown in Figure 4.1, a sandwich assay uses a capture antibody directly attached to a surface, such as a plastic substrate or paramagnetic beads, to capture the protein antigen. Then, to complete the antibody 'sandwich' an enzyme conjugated detection antibody binds to the other end of the protein antigen. Each assay type uses an enzyme to catalyze a reaction with a substrate to produce a quantifiable color change. Note, a quantum dot could replace the enzyme attached to the detection antibody for fluorescent optical detection.

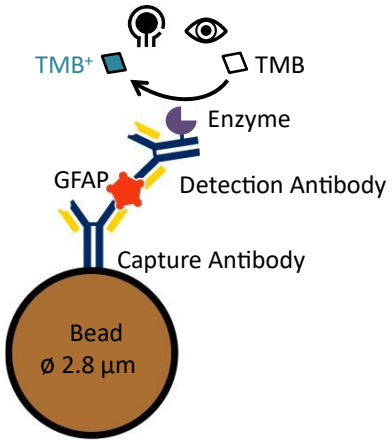


Figure 4.1:Schematic of an enzyme linked sandwich immunoassay. The enzyme immunoassay is capable of being both an optical and electrochemical detection method. Note, the depicted immunoassay is not to scale.

Enzymatic immunoassays can use both optical and electrochemical detection for quantifying TBI biomarkers in the presence of a substrate. The most common enzymes used are horseradish peroxidase (HRP) and alkaline phosphatase (AP). HRP tends to be smaller, more stable and cheaper than AP[118]. Combined with 3,3′,5,5′-tetramethylbenzidine (TMB) substrate and hydrogen peroxide, the HRP enzyme will catalyze a non-toxic reaction with a widely studied

mechanism shown in Figure 4.2[119-122]. The TMB oxidizes into a radical cation that is in rapid chemical equilibrium with a blue-green charge transfer complex consisting of a colorless diamine form and a yellow colored diimine (λ=370 nm, 652 nm). The HRP enzyme can facilitate an additional oxidation state producing a yellow diiamine (λ=450 nm). To quench the reaction for optical detection, sulfuric acid stop solution is added to reduce the pH of the solution and halt HRP redox activity while converting the TMB to the yellow diiamine[119]. The resulting color change makes the process highly favorable for optical detection and is easily measured with a plate reader (λ= 450 nm). For electrochemical detection, amperometry can be used to reduce the converted TMB^+ back into TMB using a three-electrode system consisting of a working, counter, and reference electrode. During the amperometry measurement, a 0.1 V potential is applied between the working and reference electrodes to facilitate the faradaic reduction reaction while current is simultaneously measured. The selected potential value has been shown to accurately convert a small amount of TMB^+ in the presence of large concentrations of TMB[123]. The strength of the signal is directly proportional to the concentration of antigen biomarker.

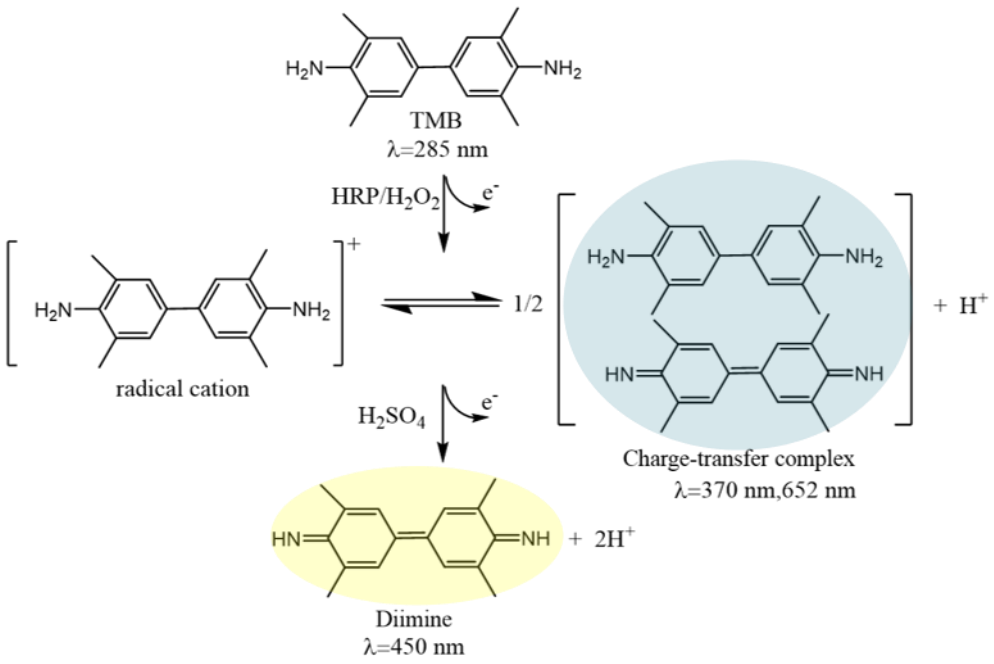


Figure 4.2:Schematic of the TMB reaction in the presence of HRP enzyme and hydrogen peroxide.

4.3 Materials and Methods

4.3.1 Antibody Conjugation to Magnetic Beads

Phosphate buffer saline, (PBS), 1% Bovine Serum Albumin (BSA), ammonium sulfate, Bicinchoninic acid kit (BCA, Pierce™ Rapid Gold), Tween 20, and sulfuric acid were purchased from Fisher Scientific (Hampton, NH, USA). Two and a half milligrams of superparamagnetic beads coated with epoxy groups (Dynabeads™ M-270 Epoxy, Invitrogen™,Waltham, MA, USA) were suspended in 1 mL of PBS. The beads were mixed and incubated with tilting rotation for 10 minutes using a mixer (HulaMixer, ThermoFisher Scientific, Waltham, MA, USA). The bead solution was placed on a magnet to remove the supernatant and washed in 1 mL PBS. The capture antibody and detection antibody pairs (DuoSet™, R&D Systems, Minneapolis, MN, USA), were selected for the biomarker of interest. The bead to capture antibody ratio was [2.5 mg beads: 50 µL capture antibody]. For the coupling reaction, the beads were resuspended in 50 µL of PBS, 50 µL of 1 mg/mL capture antibody and 50 µL of 3 M ammonium sulfate solution.

The antibody coupling concentration was satisfactory with approximately 1.19 $\times 10^9$ beads/mL and a capture antibody concentration of 333 µg/mL. The bead solution was incubated for 2 hours at room temperature with slow tilt rotation and then moved to 4°C for at least 16 hours with slow rotation. Following incubation, the bead supernatant was removed and stored for use in the BCA assay. The beads were washed four times with 0.5 mL of PBS and resuspended in 82.5 µL PBS with 1% BSA. The final bead concentration was approximately 2×10^9 beads/mL.

4.3.2 Bicinchoninic acid Assay

To determine successful bead conjugation, a bicinchoninic (BCA) assay was performed. The BCA assay uses a copper-chelating reaction to colorimetrically quantify protein concentration. Briefly, biomarker specific capture antibodies were diluted three-fold from 1 mg/mL to produce antibody standards. Following the manufacturers protocol, 20 µL of sample and 200 µL working reagent (20 parts Reagent A proprietary copper chelator: 1 part Reagent B cupric sulfate) were added to a 96 well plate. The samples consisted of the antibody standards, the reserved bead supernatant, and reacted bead supernatant. For the reacted bead solution, 2 µL of conjugated beads diluted in 18 µL PBS were reacted with the 200 µL working reagent in a separate vial. The beads were magnetically removed from the solution prior to testing. The plate was mixed and incubated at room temperature for 5 minutes. The light absorbance (λ = 480 nm) was measured with a plate reader (Biotek Synergy H1, Agilent Technologies, Santa Clara, CA, USA).

4.3.3 GFAP and UCH-L1 Sandwich Immunoassay

As shown in Figure 4.3, for the bead-based sandwich immunoassay, 5 µL capture antibody conjugated bead solution and 150 µL protein biomarker (e.g., GFAP, UCH-L1) was mixed and

incubated for 2 hours with rotation in Incubation I. The beads were washed three times with a wash buffer (0.05% Tween 20 in PBS). Then, 50 µL of biotinylated detection antibody (100 ng/mL GFAP detection antibody; 1000 ng/mL UCH-L1 detection antibody) were introduced to the beads and incubated for 2 hours with rotation in Incubation II. The beads were washed three times with wash buffer. Next, 50 µL of Streptavidin conjugated horseradish peroxidase (HRP) enzyme (Thermofisher Scientific, Waltham, MA, USA, 1:625 dilution in PBS) was introduced and incubated for 20 minutes with rotation in Incubation III. The beads were washed four times with wash buffer and resuspended in 15 µL of PBS. The resuspended beads were used for both optical and electrochemical testing. For optical testing, 100 µL of 3,3', 5,5-tetramethylbenzidine (TMB, One Step Ultra, Thermofisher Scientific, Waltham, MA, USA) was mixed with 2.5 µL of bead solution and reacted for 6 minutes in Incubation IV. Following the reaction, 50 µL of 0.16 M sulfuric acid stop solution was added to the vial. The bead supernatant was transferred to a 96 well plate and the light absorbance (λ = 450 nm) was measured with a plate reader.

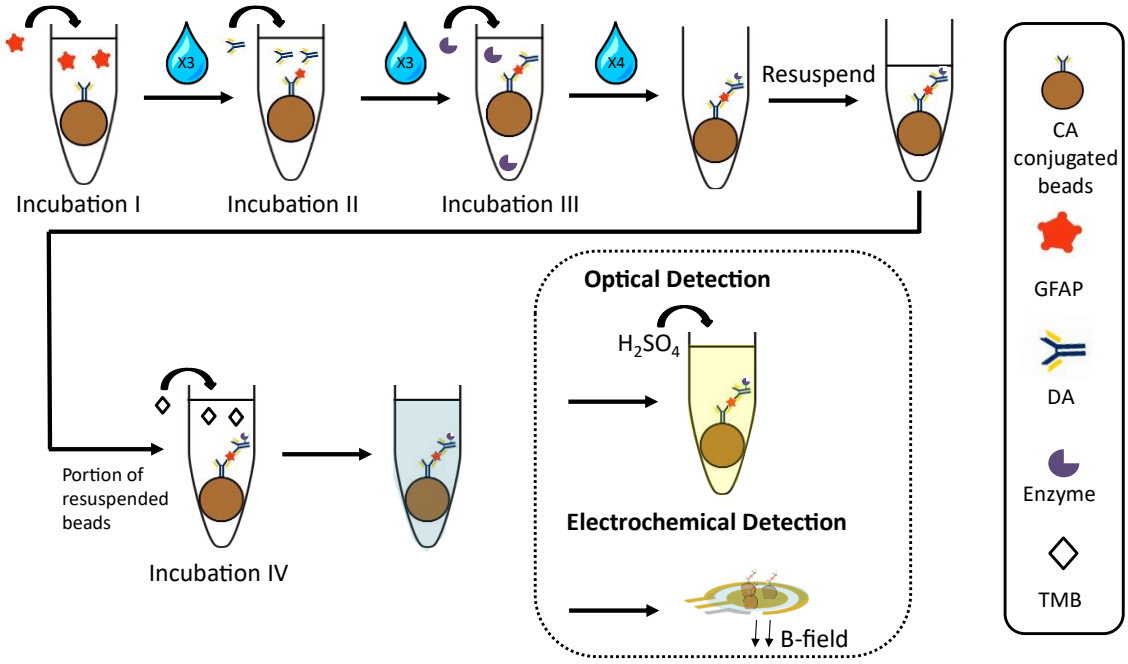


Figure 4.3:Schematic of the assay steps necessary to detect the biomarker of interest (GFAP depicted) with optical and electrochemical detection. Each step was completed in a microcentrifuge tube with 2.8 µm diameter beads. Note, a single bead is depicted as a representative for millions of beads that were present during the assay.

4.3.4 Electrochemical Assay, Testing and Analysis

Amperometry was used to initiate the TMB reduction reaction that generates the electrochemical signal. To this end, screen printed electrodes (220AT, Metrohm Dropsens, Oviedo, Spain) were used to perform the electrochemical experiments. The electrodes were on a ceramic substrate. The reference electrode was silver, and the working and counter electrodes were gold. The sensors were inserted into a custom 3D printed holder. The holder contained a magnet that aligned with the center of the working electrode and the electrodes were connected to a SP-200 potentiostat (Biologic Science Instruments, Seyssinet-Pariset, France). The electrodes were controlled with Biologic's EC-Lab software.

To oxidize TMB in the presence of the HRP enzyme, 5 µL of reserved bead solution and 20 µL of TMB were pipetted into a vial to react for 6 minutes. The contents of the vial were pipetted on top of the working electrode, where the beads were attracted to the surface of the

working electrode with the magnet located under the screen-printed electrodes. The open circuit potential (OCP), where no current passes in the system, was measured for 30 s to ensure proper electrode connection. Next, the TMB^+ was reduced to TMB by applying 0.1 V between the working and reference electrodes for 1 minute. For amperometry tests, EC Lab recorded the current between the working and counter electrode during the application of constant potential. A Python program determined a current average of the measurement.

4.4 Results and Discussion

To begin, we utilized optical assays to develop a protocol suitable for translation to electrochemical detection. We conducted a limited investigation to study how small perturbations to different assay variables affected the overall measurement. During these experiments, we often evaluated the assay across a wide range of concentrations. We were able to achieve a working electrochemical protocol, but the assay parameters will need to be optimized for on chip detection in future studies. Ideally, the assay would capture concentration ranges of 30 – 10,000 pg/mL and 200 – 3,200 pg/mL of GFAP and UCH-L1, respectively[124, 125]. Additionally, the eventual goal for optimized assay time would be complete all the assay steps after bead conjugation in under 15 minutes to quickly quantify a traumatic brain injury event and monitor response to treatment.

4.4.1 The Effect of Reagent Concentration on Assay Signal

To quickly develop the assay, optical detection was utilized for high throughput analysis of varying reagent concentration, such as capture antibody, on the assay performance. To study the effect of capture antibody concentration, 100 μg and 50 μg capture antibody were added to 2.5 mg beads. The resulting standard curves, shown in Figure 4.4, indicate that there was minor

difference in signal between the different amounts of capture antibody. Assuming 30% conjugation efficiency, 6.0×10^{13} and 1.2×10^{14} molecules of capture antibody would be present on the beads for 100 µg and 50 µg capture antibody (150 kDa), respectively. At the upper limit of GFAP protein (50 kDa) concentration of 10,000 pg/mL, there are approximately 1.8×10^{10} molecules per assay. Therefore, both concentrations have an excess of capture antibody molecules attached to the beads. Too much antibody coating the surface of the beads could lead to non-specific binding and steric hindrance that could prevent the GFAP protein from linking to the bead. Additionally, the 50 µg capture antibody had a lower limit of detection (LOD), calculated by taking the average of the blank plus three times the standard deviation of the blank. The resulting LOD was backcalculated using regression equations derived from plotting absorbance signal with respect to GFAP concentration.

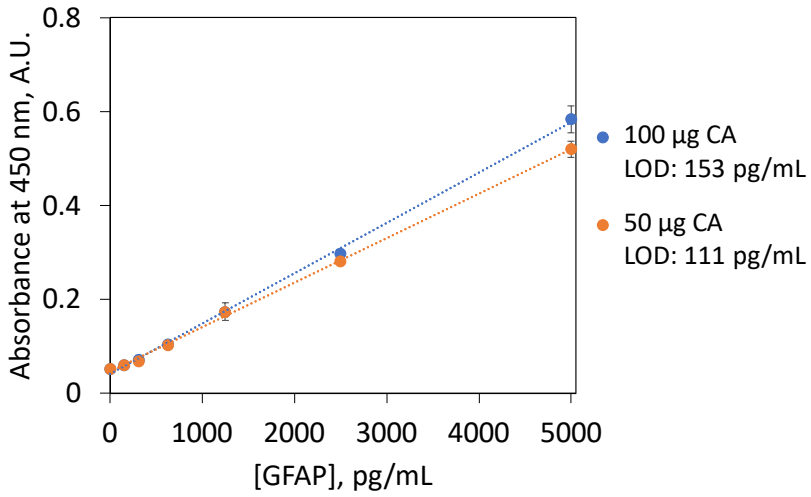


Figure 4.4:Absorbance measurements (λ = 450 nm) for varying capture antibody concentrations (N=3) with Incubation I – IV times of 2 hour, 2 hour, 20 minute and 6 minutes, respectively.

We also varied the concentration of the detection antibody to determine the effect on assay signal. As shown in Figure 4.5, the detection antibody concentration was varied at fixed GFAP protein concentration (0 and 313 pg/mL) for different TMB reaction times (Incubation IV). With a 3 minute incubation, each detection antibody concentration demonstrated a similar

weak optical signal (< 0.1 A.U.). By increasing the time to 20 minutes, as shown in Figure 4.5b, higher absorbance signals were observed across all detection antibody concentrations with larger signals observed with more detection antibody. However, an increased signal was also observed in the control, likely resulting from non-specific binding occurring from excess detection antibody present in the sample. To better understand the relationship between the signal and noise, the signal to noise ratio (SNR) was calculated for each detection antibody concentration and is depicted in Figure 4.5c. The SNR was calculated as the absorbance signal divided by three times the standard deviation of the blank. The highest SNR observed was with the 1 µg/mL detection antibody concentration and 20 minute incubation. The SNR was similar between all other combinations, except for 0.1 µg/mL with 3 minute incubation which was lower. The overall assay expense could be limited by using reduced detection antibody concentrations.

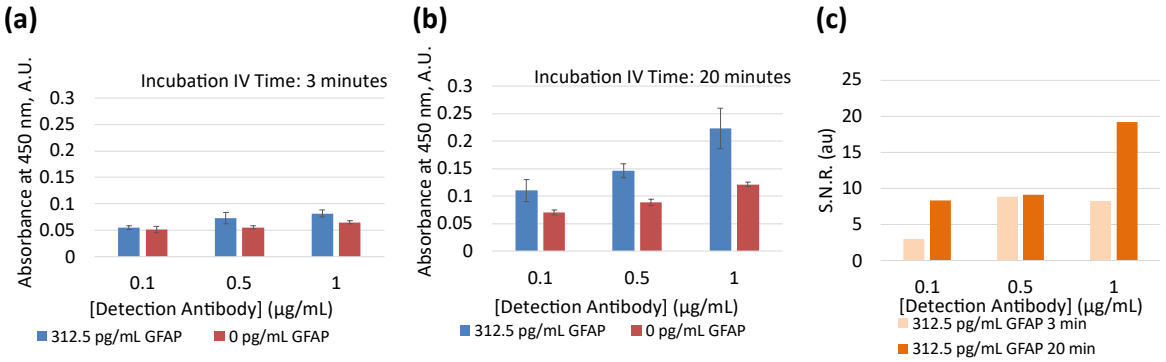


Figure 4.5:Absorbance measurements (λ = 450 nm) for varying GFAP detection antibody concentrations with fixed GFAP protein concentration and control (N=4) after (a) 3 minute and (b) 20 minute Incubation IV times with (c) the corresponding signal to noise ratio. Incubation I – III times were 2 hour, 2 hour, and 20 minute, respectively.

4.4.2 The Effect of Time on Assay Performance

The incubation times of each assay step (e.g., Incubation I, II, III, IV in Figure 4.3) were investigated with the protocols developed from the manufacturer and Min *et al*[112]. The manufacturer incubation time protocol (e.g., 2 hour, 2 hour, 20 min, 20 min) was based on times recommended for ELISAs where capture antibodies are attached to plastic well plates. A

comparison of the optical absorbance signal produced from these two protocols can be found with respect to GFAP concentration in Figure 4.6. By increasing incubation time, both lower limits of detection and increased optical absorbance can be achieved. The longer manufacturer recommended assay had a lower detection limit by a factor of 42.9 compared to the short form assay. Further optimization of incubation time is needed to minimize the total assay time while maintaining low limits of detection.

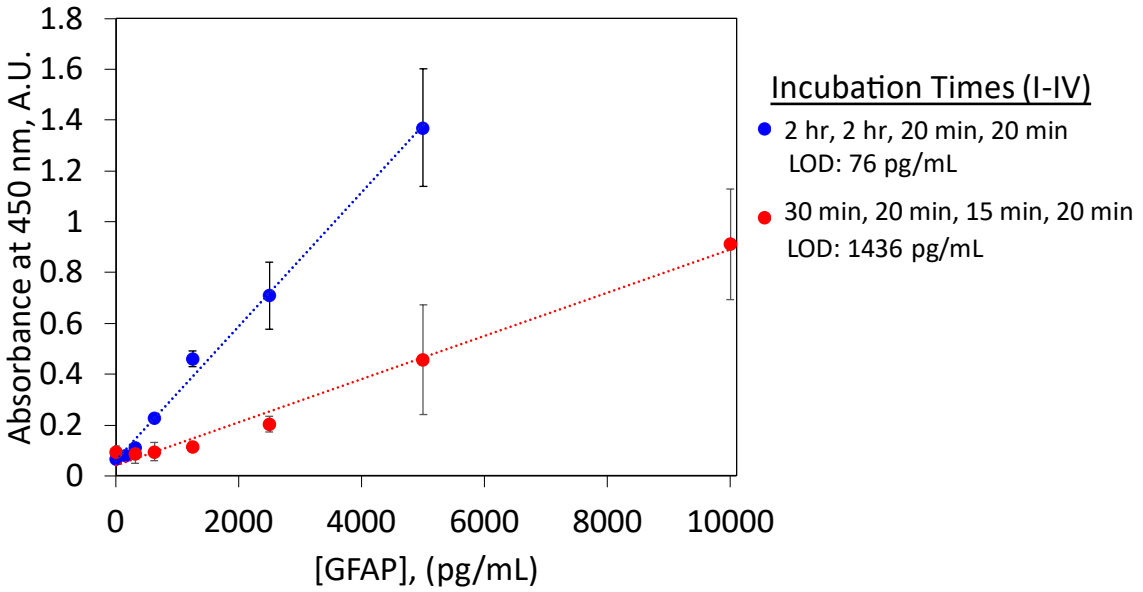


Figure 4.6:Standard calibration curve of GFAP (N=3) with absorbance measurements (λ = 450 nm) with varying Incubation I-IV times.

To reduce the overall assay time, TMB oxidation time (Incubation IV), was varied in Figure 4.7. Note the Min *et al.* incubation times were used resulting in a higher observed limit of detection. By increasing the time that the TMB and HRP enzyme react, more TMB is converted to TMB^+. The resulting increase in TMB^+ creates a larger optical absorbance signal and improved LOD. At a TMB reaction time of 3 minutes, a small signal was observed with a large limit of detection. However, at a longer reaction time scale of 20 minutes more error was observed, especially at higher concentrations of GFAP (≥ 5,000 pg/mL). We found that by

reducing the time to 6 minutes, a large signal is achieved with a reduced reaction time span from 20 minutes.

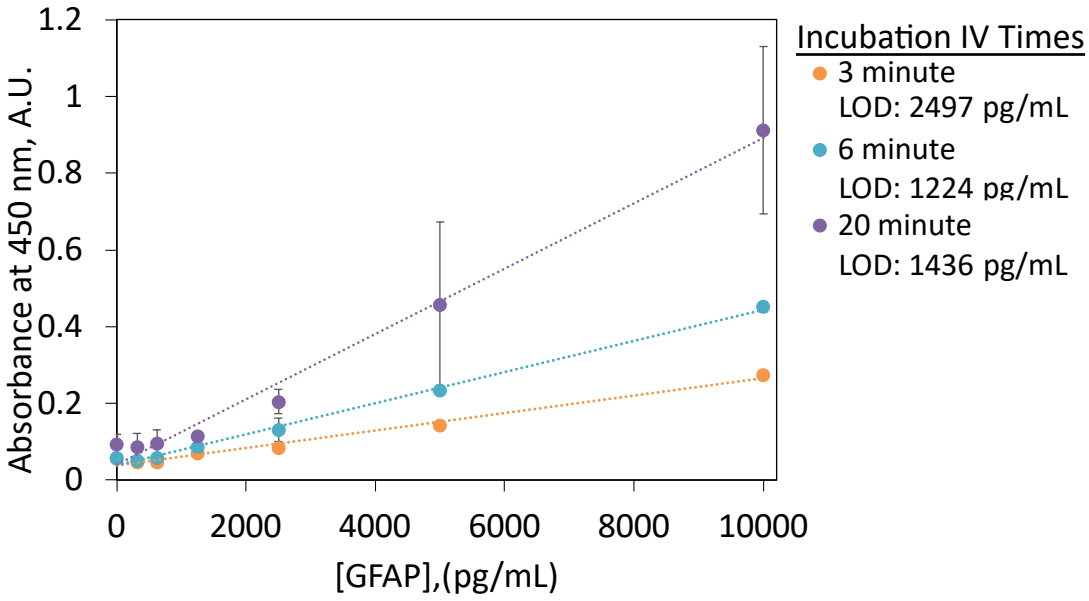


Figure 4.7:Standard calibration curve with absorbance measurements (λ = 450 nm) for varying Incubation IV times (3 minute; N=1; 6 and 20 minute N=2). Incubations I, II and III were 30 minutes, 20 minutes and 15 minutes, respectively.

The time of the initial incubation between capture antibody and protein (Incubation I), was studied to further reduce the overall assay time. A standard GFAP calibration curve for varying Incubation I times is shown in Figure 4.8. Both curves achieve close optical signal strength, indicating similar conversion of TMB^{+} for each curve. However, the 2 hour incubation time had less error between trials, resulting in a LOD ~10 times smaller than the 1 hour incubation time. This could be because of operator error or improved capture of GFAP protein with longer incubation time. The presented results indicate that the assay time can be significantly shortened while still maintaining satisfactory performance. However, further investigation is needed to achieve optimal assay time for each incubation step, both in a vial and within a flowing channel.

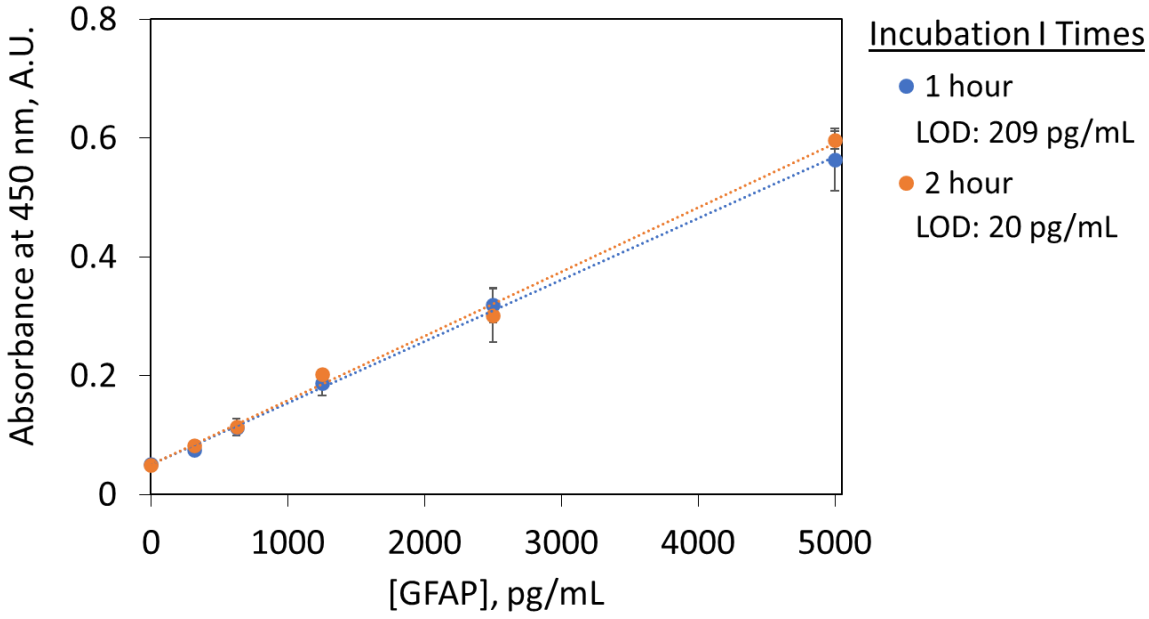


Figure 4.8:Standard calibration curve with absorbance measurements (λ = 450 nm) for varying Incubation I times (N=3; N=6 for 0). Incubations II, III and IV were 2 hours, 20 minutes and 6 minutes, respectively.

4.4.3 Electrochemical Detection of TBI Biomarkers

We have investigated amperometry for accurate quantification of TBI biomarker concentration. Figure 4.9a depicts the electrochemical cell consisting of gold working and counter electrodes with a silver reference electrode. When the TBI biomarker is present, the HRP enzyme links to the detection antibody and catalyzes the oxidation of the TMB substrate into TMB^+. By employing the amperometry method through application of potential between working and reference electrodes, the TMB^+ present in the solution surrounding the beads is reduced to TMB. Each amperometry curve, as shown in Figure 4.9b, begins with a large current value that decays exponentially towards steady state. A large initial and steady state current value corresponds to a higher concentration of oxidized TMB^+. Thus, the concentration of TMB^+ and the resulting current value relates directly to the amount of TBI biomarker and can be exploited in development of an electrochemical sensor.

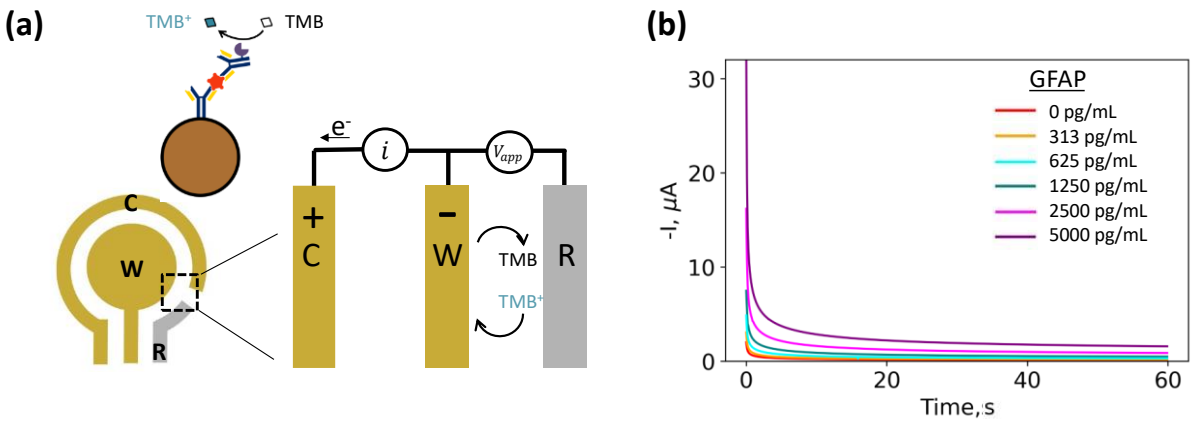


Figure 4.9:(a) The electrodes consist of gold working (WE), counter (CE), and silver reference (RE) used to electrochemically detect biomarker concentration. The HRP enzyme in the presence of H_2O_2 converts the TMB substrate into TMB^+ which is reduced back into TMB with the electrodes. (b) The generated representative reductive current between the working and counter electrodes serves as an indicator of amount of TMB^+ converted and corresponds to the GFAP concentration. The amperometry measurement was conducted with 5 µm beads reacted with 20 µL TMB for 6 minutes at varying GFAP concentrations.

The resulting amperometry signal was analyzed to determine the optimum metric used for electrochemical sensing. As shown in Figure 4.10, different time intervals of the resulting current signal were averaged and plotted with respect to GFAP concentration. When averaging the beginning interval prior to the decay at 0 to 2.5s, a large current signal is achieved, but there is larger deviation between different trials and the limit of detection is slightly higher. Also, in this range, charging current is likely to affect the measurement at short time scales. The optimal interval is averaging between 2.5 and 5s, after the initial current spike. At this interval, there is still a high current signal achieved with the lowest LOD at 67 pg/mL GFAP. Longer time scales, such as averaging between 45s to 60s, show lower current values with higher LOD. By averaging at earlier time scales, the measurement time can be shortened from 60s to 5s.

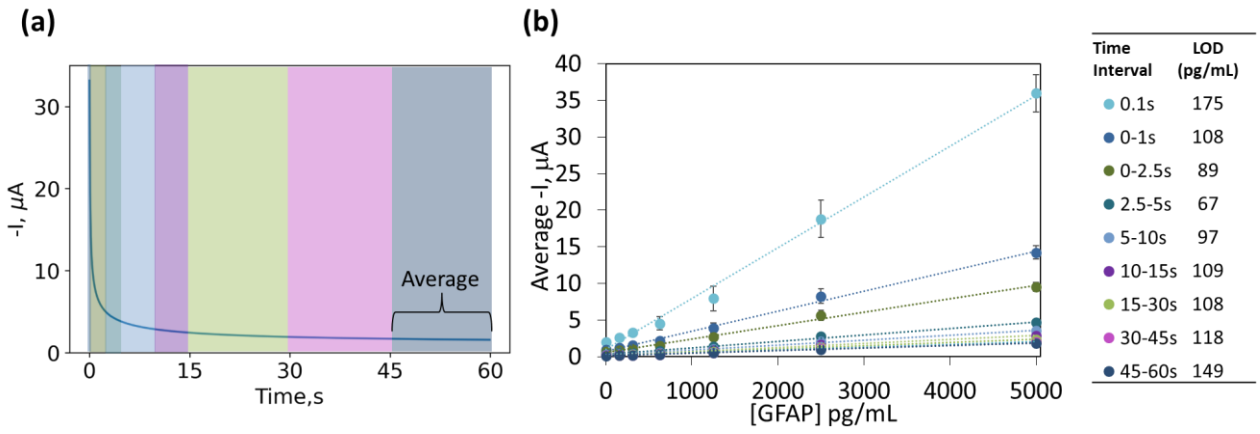


Figure 4.10:(a) Representative amperometry measurement of 5000 pg/mL GFAP concentration. (b) The reductive current was averaged at different time intervals along the amperometry curves for different GFAP concentrations (N=3; N=5 for 0 pg/mL). Incubation times (I-IV) were 2 hours, 2 hours, 20 minutes, and 6 minutes, respectively.

To determine the best detection method, electrochemical and optical assays were compared with GFAP and UCH-L1 biomarkers. Figure 4.11 demonstrates standard calibration curves generated with optical absorbance and amperometry measurement in enzyme linked immunoassays. The current was averaged between 2.5 s and 5 s for each electrochemical experimental curve and plotted with respect to a specific biomarker concentration (Figure 4.11b and Figure 4.11d). Both optical and electrochemical standard curves were linear and had a good fit with linear regression lines. Both assays for GFAP and UCH-L1 were able to quantify a broad range of biomarker concentration (156-5,000 pg/mL for GFAP; 78-2,500 pg/mL for UCH-L1). The LOD of the electrochemical assays were 44-55% lower than the LOD of the optical assays. Thus, electrochemical detection of immunoassays is a promising detection method for quantifying TBI biomarkers.

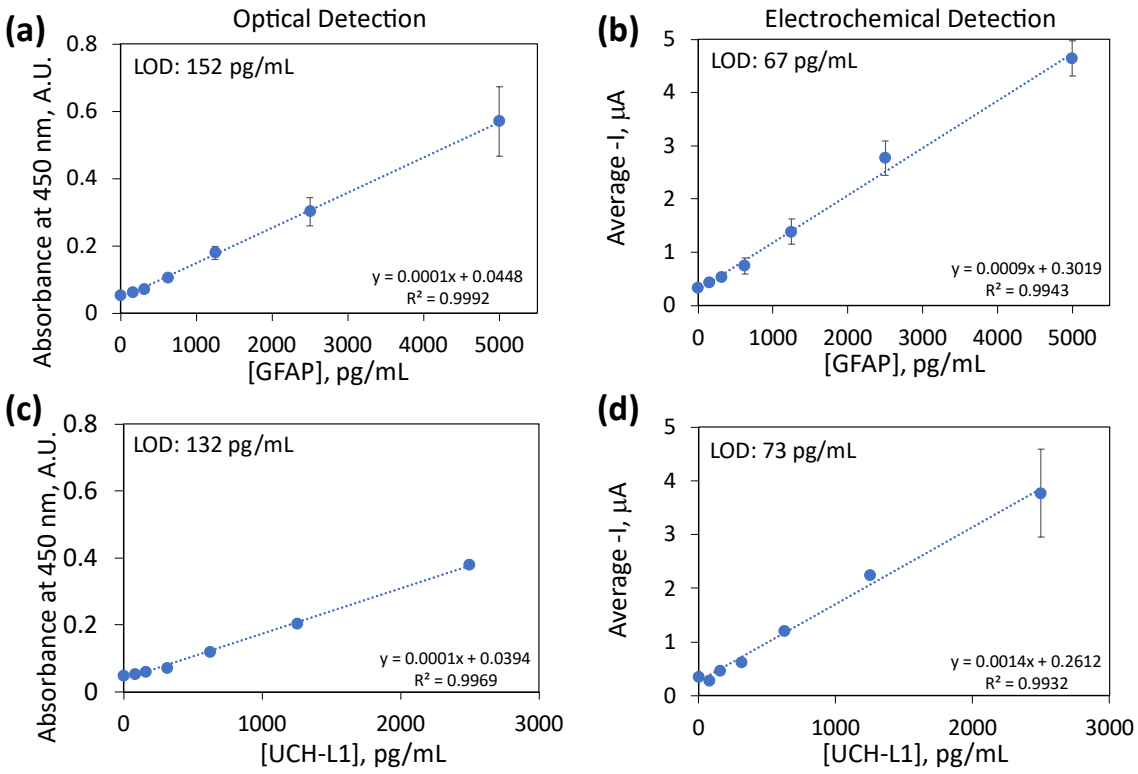


Figure 4.11:Comparison of optical and electrochemical detection methods standard curves with (a) GFAP optical absorbance (N=4; N=8 for 0 pg/mL) (b) GFAP amperometry measurement (N=3; N=5 for 0 pg/mL) (c) UCH-L1 optical absorbance (N=2; N=4 for 0 pg/mL) (d) UCH-L1 amperometry measurement (N=2; N=4 for 0 pg/mL). Incubation times (I-IV) were 2 hours, 2 hours, 20 minutes, and 6 minutes, respectively. For optical measurements, 2.5 µm beads were reacted with 100 µL of TMB and 50 µL of acid stop solution. The beads were removed from solution and measured in a plate reader at λ=450 nm. For electrochemical measurements, 5 µm beads reacted with 20 µL TMB and the first 15s of measurement was averaged. Each curve was fit with a linear regression trendline (blue dotted line).

4.4.4 Device Design and Multiplexing

Based on the successful quantification of TBI biomarkers with electrochemical immunoassays, electrodes should be incorporated into an existing variable height device[107, 114]. The proposed device design, shown in Figure 4.12a, consists of three sets of electrodes (e.g., working, counter and reference) spaced at different heights along the variable height channel. When conjugated beads are introduced into the channel, they will become trapped at a location corresponding to their height which will align with an electrode set. By conjugating different

capture antibodies on each bead size, the device can multiplex for TBI indicating biomarkers (e.g., UCH-L1, GFAP, etc.). Further, the device could be redesigned to multiplex more than three different biomarkers by increasing the length of the channels.

To properly multiplex with multiple biomarkers, the proposed design must account for interference between electrodes. In Figure 4.12b, a 1D diffusion calculation has been conducted to predict the diffusion of TMB^+ during the reaction and electrochemical measurement. As the height (2-50 µm) and width (3 mm) of the device are small in comparison to the length (20 cm) of the channel, the 1D calculation is an appropriate approximation. The calculated TMB^+/TMB_0^+ ratio is plotted as a function of the distance from the TMB^+ source (e.g., the electrode where the beads are trapped). After 1 minute, the TMB^+ has little time to diffuse with no TMB^+ present 0.5 mm away from the TMB^+ source. After 30 minutes, the distance to where no TMB^+ is observed shifts to 2.5 mm away from the source. Previously, we demonstrated that that TBI biomarkers could be quantified with a 6 minute TMB reaction and 5s measurement. Based on the 1D diffusion equation, the results suggest that the electrodes could be 1.5 mm apart without any interference between different solutions. However, it is recommended to start by designing electrodes sets 3 mm apart to ensure diffusion is not an issue with multiplexing.

To fabricate the proposed devices, two process flows are needed for the respective glass channel wafer and silicon electrode wafer. First, the glass wafer would need to be etched to create the ramped variable height channel. As previously described[107, 114], the glass wafer would undergo a lithography process where the wafer would be protected with a Cr/Au layer. After liftoff, the Cr/Au would be removed where the channel features were located. The wafer would be dipped in hydrofluoric acid (HF) and slowly removed with a robotic arm. The areas of the glass contacting HF will etch and a variable height profile will be created based on the amount of

time a specific area of the channel contacts the HF. The Cr/Au layers would then be removed with Cr and Au etch and inlet/outlet holes would be created with deep reactive ion etching. Second, the electrode features would need to be recessed into the silicon wafer. To this end, lithography and wet etching would be employed to recess the electrodes. Two lithography processes would be conducted to deposit Cr/Au working and counter electrodes and Ti/Ag reference electrodes. A silicon dioxide layer would then be deposited over the connecting metal wires to prevent silicon dioxide migration during anodic bonding. Next, the glass and silicon wafers would be fused together via anodic bonding. The wafer would be diced into individual devices and the areas where the bonding pads are located would be partially diced to remove the glass wafer over these areas. To complete the sensors, wires would be soldered to each electrode bonding pad and connected to a potentiostat.

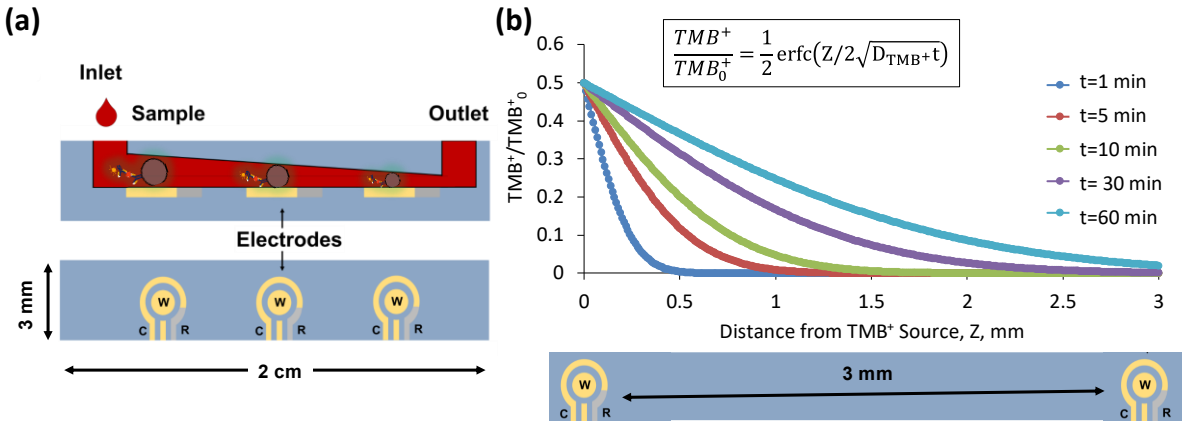


Figure 4.12:(a) The proposed multiplexed device design with three sets of electrodes placed at different heights along the channel. (b) One dimensional diffusion calculation to determine the ratio of final and initial TMB^+ concentration as a function of the distance from a TMB^+ source (e.g., working electrode). The TMB^+ diffusion coefficient was $3x10^{-10}$ m^2/s [37]. If electrode sets are placed 3 mm apart, TMB^+ should not diffuse between different electrode sets after 60 minutes.

4.5 Conclusion

In conclusion, this proof-of-concept research demonstrates a successful amperometry sensor that electrochemically detects relevant traumatic brain injury biomarkers. The work uses

bead based enzymatic sandwich immunoassays in combination with screen printed electrodes or plate readers to both optically and electrochemically quantify relevant TBI protein biomarkers. With high throughput optical detection, we found the appropriate reagent concentration and incubation time to use during assay development. We believe this work will trigger follow up research to determine the optimal in channel assay parameters for short detection time, low cost, and reduced limit of detection. By identifying the optimal average time interval in the amperometry curve, we decreased the electrochemical measurement time by 91%. The resulting GFAP and UCH-L1 standard curves indicated that electrochemical detection methods were comparable to optical with 44-55% reduced limit of detection. Finally, we proposed a design and fabrication procedure to create sensors capable of multiplexing different TBI biomarkers with minimal interference. The proposed device is capable of portable, sensitive detection for uses at the point-of-care to identify or monitor a traumatic brain injury.

Chapter 5 Conclusion and Future Work

5.1 Summary

The aim of this dissertation work was to develop electrochemical sensors capable of rapid, sensitive, and portable detection for monitoring environmental and biological samples. We developed a lead ion water quality sensor which was based on an electrodeposition capture and conductimetric detection system. We then utilized chronopotentiometry to develop a chloride ion sensor for applications in urinalysis. Lastly, we developed an enzymatic sandwich immunoassay for both optical and electrochemical detection of traumatic brain injury biomarkers.

We advanced a lead sensing system that captures conductive lead oxides and triggers when the electrodeposits bridge between electrodes. The bridging event causes a measurable change in resistance between the anode and floating electrode. The lead oxide deposition was confirmed to be governed by a diffusion limited process with visual inspection of scanning electron microscopy images, fractal analysis, review of literature, and COMSOL Multiphysics® modeling. With this fundamental understanding, we improved the lead sensor response time by changing sensor design and operating conditions. By reducing gap size between the anode/cathode and corresponding floating electrode, we shortened the lead detection time by 40%. Additionally, we improved the reliability of the sensor signal by agitating the sample to produce a more robust lead oxide deposition. The resulting miniature, sensitive sensors could be deployed at the end point of water infrastructure to monitor for lead contamination.

Next, we developed a chronopotentiometric sensor capable of rapid quantification of urinary chloride. The sensor signal was based on a transition time during which all chloride ions

are locally depleted. By tuning current density, we resolved different chloride concentration ranges with great theoretical agreement. We developed a current density sweep algorithm capable of resolving the entire relevant urinary chloride range with a single sensor. The chloride sensors could be reused at least 5 times in low concentrations (<100 mM NaCl) and were minimally impacted by changes to temperature and pH. Conductivity and transference number had greater influence on sensor signal but could be mitigated by adding additional ions to the solution prior to testing. We produced a reusable, simple and near real time sensor capable of successful operation in artificial urine samples. This work laid a foundation for further development of point-of-care and wearable urinary monitoring systems.

Finally, an enzymatic sandwich immunoassay procedure using optical and electrochemical detection was established to quantify biomarkers that elevate after a traumatic brain injury. Utilizing high throughput optical absorbance, the starting assay reagent concentrations and incubation times were determined for improved signal and limit of detection. The optical procedure was translated and compared to an electrochemical detection protocol. The electrochemical procedure showed great promise with lower limit of detection and ability to use miniaturized sensors and circuitry. We then proposed an appropriate design and fabrication process to introduce multiplexing as a sensor capability. With incorporation of electrodes into an existing variable height channel, a rapid, portable, miniaturized sensor could be used to multiplex a panel of biomarkers to aid in TBI diagnosis and monitoring.

5.2 Future Work

5.2.1 Lead Sensor

For further development, the lead sensor geometry and housing should be tuned for deployment within the home. As discussed in Chapter II, the smaller the gap size between

electrodes, the faster lead detection was achieved. Thus, in the next iteration of sensor design, the gap size between anode/cathode and corresponding floating electrode should be reduced to less than 3 µm. We also recommend introducing a barrier layer (e.g., parylene, silicon dioxide) to cover areas of the sensor electrodes that are not near a corresponding floating electrode (e.g., connecting wires, anode/cathode corners). By masking these areas, lead oxide is prevented from depositing in areas that are unable to trigger a lead oxide bridging event which could result in decreased sensor response time. In parallel, a sensor housing could be developed to mount the sensors in toilets or faucets within the home. Deploying sensors in the upper tank of home toilets is ideal, as the sensors are concealed for minimal maintenance detection and will not be in contact with downstream drinking water. Additionally, sensors will be exposed to frequent periods of agitation during flushing events, which has been shown to improve sensor signal.

The selected sensor geometry should undergo extensive tests in various solution conditions. Previously, the four-electrode sensor was investigated with individual and combined solutions of Pb^{2+}, Fe^{2+}, Zn^{2+}, and Cu^{2+} [65]. However, testing with additional heavy metals such as Ni^{2+}, Co^{2+}, Hg^{+}, Cd^{2+}, Cr^{3+} can further inform about the selectivity of the sensor. Of the listed heavy metals, Cr^{3+} is the only ion that will favor deposition on the lead sensing anode electrode, however, the lead deposition reaction is thermodynamically favored with a 200mV lower standard redox potential[65]. Additionally, the lead sensor should be evaluated in varying solution conductivities. In Chapter II, we focused on conducting experiments at the upper limit of drinking water conductivity (1000 µS/cm) to evaluate sensor performance. By testing at a higher conductivity, the solution resistance within the electrochemical cell decreases. The sensor should be evaluated at lower conductivities with different ions (e.g., Cl^{-}, SO_4^{2-}, HCO_3^{-}, Ca^{2+}, Mg^{2+}, Na^{+},

K^+) and temperatures to determine the effect on the lead deposition, precipitation of ions, and response time of the sensor.

Lastly, the sensors would benefit from long-term testing and deployment in real world conditions, such as in areas that have been prone to lead contamination in the past (e.g., Flint, MI and Newark, NJ). By testing in real conditions, the longevity and sensitivity of the sensors can be better understood. Previous long term experiments demonstrated precipitation on the heavy metal cathode sensing electrode which was mitigated by operating the sensor with no supplied potential[65]. Thus, follow up research should be conducted to determine possible strategies for cleaning, storing and reusing sensors. The outlined follow up research will be useful in determining the use case of the lead sensor.

The next steps that we recommend for a future student would be to focus on iterating the sensor design as described above. The selection of sensor design may benefit with the development of a computational model to further understand the impact of sensor geometry (e.g., gap distance, etc.) on the transport within the system, the growth rate of the lead oxide deposition, and the function of this growth (e.g., linear). With better understanding of the growth behavior, the sensor could become more quantitative as the amount of lead on the sensor could be predicted as a function of time.

5.2.2 Urinary Chloride Sensor

To be more impactful, the urinary chloride sensor could benefit from being integrated into a wearable system, such as a uroflowmeter[82]. To integrate, the sensor should be further miniaturized to fit into a wearable housing. This could be achieved using lithography procedures to develop a customized sensor using silver and platinum electrodes on a glass substrate. The sensor housing could be designed such that urine would collect into a stagnant holding area

where the measurement could be conducted. Alternatively, the sensor could be integrated into a funnel system where it would contact low flowing urine exiting the body during urination. To determine appropriate design, the sensor should be assessed in low flow conditions to determine the impact on the sensor signal. To increase the accuracy of the sensor, additional inexpensive sensors could be incorporated into this housing (e.g., conductivity, temperature, flow). By monitoring for conductivity and temperature, the algorithm could account for these parameters in real time and adjust the chloride concentration calculation accordingly.

The algorithm could be further improved to increase the longevity of the sensor. For instance, the sensor could calculate the remaining sensor lifetime by tracking the amount of detected chloride concentration and number of uses. An algorithm could be developed to adjust for the chloride concentration based on these suggested parameters and the amount of silver chloride deposited on the sensor. Additional follow up research could be conducted to prevent fouling of the sensor surface. For example, the algorithm time could be further reduced to minimize silver chloride electrodeposition on the surface of the working electrode. Cleaning of the sensor surface could also be investigated to further extend the lifetime of the sensor. Chemical, physical, and electrochemical methods of removing silver chloride should be explored.

The sensor should be evaluated in cases that closely resemble the sensor application of urinalysis. This is best conducted by testing the sensor performance in real urine samples spiked with varying chloride concentrations. The composition of the real urine should be confirmed via lab testing and compared with the value obtained with the developed chloride sensor. Testing in real urine samples can evaluate the sensor performance and identify any interfering species that could affect the measurement. Additional experiments relating to interfering species would be

beneficial to conduct in simple solutions. Specifically, halides (I^-, Br^-) should be investigated as these species are thermodynamically able to react with Ag and form solid electrodeposits (AgI, AgBr). However, we believe that the halides will likely not be an issue with the sensor as chloride is the most abundant halide present in urine.

For the next student working on this project, we recommend sourcing a credit card size or smaller potentiostat (e.g., Palmsens EmStat4M Module) to translate the sensing system from a benchtop to portable method. We also recommend fabricating the chloride sensors in-house using lithography procedures to further miniaturize the sensor. Through control of the design via in-house fabrication, the area of the working electrode could be studied to determine the effect on sensor response, fouling of the sensor surface, and reusability. Additionally, the developer of these sensors should be aware that the formation of silver chloride during the reaction can react with light, however, we did not find that this affected the sensor performance.

5.2.3 Traumatic Brain Injury Biomarker Sensor

The proposed traumatic brain injury sensor should be designed and fabricated to incorporate electrodes into a variable height device. The design constraints and process steps to achieve this fabrication have been outlined in Chapter IV. A potential pivot point if electrode fabrication proves difficult would be to design alternative bead capturing microfluidic sensors such as spiral sorters. After development, testing should be conducted in the channel such that the entire assay is completed on-chip. A vacuum system can be used to control the flow of reagents into the channel.

With the assay translated to an in-channel system, the assay parameters could be further optimized in a system that is more representative of the final product. The experimental design space is large with the sandwich immunoassay (e.g., multiple reagents and incubations) and

follow up research can aid in optimizing these parameters. Presently, the assay is conducted inside of a vial and takes upwards of 5 hours to complete. To become practical for point-of-care applications, this time must be reduced. We are confident that a significant reduction in overall assay time can be achieved with an on-chip assay. We predict that a faster reagent contact time is achievable by trapping the beads at a specific location and flowing solution across the channel.

After establishment of optimal parameters for individual biomarkers, we recommend investigating the sensor multiplexing capabilities. As the sensor signal is tied directly to the solution surrounding the beads, interference from diffusion will need to be thoroughly studied. We calculated TMB diffusion and accounted for the interference in the suggested design in Chapter IV. An alternative path may be to explore additional enzyme-substrate reactions (e.g., AP and p-Nitrophenyl Phosphate) to further multiplexing capabilities. Different enzymes could be attached to various detection antibodies prior to being introduced to the channel.

For the next student working on this project, we recommend conducting a sensitivity analysis to verify the most sensitive parameters (e.g., reagent concentrations, incubation times, etc.) effect on the outputs of interest (e.g., total assay time, reagent concentration, etc.). We believe by conducting this analysis, the wide experimental space can be narrowed to focus on the most important parameters affecting the assay. We also recommend sourcing larger sized (e.g., > 5 μm) beads with surface epoxy groups to enable the future device channel to have a larger input and output channel. By allowing larger channels, the flow through the device can easily be increased to reduce overall assay time.

5.3 Conclusion

This dissertation work is merely a piece of the wide field of chemical sensing. We primarily conducted early-stage research through development of novel electrochemical sensing

systems. Our work created selective sensors that detected a variety of chemical species, including heavy metals, halides, and proteins. The choice in developing electrochemical detection systems over alternative detection methods was strategic as we believe electrochemical sensors will be advantageous for future applications. Specifically, electrochemical sensors show promise in developing cost-effective, rapid, simple, and miniaturized sensors. We focused on developing sensors with unmodified pure metal electrodes and pseudo reference electrodes. Through this simplified design, sensors can be easily fabricated, produced in bulk to reduce cost, and miniaturized for portable use.

In the next decade, we predict chemical information (e.g., ion, protein concentration) will become more accessible to the end user. In-home smart sensors, wearables, and point-of-care devices are currently emerging as smart healthcare and environmental monitoring devices[126]. The potential species that could be monitored include, but are not limited to, ions, heavy metals, viruses, pathogens, bacteria, pharmaceuticals, and chemical pollutants. We predict these technologies will continue to develop for improved precision health:

- In-home smart sensors. Smart toilets, which are emerging on the market today, could monitor the body and home environment by utilizing chemical sensors. For example, the upper tank of the toilet could monitor the water quality within the home. The toilet bowl which collects urine, an underutilized indicator of health, could be equipped with many chemical sensors to provide real time health updates.
- Wearable devices. Currently this space is primarily dominated by optical smartwatches that are used to track health information. Additional areas that are emerging include sweat sensors, wearable fabrics, smart tattoos, and smart diapers.

We predict wearable devices could be particularly valuable in the ICU or assisted living facilities where patient monitoring is critical.

- Point-of-care devices. Pregnancy and COVID testing have demonstrated the importance of single use devices that provide YES/NO results in an end user setting. We predict this space to expand towards identifying and monitoring additional disease states as new analytical technologies are developed. Multiplexed sensors capable of testing and quantifying many analytes and continuous testing are predicted to emerge.

We conclude this dissertation by listing challenges that should be addressed to achieve progress in development of electrochemical sensors for monitoring environmental and biological samples:

- Developing reusable and low maintenance sensors. Especially in cases of in-home smart sensors and wearable devices, reusability and extended lifetime will be key to the sustainability and cost of using these devices. In our work, sensors were single use or reusable in specific cases. With electrochemical sensors that utilize a reaction to capture the molecule of interest, it is important to mitigate fouling the sensor surface. Developing non-invasive analytical techniques, redesigning sensor geometries or developing complex sensing algorithms could minimize damage to the sensor surface. Additionally, to extend the sensor lifetime, many miniaturized sensors could be placed in series and controlled by an embedded microprocessor.
- Understanding interference in complex samples. The sensors developed in this early-stage work have been investigated in simplified solutions tuned towards a specific application. Environmental and biological fluids are much more complex containing

many different ions and organic species that are continuously changing. Extensive work needs to be conducted in understanding and mitigating interference from complex samples. Large experimental design may benefit by being paired with machine learning to analyze multivariable experimental matrixes.

- Data management and algorithm design. In most sensors, an algorithm is needed to convert generated raw data into a readout conclusion (e.g., disease diagnosis). As smart healthcare devices continuous to develop, we must create sustainable systems of monitoring and identifying meaning in the large amount of generated data. In some cases, simplified results (e.g., YES/NO) will be favored as the sensor capabilities must be tailored to the application. For example, quantitative sensing is superior to sensing that only has a binary readout, but not in the case of lead sensing where a homeowner only needs to know that lead is present to take action.

The above challenge areas provide exciting avenues for future dissertation work in this field.

Bibliography

1. C. Dincer, R. Bruch, E. Rama, M. T. Fernández-Abedul, A. Merkoçi, A. Manz, G. Urban, and F. Güder, *Advanced Materials,* **31** 1806739 (2019).
2. H. Bi and X. Han, in *Chemical, Gas, and Biosensors for Internet of Things and Related Applications*, K. Mitsubayashi, O. Niwa and Y. Ueno, eds., p. 147-160, Elsevier, (2019).
3. C. M. A. Brett, *Pure and Applied Chemistry,* **73** (12), 1969-1977 (2001).
4. B. Bansod, T. Kumar, R. Thakur, S. Rana, and I. Singh, *Biosensors & bioelectronics,* **94** 443-455 (2017).
5. P. Kruse, *Journal of Physics D: Applied Physics*, **51** (20), 203002 (2018).
6. F. Gao, C. Liu, L. Zhang, T. Liu, Z. Wang, Z. Song, H. Cai, Z. Fang, J. Chen, and J. Wang, *Microsystems & Nanoengineering,* **9** (1), 1 (2023).
7. V. Naresh and N. Lee, *Sensors,* **21** (4), 1109 (2021).
8. M. Jović, D. Prim, E. Saini, and M. E. Pfeifer, *Biosensors (Basel),* **12** (3), (2022).
9. Y.-S. Chen, C.-H. Huang, P.-C. Pai, J. Seo, and K. F. Lei, *Biosensors,* **13** (1), 83 (2023).
10. L. Cilliers and F. Retief, in *Toxicology in Antiquity (Second Edition)*, P. Wexler, ed., p. 221-229, Academic Press, (2019).
11. R. Rabin, *American journal of public health*, **98** (9), 1584-1592 (2008).
12. P. Z. Ruckart, A. S. Ettinger, M. Hanna-Attisha, N. Jones, S. I. Davis, and P. N. Breysse, *Journal of public health management and practice : JPHMP,* 25 Suppl 1, Lead Poisoning Prevention (Suppl 1 LEAD POISONING PREVENTION), S84-s90 (2019).
13. B. F. Palmer and D. J. Clegg, *Clinical Journal of the American Society of Nephrology,* **14** (2), 306-316 (2019).
14. R. A. Sherman and R. P. Eisinger, *Jama,* **247** (22), 3121-3124 (1982).
15. H. Kataoka, (2021).
16. H. Kataoka, *Cardiology and Therapy,* **10** (2), 407-428 (2021).
17. J. van der Leeuw, M. H. de Borst, L. M. Kieneker, S. J. Bakker, R. T. Gansevoort, and M. B. Rookmaaker, *PloS one,* **15** (2), e0228490 (2020).
18. V. Panuccio, P. Pizzini, G. Parlongo, G. Caridi, R. Tripepi, A. Mafrica, S. Cutrupi, G. D'Arrigo, G. Porto, and C. Garofalo, *Clinical Chemistry and Laboratory Medicine (CCLM),* **57** (8), 1162-1168 (2019).
19. N. Heeney, R. Lee, B. Hockin, D. Clarke, S. Sanatani, K. Armstrong, T. Sedlak, and V. Claydon, *Autonomic Neuroscience,* **233** 102797 (2021).
20. M. Brüngel, R. Kluthe, and P. Fürst, *Annals of nutrition and metabolism,* **45** (4), 169-174 (2001).
21. C.-Y. Wang, M. E. Cogswell, C. M. Loria, T.-C. Chen, C. M. Pfeiffer, C. A. Swanson, K. L. Caldwell, C. G. Perrine, A. L. Carriquiry, and K. Liu, *The Journal of nutrition,* **143** (8), 1276-1282 (2013).
22. M. C. Dewan, A. Rattani, S. Gupta, R. E. Baticulon, Y.-C. Hung, M. Punchak, A. Agrawal, A. O. Adeleye, M. G. Shrime, and A. M. Rubiano, *Journal of neurosurgery,* **130** (4), 1080-1097 (2018).

23. F. K. Korley, G. D. Kelen, C. M. Jones, and R. Diaz-Arrastia, *The Journal of head trauma rehabilitation*, **31** (6), 379 (2016).
24. (U. S. EPA., ed.), Cincinnati, OH, 1994.
25. (U. S. EPA., ed.), Cincinnati, OH, 1982.
26. S. C. Wilschefski and M. R. Baxter, *The Clinical biochemist. Reviews*, **40** (3), 115-133 (2019).
27. N. Bhalla, P. Jolly, N. Formisano, and P. Estrela, *Essays in biochemistry*, **60** (1), 1-8 (2016).
28. C. I. L. Justino, A. C. Freitas, R. Pereira, A. C. Duarte, and T. A. P. Rocha Santos, *TrAC Trends in Analytical Chemistry*, **68** 2-17 (2015).
29. L. Eddaif and A. Shaban, in *Advanced Sensor Technology*, A. Barhoum and Z. Altintas, eds., p. 17-49, Elsevier, (2023).
30. F. Ghaderinezhad, H. Ceylan Koydemir, D. Tseng, D. Karinca, K. Liang, A. Ozcan, and S. Tasoglu, *Scientific reports*, **10** (1), 1-9 (2020).
31. A. Yakoh, P. Rattanarat, W. Siangproh, and O. Chailapakul, *Talanta*, **178** 134-140 (2018).
32. I. I. Ebralidze, N. O. Laschuk, J. Poisson, and O. V. Zenkina, in *Nanomaterials Design for Sensing Applications*, O. V. Zenkina, ed., p. 1-39, Elsevier, (2019).
33. Y.-H. Shin, M. T. Gutierrez-Wing, and J.-W. Choi, *Journal of The Electrochemical Society*, **168** (1), 017502 (2021).
34. N. Jaffrezic-Renault and S. V. Dzyadevych, *Sensors*, **8** (4), 2569-2588 (2008).
35. A. C. Lazanas and M. I. Prodromidis, *ACS Measurement Science Au*, (2023).
36. I. Yaroshenko, D. Kirsanov, L. Kartsova, A. Sidorova, I. Borisova, and A. Legin, *Talanta*, **131** 556-561 (2015).
37. H. Li, Y. Lu, and P. K. Wong, *Lab Chip*, **18** (20), 3086-3089 (2018).
38. J. Bujes-Garrido and M. Arcos-Martínez, *Sensors and Actuators B: Chemical*, **240** 224-228 (2017).
39. A. G. M. Ferrari, P. Carrington, S. J. Rowley-Neale, and C. E. Banks, *Environ Sci-Wat Res*, **6** (10), 2676-2690 (2020).
40. Y.-J. Fan, Y.-C. Hsu, B.-C. Gu, and C.-C. Wu, *Microchemical Journal*, **154** 104641 (2020).
41. P. Bergveld, J. C. Eijkel, and W. Olthuis, *Biosensors and Bioelectronics*, **12** (9-10), 905-916 (1997).
42. Y. Abbas, W. Olthuis, and A. van den Berg, *Sensors and actuators B: Chemical*, **188** 433-439 (2013).
43. A. Ganguly and S. Prasad, *Sensors*, **19** (20), 4590 (2019).
44. A. Ganguly, P. Rice, K.-C. Lin, S. Muthukumar, and S. Prasad, *SLAS TECHNOLOGY: Translating Life Sciences Innovation*, **25** (1), 25-32 (2020).
45. L. Wei, Z. Lv, Y. He, L. Cheng, Y. Qiu, X. Huang, C. Ding, H. Wu, and A. Liu, *Sensors and Actuators B: Chemical*, **379** 133213 (2023).
46. X. Ke, *Talanta*, **211** 120734 (2020).
47. N. Elgrishi, K. J. Rountree, B. D. McCarthy, E. S. Rountree, T. T. Eisenhart, and J. L. Dempsey, *Journal of Chemical Education*, **95** (2), 197-206 (2018).
48. Y. Abbas, D. B. de Graaf, W. Olthuis, and A. van den Berg, *Analytica chimica acta*, **821** 81-88 (2014).
49. H. L. Needleman and D. Bellinger, *Annu Rev Publ Health*, **12** 111-140 (1991).

50. S. Satarug, G. C. Gobe, D. A. Vesey, and K. R. Phelps, *Toxics*, **8** (4), 86 (2020).
51. A. Mantha, M. Tang, K. J. Pieper, J. L. Parks, and M. A. Edwards, *Water Res X*, **7** (2020).
52. Y. Bae, J. D. Pasteris, and D. E. Giammar, *Water Research*, **177** 115764 (2020).
53. S. K. Ameri, P. K. Singh, and S. Sonkusale, *Biosensors & bioelectronics*, **61** 625-630 (2014).
54. Y. L. Hung, T. M. Hsiung, Y. Y. Chen, and C. C. Huang, *Talanta*, **82** (2), 516-522 (2010).
55. Y. Sasaki, T. Minamiki, S. Tokito, and T. Minami, *Chem Commun*, **53** (49), 6561-6564 (2017).
56. W. C. Lin, Z. R. Li, and M. A. Burns, *Analytical Chemistry*, **89** (17), 8748-8756 (2017).
57. E. Doré, D. A. Lytle, L. Wasserstrom, J. Swertfeger, and S. Triantafyllidou, *Critical Reviews in Environmental Science and Technology*, **51** (20), 2357-2388 (2021).
58. R. Kriss, K. J. Pieper, J. Parks, and M. A. Edwards, *Environmental Science & Technology*, **55** (3), 1964-1972 (2021).
59. P. Fabry and J. Fouletier, *Chemical and Biological Microsensors: Applications in Fluid Media*, Wiley (2013).
60. A. Karperien, 1999-2013.
61. J. Nicolás-Carlock and J. Carrillo-Estrada, *Scientific reports*, **9** (1), 1-11 (2019).
62. C. Lupo and D. Schlettwein, *Journal of The Electrochemical Society*, **166** (1), D3182 (2018).
63. *COMSOL Multiphysics® v. 5.5*, (2020).
64. J. Newman and K. E. Thomas-Alyea, *Electrochemical Systems*, Wiley (2004).
65. W. C. Lin, Z. Li, and M. A. Burns, *Anal Chem*, **89** (17), 8748-8756 (2017).
66. F. Sagues, M. Q. Lopez-Salvans, and J. Claret, *Phys Rep*, **337** (1-2), 97-115 (2000).
67. M. A. Baki and L. Badr, *Chaos, Solitons & Fractals*, **143** 110586 (2021).
68. T. C. Halsey, *Phys Today*, **53** (11), 36-41 (2000).
69. M. Rosso, *Electrochim Acta*, **53** (1), 250-256 (2007).
70. M. Jeong, T. Yokoshima, H. Nara, T. Momma, and T. Osaka, *Rsc Adv*, **4** (51), 26872-26880 (2014).
71. A. Wlasenko, F. Soltani, D. Zakopcan, D. Sinton, and G. M. Steeves, *Phys Rev E*, **81** (2), (2010).
72. H. M. Wang, S. F. Chen, T. J. Okeefe, M. Degrez, and R. Winand, *J Appl Electrochem*, **19** (2), 174-182 (1989).
73. R. Walker and N. S. Holt, *Surface technology*, **22** (2), 165-174 (1984).
74. J. L. Rein and S. G. Coca, *American Journal of Physiology-Renal Physiology*, **316** (3), F587-F605 (2019).
75. K. Berend, L. H. van Hulsteijn, and R. O. Gans, *European journal of internal medicine*, **23** (3), 203-211 (2012).
76. G. Bandak and K. B. Kashani, *F1000Research*, **6** (2017).
77. Y. Komaru, K. Doi, R. Matsuura, T. Yoshida, Y. Miyamoto, K. Yoshimoto, and M. Nangaku, *Nephrology*, **25** (5), 384-389 (2020).
78. N. a. M. Yunos, R. Bellomo, D. Story, and J. Kellum, *Critical care*, **14** (4), 1-10 (2010).
79. R. Vasumathi and P. Neelamegam, *Sensors & Transducers*, **119** (8), 142 (2010).
80. J. S. Pereira, L. O. Diehl, F. A. Duarte, M. F. Santos, R. C. Guimarães, V. L. Dressler, and É. M. Flores, *Journal of Chromatography A*, **1213** (2), 249-252 (2008).

81. G. Xu, C. Cheng, W. Yuan, Z. Liu, L. Zhu, X. Li, Y. Lu, Z. Chen, J. Liu, and Z. Cui, *Sensors and Actuators B: Chemical,* **297** 126743 (2019).
82. A. Attari, J. A. Ashton-Miller, J. O. Delancey, M. A. Burns, T. M. Kirkbride, E. P. Carlin, A. J. Ramachandran, and C. A. Day. Google Patents, 2021.
83. J. Kim, S. Lee, S. Kim, M. Jung, H. Lee, and M. S. Han, *Dyes and Pigments,* **177** 108291 (2020).
84. M. Šídlo, P. Lubal, and P. Anzenbacher, *Chemosensors,* **9** (2), 39 (2021).
85. J. Bujes-Garrido, D. Izquierdo-Bote, A. Heras, A. Colina, and M. Arcos-Martínez, *Analytica chimica acta,* **1012** 42-48 (2018).
86. D. B. de Graaf, Y. Abbas, J. G. Bomer, W. Olthuis, and A. van den Berg, *Analytica chimica acta,* **888** 44-51 (2015).
87. H.-J. Sheen, B. Panigrahi, T.-R. Kuo, W.-C. Hsu, P.-S. Chung, Q.-Z. Xie, C.-Y. Lin, Y.-S. Chang, C.-T. Lin, and Y.-J. Fan, *Biosensors and Bioelectronics,* **210** 114338 (2022).
88. C.-Y. Lin, U. T. N. Nguyen, H.-Y. Hsieh, H. Tahara, Y.-S. Chang, B.-Y. Wang, B.-C. Gu, Y.-H. Dai, C.-C. Wu, and I.-J. Tsai, *Talanta*, **236** 122886 (2022).
89. M.-H. Chiu, W.-L. Cheng, G. Muthuraman, C.-T. Hsu, H.-H. Chung, and J.-M. Zen, *Biosensors and Bioelectronics,* **24** (10), 3008-3013 (2009).
90. A. J. Bard, L. R. Faulkner, and H. S. White, *Electrochemical methods: fundamentals and applications*, John Wiley & Sons (2001).
91. A. Adamson, *A Textbook of Physical Chemistry*, Elsevier Science (1973).
92. Y. Fazil Marickar, *Urological research,* **38** (4), 233-235 (2010).
93. W.-C. Lin and M. A. Burns, *Analytical Methods,* **7** (9), 3981-3987 (2015).
94. W.-C. Lin, K. Brondum, C. W. Monroe, and M. A. Burns, *Sensors,* **17** (7), 1655 (2017).
95. F. Delange, B. d. Benoist, and H. Bürgi, *Bulletin of the World Health Organization,* **80** (8), 633-636 (2002).
96. (N. C. f. I. P. a. Control, ed.). Centers for Disease Control and Prevention, 2003.
97. J. R. Kulbe and J. W. Geddes, *Experimental neurology,* **275** 334-352 (2016).
98. A. D. Krausz, F. K. Korley, and M. A. Burns, *Biosensors,* **11** (9), 319 (2021).
99. C. f. D. C. a. Prevention, 2023.
100. A. L. Sharp, G. Nagaraj, E. J. Rippberger, E. Shen, C. J. Swap, M. A. Silver, T. McCormick, D. R. Vinson, and J. R. Hoffman, *Academic Emergency Medicine,* **24** (1), 22-30 (2017).
101. D. J. Brenner and E. J. Hall, *New England journal of medicine,* **357** (22), 2277-2284 (2007).
102. C. Moriates, N. T. Shah, and V. M. Arora, *Jama,* **310** (6), 577-578 (2013).
103. P. Vos, B. Jacobs, T. Andriessen, K. Lamers, G. Borm, T. Beems, M. Edwards, C. Rosmalen, and J. Vissers, *Neurology,* **75** (20), 1786-1793 (2010).
104. S. Mondello, L. Akinyi, A. Buki, S. Robicsek, A. Gabrielli, J. Tepas, L. Papa, G. M. Brophy, F. Tortella, and R. L. Hayes, *Neurosurgery,* **70** (3), 666 (2012).
105. U. Food, (2018).
106. L. Papa, G. M. Brophy, R. D. Welch, L. M. Lewis, C. F. Braga, C. N. Tan, N. J. Ameli, M. A. Lopez, C. A. Haeussler, and D. I. M. Giordano, *JAMA neurology,* **73** (5), 551-560 (2016).
107. A. D. Krausz, F. K. Korley, and M. A. Burns, *Biosensors,* **11** (9), 320 (2021).
108. F. Ricci, G. Adornetto, and G. Palleschi, *Electrochim Acta,* **84** 74-83 (2012).

109. S. Khetani, V. Ozhukil Kollath, V. Kundra, M. D. Nguyen, C. Debert, A. Sen, K. Karan, and A. Sanati-Nezhad, *ACS sensors*, **3** (4), 844-851 (2018).
110. L. Xu, S. Ramadan, O. E. Akingbade, Y. Zhang, S. Alodan, N. Graham, K. A. Zimmerman, E. Torres, A. Heslegrave, and P. K. Petrov, *ACS sensors*, **7** (1), 253-262 (2021).
111. B. A. Cardinell, C. P. Addington, S. E. Stabenfeldt, and J. La Belle, *Critical Reviews™ in Biomedical Engineering*, **47** (3), (2019).
112. J. Min, M. Nothing, B. Coble, H. Zheng, J. Park, H. Im, G. F. Weber, C. M. Castro, F. K. Swirski, and R. Weissleder, *Acs Nano*, **12** (4), 3378-3384 (2018).
113. A. Jones, L. Dhanapala, R. N. T. Kankanamage, C. V. Kumar, and J. F. Rusling, *Anal Chem*, **92** (1), 345-362 (2020).
114. S. E. Mena, M. P. de Beer, J. McCormick, N. Habibi, J. Lahann, and M. A. Burns, *Lab Chip*, **20** (14), 2510-2519 (2020).
115. M. Alhajj and A. Farhana, in *StatPearls [Internet]*, StatPearls Publishing, (2022).
116. O. Tzara, S. Amalie Simonsen, A. Sode West, M. Asser Karsdal, H. Klingenberg Iversen, and K. Henriksen, *Brain Injury*, **36** (6), 792-799 (2022).
117. X. Wang, L. Cohen, J. Wang, and D. R. Walt, *Journal of the American Chemical Society*, **140** (51), 18132-18139 (2018).
118. M. Diagnostics, 2023.
119. I. Technologies, 2023.
120. M. Li, Y. He, H. Meng, Y. Dong, Y. Shang, H. Liu, Z. Qu, and Y. Liu, *Journal of Dispersion Science and Technology*, **42** (4), 526-536 (2021).
121. S. Gu, S. Risse, Y. Lu, and M. Ballauff, *Chemphyschem : a European journal of chemical physics and physical chemistry*, **21** (5), 450-458 (2020).
122. D. Evans, K. I. Papadimitriou, L. Greathead, N. Vasilakis, P. Pantelidis, P. Kelleher, H. Morgan, and T. Prodromakis, *Sci Rep*, **7** (1), 685 (2017).
123. G. Volpe, R. Draisci, G. Palleschi, and D. Compagnone, *Analyst*, **123** (6), 1303-1307 (1998).
124. Abbott.
125. K. K. Wang, F. H. Kobeissy, Z. Shakkour, and J. A. Tyndall, *Acute Medicine & Surgery*, **8** (1), e622 (2021).
126. J. F. Hernández-Rodríguez, D. Rojas, and A. Escarpa, *Analytical Chemistry*, **93** (1), 167-183 (2021).